Lehigh University
Lehigh Preserve

Theses and Dissertations

2014

Analytical and Experimental Evaluation of Precast Sandwich Wall Panels Subjected to Blast, Breach, and Ballistic Demands

Patrick Alan Trasborg
Lehigh University

Follow this and additional works at: http://preserve.lehigh.edu/etd

 Part of the Civil and Environmental Engineering Commons

Recommended Citation
Trasborg, Patrick Alan, "Analytical and Experimental Evaluation of Precast Sandwich Wall Panels Subjected to Blast, Breach, and Ballistic Demands" (2014). *Theses and Dissertations.* Paper 1656.

This Dissertation is brought to you for free and open access by Lehigh Preserve. It has been accepted for inclusion in Theses and Dissertations by an authorized administrator of Lehigh Preserve. For more information, please contact preserve@lehigh.edu.

www.manaraa.com

ANALYTICAL AND EXPERIMENTAL EVALUATION OF PRECAST SANDWICH WALL PANELS SUBJECTED TO BLAST, BREACH, AND BALLISTIC DEMANDS

by

Patrick Trasborg

A Dissertation

Presented to the Graduate and Research Committee

of Lehigh University

in Candidacy for the Degree of

Doctor of Philosophy

in

Structural Engineering

Lehigh University

September 2014

www.manaraa.com

Copyright 2014 Patrick Trasborg

www.manaraa.com

CERTIFICATE OF APPROVAL

Approved and recommended for acceptance as a dissertation in partial fulfillment of the requirements for the degree of Doctor of Philosophy.

Date

Dissertation Director

Accepted Date

Committee Members:

Shamim Pakzad, Committee Chair

Clay Naito, Dissertation Advisor

Paolo Bocchini, Committee Member

John Wilson, Committee Member

James Davidson, External Member

www.manaraa.com

ACKNOWLEDGEMENTS

The author would like to thank his dissertation advisor, Professor Clay Naito, for guiding him academically and social, and tolerating him for the past four years. The author would also like to thank all the members of his dissertation committee, Committee Chair Professor Shamim Pakzad, Professor Paolo Bocchini, Professor James Davidson, and Professor John Wilson for their guidance and wisdom in research and beyond.

The author would like to thank all the lab technicians and staff for assisting him in undertaking the large experimental testing matrix and for their friendship throughout the research project especially Todd Anthony, Peter Bryan, Carl Bowman, Darrick Fritchman, John Hoffner, Shaun Keggan, Adam Kline, Gene Matlock, Roger Moyer, and Jeffrey Sampson. The author would also like to thank all the undergraduate and graduate students whom assisted him in his research project especially Corey Fallon, Pierluigi Olmati and Thiago de Aguiar Freire Sarkis.

The author would like to thank the PCI industry board including Steve Brock, HS Lew, Harry Gleich, Ned Cleland, Ken Baur, Tommy Mitchell, and Roger Becker for providing their invaluable experience in designing the various test matrices. Additionally, the author would like to thank PCI for granting him the PCI Daniel P. Jenny Fellowship. The author would also like to thank all of the organizations that donated their time, expertise, and material throughout the research project especially Casilio Concrete, Gate Precast, High Concrete Group LLC, Metromont Corporation, and Tindall Corporation. Without them, this research project would not have been possible.

Finally, the author would like to thank his family and friends for their support during the rigorous and many times daunting curriculum of the PhD degree, especially his mother Patricia Trasborg, brother Parker Trasborg, sister Catherine Trasborg, Uncle Gerry Sotolongo (UG), girlfriend Carolyn Zelenetz, and friend Cooper Zelenetz.

The material in this dissertation is based upon work supported by the National Science Foundation under Grant No. CMMI-1030812.

www.manaraa.com

TABLE OF CONTENTS

www.manaraa.com

www.manaraa.com

www.manaraa.com

www.manaraa.com

www.manaraa.com

LIST OF TABLES

www.manaraa.com

www.manaraa.com

LIST OF FIGURES

www.manaraa.com

www.manaraa.com

www.manaraa.com

www.manaraa.com

www.manaraa.com

www.manaraa.com

ABSTRACT

Due to heightened security concerns federal as well as many public facilities require some level of blast design, whether it be intentional or accidental. In addition, with the increasing cost in utilities and continuous rise in global warming, a movement has begun to streamline the construction process and limit the environmental footprint of every building. In response, the federal government now requires that all government buildings not only be designed for blast loads, but also sustainability.

Insulated wall panels are capable of meeting both the blast and sustainable requirements due to the inherit strength of a reinforced concrete slab and the thermal resistance provided from the insulating layer; however, limited experimental testing is available to prove that insulated wall panels are an ideal system for both blast and sustainability. The objective of this research is to develop the tools to design a blast and ballistic resistant insulated wall panel system. As part of this research, experimental tests were conducted on insulated panels to validate models developed to predict panel behavior observed. Using the results of the research an approach was developed to create a 1) Thermally efficient, 2) Blast Resistant, 3) Spall/Breach Resistant and 4) Ballistic Resistant panel.

Insulated wall panels are inherently thermally resistive due to the insulating foam located between the two layers of concrete. Parametric studies were performed via analytical calculations to determine the efficiency of the wall system. The calculations indicated that the insulating layer is fundamental to the resistance of the panel; an 8in. solid concrete panel had a thermal resistance of less than 10% of a panel 2in. of insulation sandwiched between two 3in. concrete wythes. Additionally, the parametric study indicated that the shear connectors located between the interior and exterior wythes can have a significant effect on the overall panel thermal resistance due to the thermal bridging phenomenon.

www.manaraa.com

Three panels were modeled with identical layout and wythe connectors with identical dimensions but different material: concrete, steel, and low-conductive material. The panel with concrete and steel wythe connectors saw a reduction in thermal resistance compared to the low-conductive material of nearly 78% and 62% respectively. Thus, to decrease the panel resistance while maintaining strength, a strong thermally resistive material must be used as a shear connector.

To improve the response to far-field detonations, experimental tests were performed on small solid panels as well as larger insulated panels. Locally unbonding the small solid panels allowed the panel to reach support rotations past the 10° specified by the United States Army Corps of Engineers as the highest threat level while the bonded panels reached less than 5° before softening. Additionally, testing of insulated wall panels revealed that the panel behavior is highly dependent on the shear tie constitutive property and location along the span. A numerical model was created to predict the behavior of an insulated and as a result, a new shear tie was developed to improve the flexural response of the panel while at the same time, decreasing the production cost.

To assess the response of insulated wall panels to close-in detonations, experimental tests and numerical models were conducted. The tests revealed that the insulation results in a detriment to panel performance as a panel with 2in. of insulation sandwiched between two 3in. thick concrete wythes breaches the exterior wythe while a 6in. thick solid concrete panel does not breach under the same demand. As the insulating layer thickness is increased, the panel does not breach due to the increased standoff created by the additional thickness. Additionally, the empirical formulas developed by the Unified Facilities Criteria for solid panels were shown to be inaccurate when used for insulated wall panels, while numerical simulations were able to bound the response of an insulated wall panel.

www.manaraa.com

To investigate the performance of insulated wall panels to ballistic and fragment demands, a probabilistic method was developed. The method results in the creation of fragility curves allowing a designer to assess the probability of perforation and residual velocity for a given threat at any wall thickness. Additionally, the likelihood of injury occurring to personnel behind the wall panel was assessed by using organ threshold tolerances provided in literature. Using the method developed, engineers can design the thickness of an insulated wall panel to achieve an acceptable probability of occurrence for injury.

Finally, all of the material learned through the first four stages were combined to create a comprehensive design example. An 8in. thick panel with 2in. of insulation was designed using the newly designed shear tie as well as a ductile shear tie with the same strength, and then subjected to the demands reviewed throughout the research project. The tie system allowed the wall to reach a support rotation of 10° while behaving in a moderate to heavy damage level when subjected to the far-field detonation demand. From the conclusions of the close-in detonation study, the panel is known to breach under the load prescribed. Ballistic fragility curves were developed showing that the panel stops a low threat ballistic with 100% certainty, but under a high ballistic threat the projectile has an 86.5% chance of perforating the wall system. For the fragmenting munition considered in the study, the wall system has a 15.4% chance of causing injury to personnel behind the wall. Finally, by using the new shear tie system developed, the wall system results in a reduction of less than 3% in the total R-value when compared to an insulated panel without thermal bridges due to the low thermal conductivity of the shear tie material.

www.manaraa.com

AUTHOR'S CONTRIBUTIONS

The following succinctly lists the author's original contributions to the field of structural engineering through the research project described within:

1. Development of two flexural mechanisms to improve the response of solid concrete slabs at large displacements: the dogbone method and locally unbonding the longitudinal reinforcement.

2. A method to predict the complete load-displacement response of partially composite insulated panels based on deformation of the shear connectors. Current methods are force based and are only able to predict the response of non-composite or fully-composite panels.

3. Creation of a new shear tie system tailored for far-field detonations while maintaining thermal resistance. The shear tie is stronger and more ductile than current systems allowing insulated panels to be built to resist blast demands while reducing overall cost of the panel.

4. Established performance of insulated wall panels to close-in detonations. Empirical equations for solid panels were assessed for insulated panels via experiments conducted on insulated panels.

5. Development of a stochastic approach to ballistic and fragment design. Current methods for direct weapon's fire are deterministic neglecting the large variance accompanying a ballistic demand. Additionally, current methods do not account for the life-safety of personnel behind the wall system.

www.manaraa.com

1. INTRODUCTION

After recent escalation in terroristic attacks on buildings including the Murrah Federal Building, Kohbar Towers, and the World Trade Center, as well as accidental explosions including the AZF chemical factory and Ryongchon disaster, engineers have begun designing buildings to be blast and ballistic resistant. Additionally, with the rising cost of utilities and continuing increase in public awareness of environmental protection, energy efficient buildings have become mainstream. Today, thanks to executive order 13514 (The White House 2009), all government facilities are required to not only be blast resistant but also energy efficient.

The goal of this research project, funded by the National Science Foundation Grant No. CMMI-1030812, is to develop a multi-threat insulated precast concrete wall system. Due to the insulation layer of the panel, the wall system will be thermally efficient meeting requirements by U.S. Green Building Council (USGBC 2005). Additionally, the wall system will be designed to resist far-field explosions, close-in detonations, and ballistic penetration. During the development of the multi-threat wall system, new analytical models and innovative detailing methods were created that can be used by other engineers to design future wall systems. Finally, a large amount of experimental data was generated during the research project to validate analytical models and innovative concepts. The experimental data is available in reports or is currently in review with journals in the field of structural engineering so that other engineers can utilize the data to improve the models or develop new models.

www.manaraa.com

2. BACKGROUND

Four different demands were considered for the insulated wall system developed: 1) Thermal Demands, 2) Far-Field Detonations, 3) Close-In Detonations, and 4) Ballistic Demands. Each of the demands were evaluated experimentally, numerically, analytically and/or empirically. Current methods for evaluating each demand are reviewed throughout the dissertation. In some cases, new methods are developed to predict the performance of the insulated wall panel system. The final section of the dissertation includes a design case study of an insulated wall panel utilizing material learned and developed throughout the previous four stages.

www.manaraa.com

3. THERMAL DEMANDS

The following section provides background on the insulated wall panel and highlights differences in panel thermal performance using different shear tie systems.

3.1. Thermal Background

In recent years, there has been pressure on designers to create a building that is not only safe to inhabit while meeting the needs of the occupants, but also a facility which minimizes the environmental impact while improving sustainability. To fulfill this requirement, the United States precast concrete industry responded with an energy efficient and economically viable building envelope system, the insulated concrete wall panel. Insulated concrete wall panels, also known as sandwich wall panels, consists of a layer of insulating material sandwiched between two layers of concrete (wythes).

Insulated concrete wall panels are often defined by three consecutive numbers, representing the thickness of each layer in inches. For example, a concrete panel with an external wythe (structural wythe) of 4 in., a layer of foam of 2 in., and an internal wythe (non-structural wythe) of 3 in., would be signified by 4-2-3. For the exterior and interior concrete wythes to act in unison, or compositely, shear ties are placed intermittently through the length of the panel to transfer the shear force between the two wythes, as shown in Figure 1.

www.manaraa.com

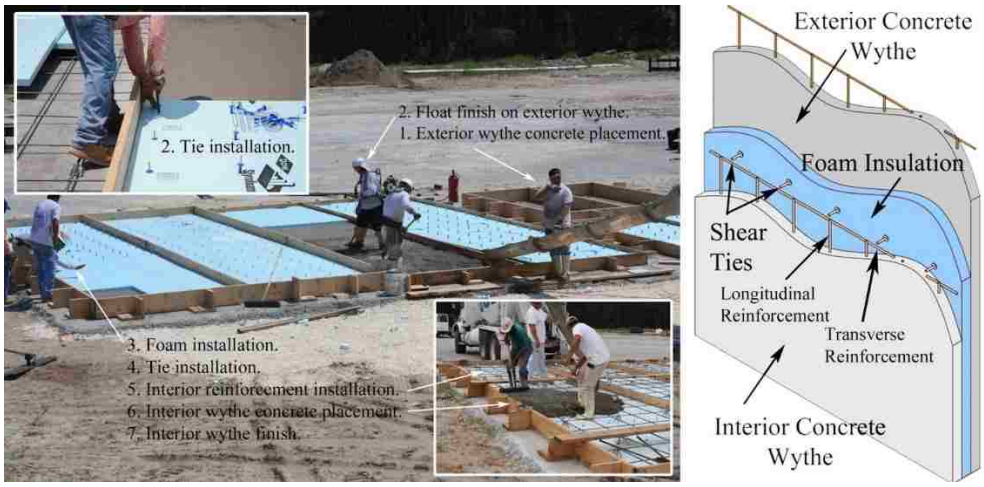

Figure 1: Insulated wall panel construction and configuration

Insulating material can vary widely depending on the function of the facility and economic requirements set by the building owner, but some commonly used insulating materials include EPS (expanded polystyrene), XPS (extruded polystyrene), and Polyiso (polyisocyanurate). The thermal resistance of the insulated concrete wall panel is predominantly attributed to the very low conductivities of the insulating material (0.04 W/m-K), while the concrete has a relatively high thermal conductivity (2.89 W/m-K for normal weight concrete) (PCI 2010b). Thus, the energy efficiency is obtained by creating a thermal barrier between the two layers of concrete via the insulating foam. The overall thermal resistance of the panel is referred to as an R-value with English units of $hr \cdot ft^2 \cdot ^oF/Btu$ and SI units of $K \cdot m^2/W$.

Shear ties provide the panel with strength in handling, construction, and service loads by connecting the exterior concrete wythe directly to the interior concrete wythe. Shear tie strength will be discussed in a following chapter. However, this allows for heat transmission to completely negate the highly resistive insulating material and travel directly along the shear ties in a phenomenon known as thermal bridging. Thermal

www.manaraa.com

bridging creates localized "hot spots" throughout the panel which can have an extremely detrimental effect on the overall R-value. The R-value for three panels with the same cross section dimensions are calculated by utilizing the ASHRAE zone method (ASHRAE 2005) with a modified strip calculation (Lee and Pessiki 2008): (A) 6 in. solid concrete panel (B) 3-2-3 panel with steel ties spaced at 16 in. (C) 3-2-3 panel with fiber glass ties spaced at 16 in. Panel A, without foam insulation, was found to have an R-value of 0.11 $K \cdot m^2/W$, while both panels with 2 in. of foam insulation each had a thermal resistance of over 13 times the solid panel. Panel B with steel ties was found to have an R-value of 1.44 $K \cdot m^2/W$ while panel C with fiber glass ties had an R-value of 1.87 $K \cdot m^2/W$. The properties and spacing of the shear ties can decrease the thermal resistance of a panel by over 20%. For this reason, many shear ties today are proprietary and are often constructed of low conductive material such as phenolic or cellular glass. In some design cases, the exterior and interior wythes are directly connected by discrete regions of solid concrete, called "solid zones" (PCI 2010b). Composite panels utilizing solid zones are simpler to fabricate than panels with shear ties as they do not require extra components; however, solid zones lead to similar thermal bridging issues as conductive shear ties.

3.2. Analytical Methods

Three approaches were used for the thermal analysis: the modified zone method, the isothermal planes method, and the parallel flow method. The zone method breaks the panel into two separate zones – Zone A containing the highly conductive element and Zone B containing the remaining portion of the panel. The two zones are then combined using the parallel flow method. The modified zone method is identical to the traditional zone method adopted by PCI except the width for Zone A is modified based on the concrete conductivity, insulation conductivity, shear tie conductivity, diameter of the tie, and the

www.manaraa.com

distance from the panel surface to the tie. The isothermal method considers lateral heat flow with little resistance while the parallel flow method assumes that no heat will travel through a lateral path. The parallel flow method allows an electrical circuit analogy to be made where the laws of combining series and parallel resistors are applied to solve the thermal resistance of the panel.

3.3. Parametric Study

All material resistances were taken from either PCI 7th edition (2010b) handbook thermal section and ASHRAE handbook fundamentals (2005). In this study, R will be in English units of *[(°F*hr*ft²)/(BTU*in)]* for resistance per thickness and *[(°F*hr*ft²)/(BTU)]* for resistance. The assumed properties are summarized in Table 25. To be conservative, the minimum value of EPS is taken from PCI Handbook as 3.1 (PCI 2010b).

Table 1: Material resistances

Material Description	**Resistance/thickness** *[(°F*hr*ft²)/(BTU*in)]*
Expanded polystyrene (EPS)	3.1
Low conductive tie	4.0
Steel tie	3.2E-3
Normal Weight Concrete (140 pcf)	0.10

The five cross sections shown in Figure 2 were considered. Figure 2a shows the cross section of the solid panel, (b) a panel with 2in. of insulation and no ties, (c) a panel with 1.5in by 0.33in solid zones, (d) a panel with 1.5in. by 0.33in. low-conductive ties and (e) a panel with 1.5in. by 0.33in. steel ties. Panel ties were not specifically designed for strength purposes, but rather to determine the sensitivity to tie type. All the wall systems had the same overall dimensions of 32in. wide, 8in. thick, and 144in. long. The layout for the ties is shown in Figure 3.

www.manaraa.com

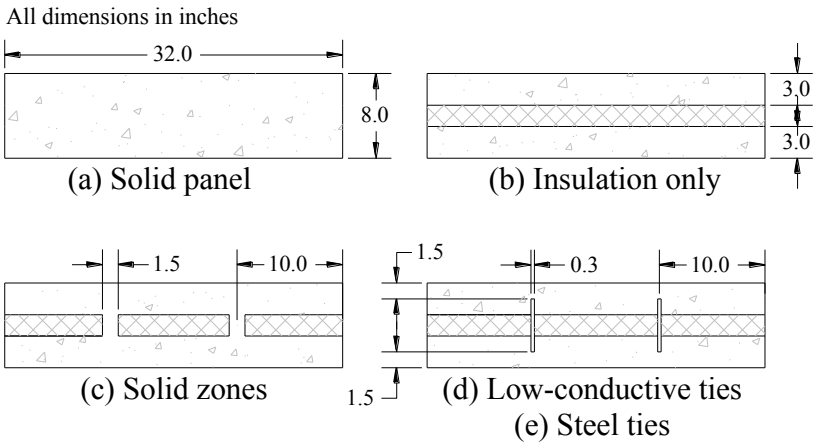

Figure 2: Cross sections considered

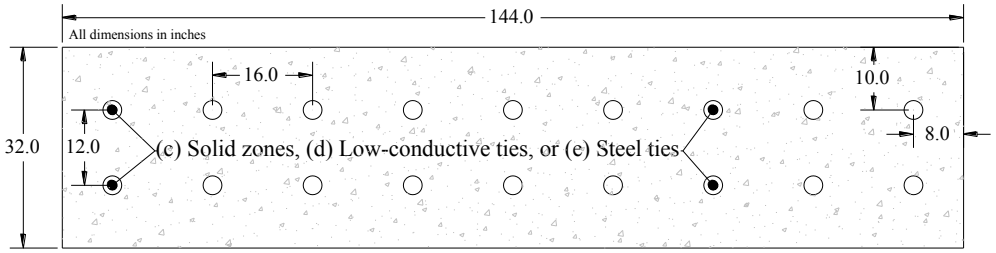

Figure 3: Panel tie layout

3.4. Results of Thermal Parametric Study

The R-value of each panel was calculated using three different methods: (1) modified zone method, (2) isothermal method, and (3) parallel flow method.

1. The zone method involves two separate computations – one for Zone A containing the bridging material and one for Zone B containing the remaining portion. The two computations are then combined using the parallel flow method. The width of Zone A is computed using a modified zone width (Pessiki, Lee 2008) for shear ties and the characteristic section method (PCI 2010b) for the concrete zones.

www.manaraa.com

2. The isothermal planes method considers lateral heat flow with little resistance in accordance with ASHRAE. The computations are performed as a series combination of layers.

3. The parallel flow method assumes no heat flow through lateral paths, thus the R values are higher than provided from the isothermal method. The computations are performed as a combination of parallel layers.

Table summarizes the R-value for each case and each method. All results are provided in *[(°F*hr*ft^2)/(BTU)]*. As expected, case (a) solid concrete and (b) insulated panel without ties yield the same results for the modified zone method as both the isothermal and parallel flow method. This is because the there are no lateral paths for heat to travel in any case, so including or neglecting lateral heat flow does not affect the results. Additionally, case (a) solid concrete and (b) insulated panel without ties act as the lower and upper bound respectively. In case (b), there are no paths for thermal bridging to occur, while case (a) offers very little thermal resistance due to the lack of insulating foam. Finally, the other methods perform as expected, with case (d) low conductive ties providing the next highest thermal resistance, followed by case (e) steel ties and case (c) solid zones.

Table 2: Tabulated thermal results

Case Name	***Modified Zone***	***Isothermal***	***Parallel Flow***
(a) Solid concrete	0.8	0.8	0.8
(b) Insulated – without ties	9.9	9.9	9.9
(c) Insulated – solid zones	2.2	2.1	4.0
(d) Insulated – low-conductive ties	6.8	7.0	6.8
(e) Insulated – steel ties	3.8	0.8	6.3

Intuitively, the choice of isothermal versus parallel flow method makes little difference on case (d) as the conductivity of the tie is very low, creating less of a path for lateral heat transfer. On the other hand, the choice of method has significant impact on case (c) solid zones and case (e) steel ties. This is due to the high conductivities of the tie materials,

www.manaraa.com

allowing for significant lateral heat transfer to occur.

3.5. Thermal Conclusion

Five different cases were tested using the modified zone method, isothermal planes method, and parallel flow method: (a) 8in. solid concrete panel, (b) 2in. of insulation without shear ties, (c) 2in. of insulation with solid zones, (d) 2in. of insulation with low-conductive ties, and (e) 2in. of insulation with steel ties. The following conclusions were drawn from the parametric study:

- A solid concrete panel provides significantly less thermal resistance than a panel with shear ties or solid zones. By replacing 25% of the interior with insulation, the R-value is increased by 92%. This is a conservative value as the minimum reported resistance for the insulation was used.
- Solid-zones and steel ties can have detrimental effects on the overall R-value of the panel. In the case considered, the R-value was decreased by nearly 78% and 62% respectively.
- The modified zone method yields the same results as the isothermal planes and parallel flow methods when there are no materials bridging across a different another i.e. there are no solid zones or shear ties. This is due to the fact that there are no paths for lateral heat transfer to occur. On the other hand, the isothermal planes and parallel flow methods yield extremely different results when highly conductive materials are embedded due to the large lateral heat paths.

www.manaraa.com

4. FAR-FIELD DETONATIONS

The following section provides background into the current methodology of blast design using the single degree of freedom (SDOF) approach per the Unified Facilities Criteria (DoD 2008c) with a modeling example (Olmati et al. 2014) followed by a discussion on improving blast response for solid reinforced concrete panels by developing flexural mechanisms (Trasborg et al. 2014b). Insulated panels are introduced and their response to out-of-plane loads (Trasborg et al. To be submitted) which is dependent on the shear tie behavior followed by the development of a new shear tie to improve insulated panel response. Finally, a discussion on flexural mechanism development for insulated panels is discussed.

4.1. Review of Current Methodology

The current discussion will be limited to a surface burst. When an explosive is detonated on the surface, a hemispherical shock wave is formed which moves outward until it eventually comes into contact with the structure creating a pressure wave. If the explosive has a large enough standoff distance, R, the blast load is generally assumed to be uniform in nature. Figure 4 below shows the detonation of an explosive and the pressure demand on a structure. For a surface blast, part of the shock wave bounces off the ground and is joined with the initial shock wave creating a magnified reflected pressure, P_r. The shock wave duration and pressure are dependent on the scaled distance, Z, equal to the quotient of the standoff distance and the equivalent explosive weight to the cube root. The equivalent explosive weight is calculated by multiplying the actual explosive weight by a TNT equivalency factor depending on the explosive type (DoD 2008c).

www.manaraa.com

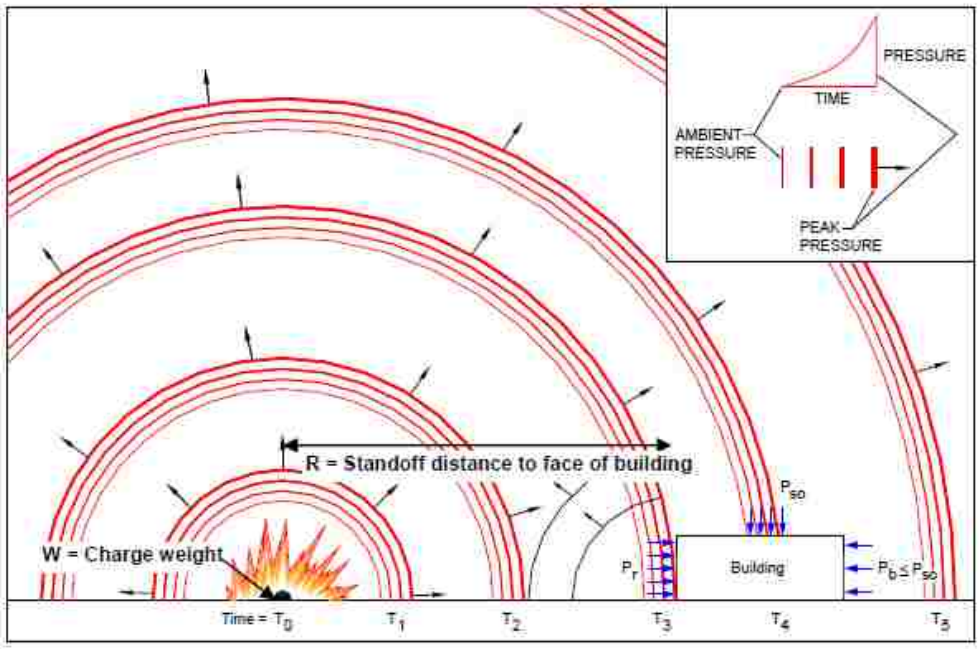

Figure 4: Blast demand on a structure (PCI 2010a)

The positive phase of the shockwave occurs as the pressure wave first strikes the building until the pressure wave changes to a suction, at which point the negative phase begins. Positive and negative phase shock wave charts exist, developed from experimental data *Z* to determine the characteristics of the shock wave that strikes the component. Thus, the load-history demand on a wall panel can be determined by knowing the standoff-distance and the equivalent charge weight.

A simplified method based on a single degree of freedom has been developed to determine the response of the component to the load-history demand. The component is made equivalent to a non-linear spring by knowing the component mass, resistance function, and mass transformation factors. The mass transformation factors are determined such that the SDOF system and the component will have equal kinetic, work, and strain energies at each time (PCI 2010a).

www.manaraa.com

The resistance function of a component is determined by performing a section analysis and calculating the load-displacement response under a uniform load. The applied load is converted to a pressure (resistance). The transformation factors are calculated by the boundary conditions, loading condition, and an assumed deformed shape. Various transformation factors may exist depending on the current stage of loading on the component. For example, a simply supported beam with a uniform load that is still in the elastic regime has a load-mass factor of 0.78; however, once a plastic hinge forms at the center of the panel (the region where the moment is highest), the transformation factor changes to 0.66. Scenarios where the support is redundant will have multiple load-mass factors as hinges begin to form in different locations. Tables are available with precalculated load and mass factors for typical scenarios (DoD 2008c); however, for unusual cases it will be necessary to calculate the necessary factors. For more information, see (PCI 2010a).

The load-mass transformation factors are multiplied by the mass, damping, resistance function, and the load of the classic equation of motion (Chopra 2007). Damping is often ignore in blast applications for simplicity. Additionally damping does not contribute much to the initial response during an impulsive load (Chopra 2007) and the main points of interest for a blast analysis are during the initial positive phase or negative phase response.

Once the resistance function of the component is calculated via a section analysis, and the load-transformation factors are determined given the loading scenario and boundary conditions and multiplied by their corresponding components in the equation of motion, the time-history of the component is calculated with standard dynamic approaches. In most cases, a close-formed solution is not available so numerical time-stepping approaches are utilized (Biggs 1964).

www.manaraa.com

By knowing the time-history response of the component, the amount of damage the component has received can be determined. The United States Army Corps of Engineers (USACE) has developed a system to correlate the panel response to amount of damage via experimental tests (USACE 2008a). For a secondary reinforced concrete flexural element, such as a non-loading bearing wall panel, the damage is correlated to either the ductility, μ, defined as the maximum deflection over the yield deflection, or the amount of support rotation, θ, calculated by the geometry. For a simply supported panel, the rotation is determined by the tan of the quotient of the maximum deflection at midspan and half the panel length. Table 3 provides the response correlated to damage received for a secondary flexural concrete element reinforced with either prestressing or non-prestressing (USACE 2008a).

Table 3: Allowable response limits (USACE 2008a)

Component Damage Level	PS	Non-PS
Superficial	$\mu \leq 1.0$	$\mu \leq 1.0°$
Moderate	$\theta \leq 1.0°$	$\theta \leq 2.0°$
Heavy	$\theta \leq 2.0°$	$\theta \leq 5.0°$
Hazardous	$\theta \leq 3.0°$	$\theta \leq 10.0°$

The SDOF analysis presented by (USACE 2008a) has been validated through experimental testing. The following sections outline an experimental validation of the SDOF method carried out in response to the 2012 ACI Blast Blind Simulation Contest (Olmati et al. 2014).

4.2. Experimental Validation of Analytical Approach

Blast loads are an important design load for any structure involved with the handling or manufacturing of volatile materials. In the case of military, government, and other high risk facilities, designing for a prescribed detonation is required. Unlike conventional design practice for natural hazards such as seismic events, where the earthquake load is

www.manaraa.com

applied as an equivalent static force, designing a building for a blast load must consider the dynamic event to prevent the structure from becoming prohibitively expensive.

Many methods are available to the design engineer to predict the performance of a structural component subjected to an explosive event. Numerical modeling can provide the user with a detailed response of the component but is generally time consuming to build, computationally expensive, and often requires a deep understanding of finite element methods and solid mechanics. Analytical modeling can provide the user with a quick method to calculate the response of the component, but results generally lack the detail available in numerical modeling.

The response of concrete structural elements to blast demands have been investigated by several authors, in the following are few examples. Davidson et al. (2005) investigated the failure mechanisms of reinforced concrete masonry walls reinforced by polymer sheets and then subjected to blast load. In Zineddin and Krauthammer (2007) normal concrete slabs were subjected to localized impact loads by a drop test machine. In Schenker et al. (2008) protected and unprotected concrete slabs are tested with a large hemispherical surface detonation of TNT. In Wu et al. (2009) a series of concrete slabs were tested in order to compare their blast resistance. In Naito et al. (2012) the behavior of precast concrete panels with an insulation layer to improve the thermal resistance of the panel is investigated, focusing on the shear ties connecting the two concrete layers confining the insulation layer.

The subject is current, and federal, industrial and academic affiliations (Giovino et al 2014, Naito et al. 2014) are interested in concrete structures subjected to impulsive loads as shown in the previous brief literature review. Several experimental tests are conducted in order to understand the fundamental parameters that lead the response of concrete

www.manaraa.com

structures under blast loads. FE and analytical simulations are also carried out in order to both reduce the experimental effort (cost) and provide useful tools for designing and assessing concrete structures under impulsive loads from the defensive and offensive points of view.

Generally the experimental and the simulated results agree (Trasborg et al. 2014b). However simulations and novel concrete constitutive models have to be constantly validated by the experimental evidence in order to be useful in predicting the response of concrete structure subjected to impulsive loads since, as mentioned, several numerical and analytical methods are available. The following section validates the accuracy of analytical modeling to analyze the behavior of reinforced concrete slabs under a blast demand with experimental tests by the means of data generated for the ACI Blast Blind Simulation Contest 2012 (Thiagarajan et al. 2010).

4.2.1. Experimental Program

The experimental program consisted of blast tests conducted in a shock tube at the Engineering Research and Development Center in Vicksburg, Mississippi on three reinforced concrete panels. The shock tube, shown in Figure 5, applies both the positive and negative phase of the pressure uniformly across the panel face. Pressures were recorded via pressure gauges at six different locations along the length of the panel. The pressure history for each panel is presented in Figure 5, where each curve is the average of the six pressure gauges. The first two specimens were tested under the pressure demand "PH-Set 1a" while the third specimen was tested under the pressure demand "PH-Set 1b". For modeling convenience, pressure data was simplified by averaging data points to the curves labeled "Load 1" and "Load 2" as shown in Figure 5. A laser deflection device was used to record the deflection history of each panel.

www.manaraa.com

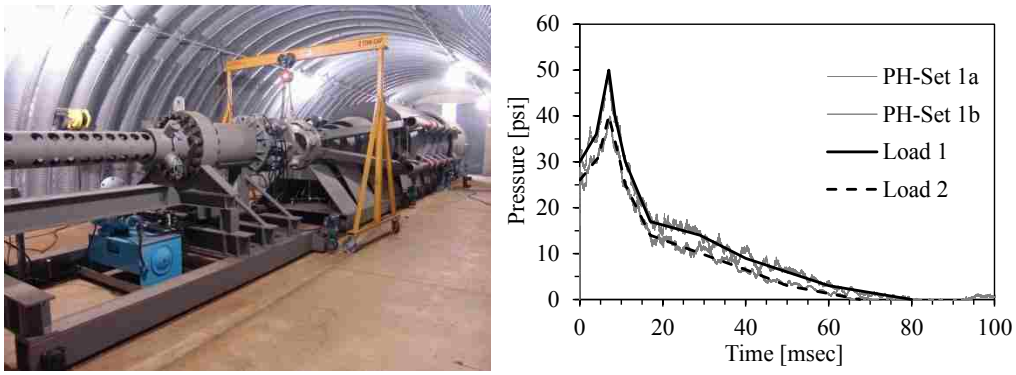

Figure 5: ERDC shock tube (ACI 2013) and pressure demands

The three specimens had identical reinforcement layout, dimensions, and material strengths. Panels were 64 in. (162.6cm) long by 33.75 in. (85.7cm) wide by 4 in. (10.2cm) thick. Each specimen consisted of nine #3 (#10) and five #3 (#10) grade 60ksi (420MPa) deformed reinforcing bars longitudinally and transversely placed as shown in Figure 6. For construction ease, longitudinal bars were tied directly to transverse bars and had 0.5 in. (1.3cm) of cover to the transverse bars, meeting ACI cover requirements for concrete not exposed to weather or in contact with ground (ACI 2011).

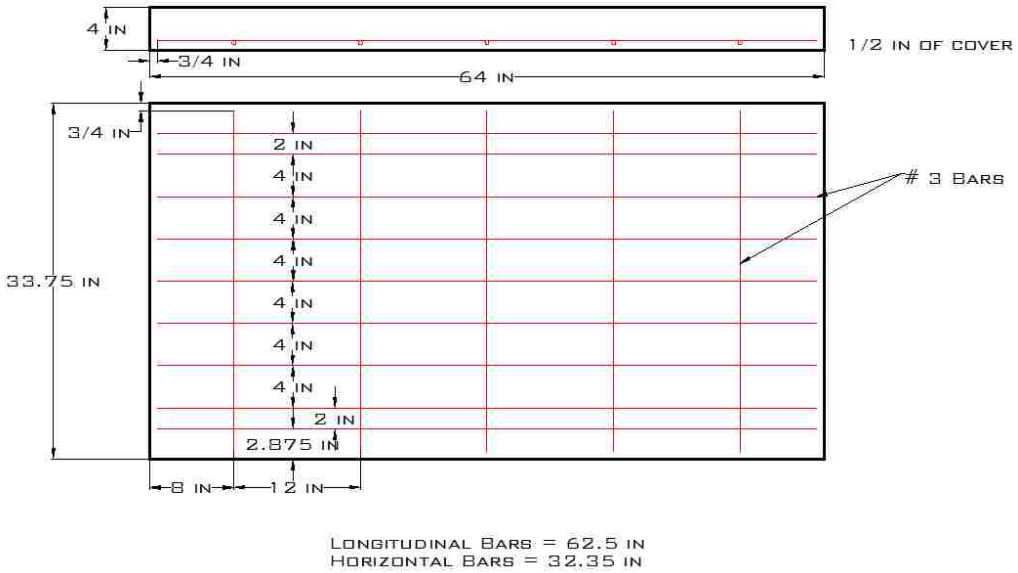

Figure 6: Panel dimensions and reinforcement layout

Each panel was simply supported by 6x8x5/8 in. (15x20x1.6cm) structural tube with

www.manaraa.com

3x3x5/16 in. (7.6x7.6x0.8cm) structural tube on the blast side face in order to prevent the overturning of the slab in the shock tube as shown in Figure 7. The framing supporting the panel is considered to be rigid for analytical modeling. A void was allocated between the two steel tube sections and the concrete slab in order to allow the slab to rotate to the extremities as shown in Figure 7. The gap between the 3x3x5/16 in. structural tube on the blast side face and the panel face was measured as 0.25 in. (6.35mm) in the construction drawings provided (determined by scaling the construction drawing and calculating the gap size); however, to improve the accuracy of the predictive models, the gap was adjusted to 0.35 in. (8.89mm), see next sections.

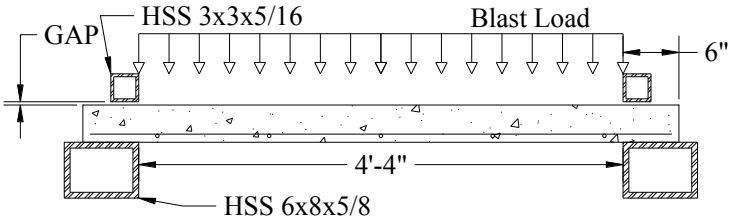

Figure 7: Panel restraints and as built dimensions used for modeling

4.2.2. SDOF Modeling

The analytical modeling is conducted using the single-degree-of-freedom (SDOF) method (Olmati et al. 2013). The SDOF approach with a uniformly distributed pressure load is assumed to be adequate to properly model the panel behavior subjected to the shock load generated by the shock tube. The model material properties, shock wave magnitude and duration are based on information obtained through destructive material tests and pressure gauges located in the shock tube.

DIFs for concrete and steel reinforcement are accounted for by performing an iterative SDOF analysis. The SDOF analysis is first conducted using static constitutive material properties. The strain rates of the concrete and steel are determined by the quotient of the

www.manaraa.com

yield strain of the respective material and the time required for the component to reach the deflection at which the respective material yielding occurred. DIFs were determined by substituting the strain rates in the Murray (2007) model for concrete and the Cowper-Symonds (1957) model for 60ksi (420MPa) steel as shown in Figure 8. The SDOF process is repeated until the DIFs in the current SDOF analysis converged with those from the previous SDOF analysis. Final DIFs for concrete in compression and tension are found to be 1.05 and 1.8 respectively (since in the SDOF analysis the inertial confinement due to the high rate load is not taken into account, the opportune DIF should be provided). Similarly, the DIF for the reinforcing steel is found to be 1.4.

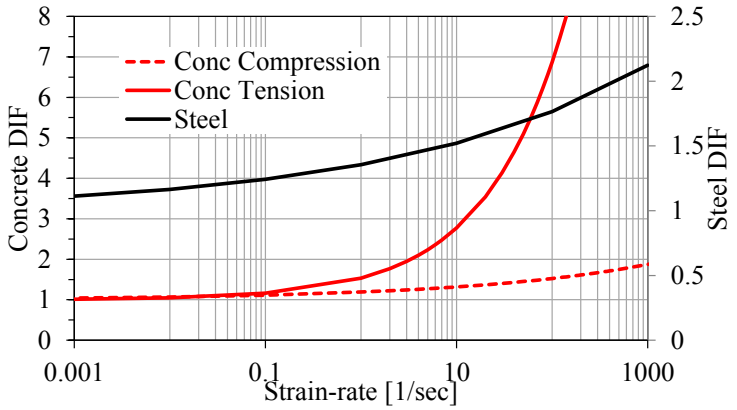

Figure 8: Concrete and steel DIF models

The constitutive models shown in Figure 9 depict both the static experimental material data as solid lines and the models with DIFs as dashed lines. The concrete experimental data is found to match Popovics' model (1973) well until a strain of approximately 0.01. Concrete strains past 0.01 are modeled by a linear regression, labeled as the "Mod (Modified) Popovics" in Figure 9. The concrete model stress values are adjusted by the multiplicative DIF for concrete provided in Figure 8 as shown by the dashed line in Figure 9. Although the concrete model utilized is able to carry tension, the tensile capacity of the concrete is

www.manaraa.com

not shown in Figure 9 as the magnitude of the tensile strength adjusted by the corresponding DIF relative to the compressive strength is very small (less than 10%). The stress-strain steel curve obtained through tensile tests is discretized to a multi-linear relationship to facilitate modeling. The steel reinforcement DIF is applied in a manner such that the original elastic modulus remained the same.

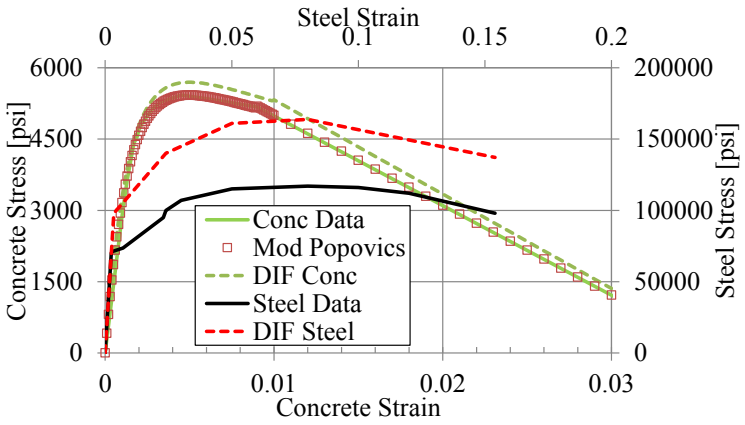

Figure 9: Material constitutive models (1000 psi = 6.89MPa)

A fiber analysis (Trasborg et al. 2014b) is performed in order to obtain the moment-curvature relationship of the slab as provided in Figure 10. Due to the placement of the reinforcement as shown in Figure 6, the negative flexural capacity of the slab is lower than the positive flexural capacity. The non-symmetric moment-curvature behavior was important to consider as the panel moment distribution changes from negative to positive when the gap at the BCs close and the condition changes from pinned to fixed.

www.manaraa.com

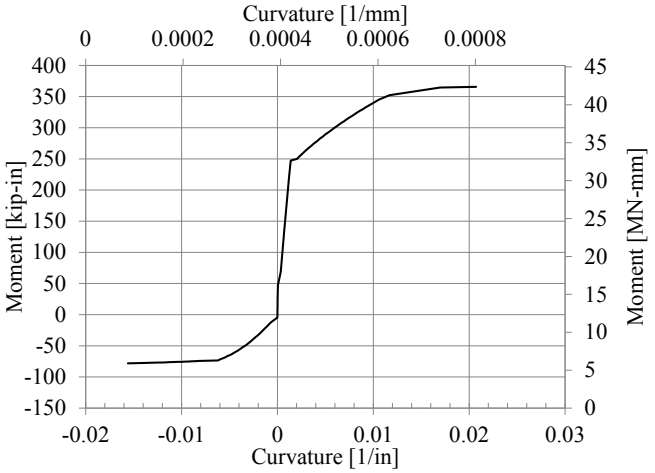

Figure 10: Moment-curvature relationship

Similarly to the numerical model, a gap of 0.25 in. is initially assumed between the slab face on the blast load side and the structural tube as shown in Figure 11. The model gap is later changed to 0.35 in. to improve the accuracy of the model when compared to the experimental data. Initially the slab is modeled with simple-simple supports; however, after a given amount of rotation, θ, the ends of the panel begin to contact the upper supports where the model BCs are more appropriately modeled as fixed-fixed supports. With increasing θ, a plastic hinge forms at the center of the panel, causing the panel to effectively behave as two cantilevered beams. Finally, hinges forms at the ends of the panel creating a mechanism where the panel deflects continuously at a constant load. Utilizing methods discussed in detail in Biggs (1964) the panel can be simplified to a SDOF model. The method utilizes transformation factors based on assumed panel response. The transformation load-mass factor (KLM) for each BC is determined by taking the quotient of the load factor and the mass factor. The progression of BCs and their corresponding KLM factors are shown in Figure 12.

www.manaraa.com

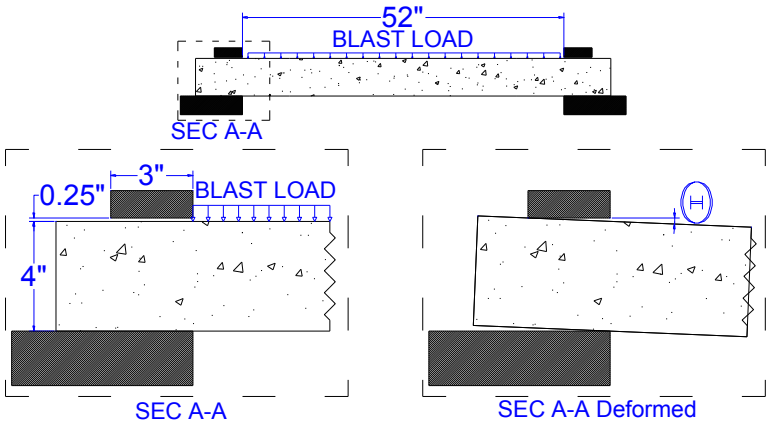

Figure 11: Slab BCs during loading

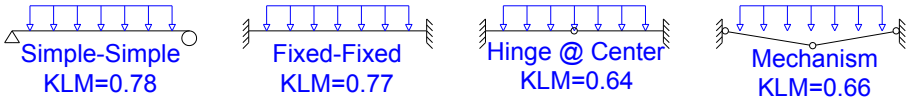

Figure 12: Progression of BCs

From the moment-curvature relationship shown in Figure 10, the curvature over the length can be determined by utilizing the BCs and the applied load. Numerically integrating the curvature distribution with a virtual moment allows for the calculation of the load-displacement of the slab. The BCs of the slab are a function of the panel deflection which is a function of the load-history; thus the relationship between the moment-curvature and the curvature over the length is also a function of the load-history. From geometry (assuming the panel is rigid and hinges about the center), the panel is calculated to change from simple-simple BCs to fixed-fixed at approximately 3.03in. (77.1mm) of deflection. At each change in the panel BCs, the moment distribution and curvature over the length are saved. The results at the conclusion of each BC transition are then summed, creating the resistance-deflection curve shown in Figure 13.

The analytical model is also updated with an increased gap size of 0.35 in. (8.89 mm) between the panel face on the blast side and the structural tube section referred to as "updated" in Figure 13, while "original" refers to the model with the original 0.25 in.

www.manaraa.com

(6.35mm) gap. For modeling convenience, the resistance function of the panel was simplified to a multi-linear backbone curve, referred to as "Model Input" in Figure 13. The backbone curve is developed in accordance with the procedure presented in Naito and Ren (2013).

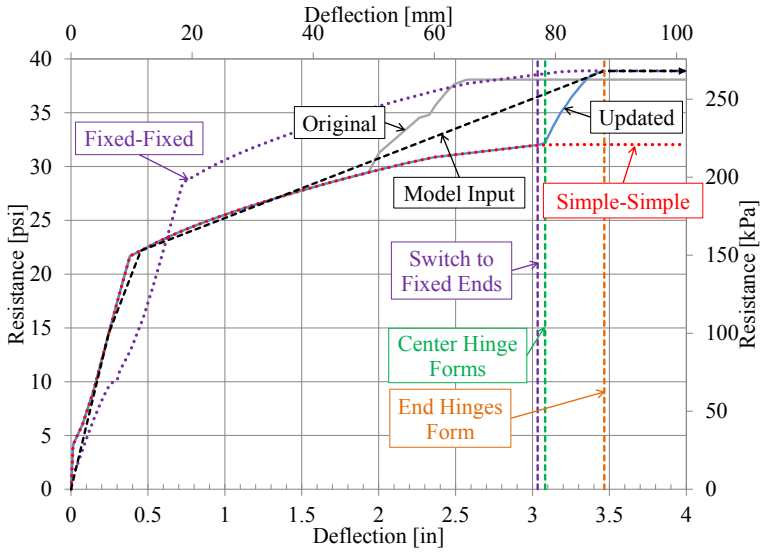

Figure 13: Panel resistance-deflection relationship

Component damping is neglected as damping does not have a large contribution to maximum or residual displacements for highly impulsive loads. Due to ease of implementation and unconditional stability, the constant velocity method described by Biggs (1964) was used to solve the differential equation of motion. In regions with sudden change of slope in the resistance function (e.g. yielding of the reinforcement and BC changes) "overshoot" is avoided by using very small time steps. A time step of 0.05 msec was found to be suitable in this case.

4.2.3. Experimental and Analytical Comparison

Time history results for the panel with various BCs subjected to Load 1 are shown in Figure 14. The condition when the BCs change from simple to fixed has been named

www.manaraa.com

"adaptive boundaries". "Simple-simple" refers to a panel that is simply supported throughout the load history while "fixed-fixed" refers to a panel that starts with fixed-fixed BCs until hinges form at the restraints. As expected, the fixed-fixed BCs lead to the stiffest panel while the simple-simple BCs lead to the most flexible panel. The panel with adaptive boundaries is considered to most accurately represent the actual restraint conditions during testing.

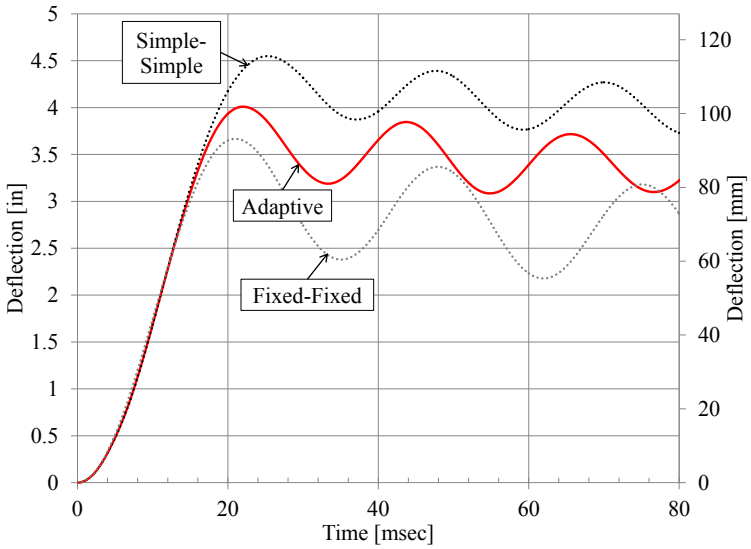

Figure 14: Time-history

Permanent deflection (average residual) is calculated by averaging all the points after 30 msec. Table 4 presents the final analytical results as well as the experimental results while Figure 15 provides the final time-history for the panel subjected to Load 1 and Load 2. The gap between the structural tube and the blast side face of the panel is changed to 0.35 in. (8.89mm) from 0.25 in. (6.35mm) as shown in Figure 7. The analytical model corresponding to a gap of 0.25 in. (6.35mm) is referred to as "original" in Figure 15, while the analytical model with a gap of 0.35 in. (8.89mm) is referred to as "updated". As expected, the updated model was more flexible than the original model as the "fixed-fixed" BC transition occurs at a later displacement. Finally, the models with updated BCs provide

www.manaraa.com

the best match to the experimental data for both Load 1 and Load 2.

Table 4: Analytical model versus experimental results

	Demand = Load 1		Demand = Load 2	
	Model	Experiment	Model	Experiment
Max Deformation [in. (mm)]	[4.010 (101.9)]	[4.371 (111.0)]	[2.804 (71.21)]	[3.170 (80.52)]
Time of occurrence of max deformation [msec]	22.00	31.34	20.45	23.36
Residual deformation [in. (mm)]	[3.395 (86.22)]	[3.656 (92.87)]	[2.353 (59.76)]	[2.131 (54.13)]

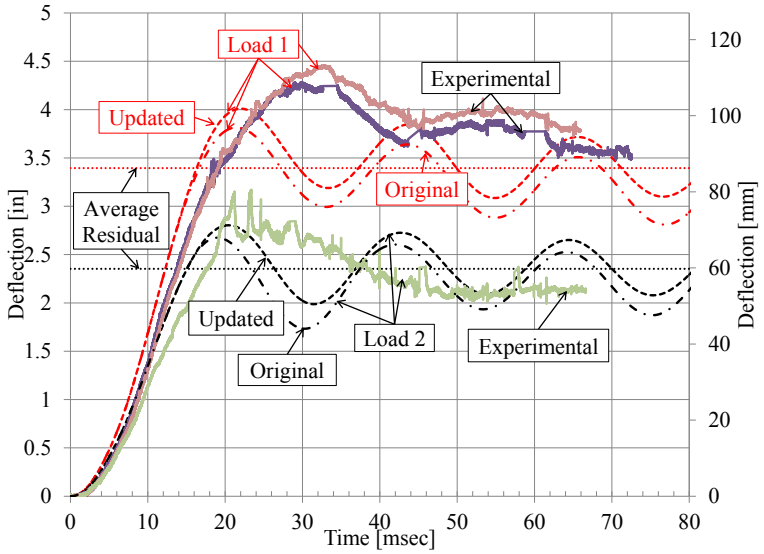

Figure 15: Analytical versus experimental results

4.2.4. SDOF Conclusions

To highlight the efficacy of analytical models to predict the response of reinforced concrete structures subjected to impulsive loads, the present work shown both finite element and SDOF simulations carried out to predict the deflection-time history of the slabs tested (referred to as normal slab, category 3 ACI Blast Blind Simulation (Thiagarajan et al. 2010)). The accuracy of analytical model presented in this paper were assessed by comparing the predictions to the experimental results.

The call of the contest mentions (Thiagarajan et al. 2010): *"Several factors contribute to the prediction of the response of a structure when subjected to shock/blast loading. These*

www.manaraa.com

factors include boundary conditions, complexity of material properties available, material models used and finite element parameters such as element type selection, mesh size sensitivity, material model rate effects amongst others. There are a number of concrete material models developed by several researchers over the past few decades for both static and dynamic loading and the primary objective of this contest it to evaluate their effectiveness under blast/shock loading". The reported analytical model presents an accurate, practical approach that can be used to predict the response of concrete structures subjected to impulsive loads. The following conclusions have been made based on the work presented:

- A fiber analysis can provide an accurate prediction of the moment-curvature for a reinforced concrete slab given the material properties of the reinforcement and concrete as well as the geometry of the panel and placement of the reinforcement.
- Moment-curvature analysis can be used for the prediction of the resistance function for a reinforced concrete slab with varying boundary conditions. Boundary conditions can be adjusted as the panel deflects in an analytical model if the panel response is carefully monitored and saved at each boundary condition transition.
- Single degree of freedom analysis can provide an accurate prediction of the time-history response of a reinforced concrete slab subjected to a blast load when given the duration and magnitude of the load, assuming the loading is uniform on the surface of the panel.

www.manaraa.com

- Analytical methods provide comparable results to the experimental results, indicating that analytical methods are suitable for a quick check when more time consuming and computationally expensive numerical methods are not available.

4.3. Flexural Mechanism Development

To improve the response of wall panels to blast loading, the flexural response of thin, reinforced concrete components need to be improved. As a result, new flexural mechanisms were devised which are outlined in the following sections.

4.3.1. Flexural Mechanism Background

Precast concrete panels are often used for exterior cladding of buildings due to their aesthetic appeal, quick erection time, and economic design. These systems can be used to minimize environmental impact and increase sustainability, since thin insulated concrete wall panels increase thermal resistance without drastically increasing the overall cost. While these wall panels are often designed for conventional handling, construction, and service loads, in many cases extreme loading conditions must be considered. Most federal buildings, military facilities, explosive storage and manufacturing structures, and many industrial buildings require that the structure be able to withstand a prescribed detonation for both accidental and intentional scenarios. This blast load can create a dynamic reflected pressure resulting in large out-of-plane demands on the building. To be effective against these demands, exterior walls must have substantial out-of-plane deformation capacity and ductility. For a non-load bearing, reinforced concrete element in flexure, such as a wall panel, the US Army Corps of Engineers (USACE) requires that the component be able to reach a support rotation of 10º prior to blowout (US Army 2008).

According to ACI 318-11 R10.3.4, tension-controlled members will provide ductile

www.manaraa.com

behavior for designs where unusual amounts of ductility are not required. In order for a reinforced concrete section to be classified as tension-controlled, at nominal capacity the strain in the extreme tensile reinforcement, ε_t, must be equal to or greater than 0.005 (ACI 318-11). Use of a tension controlled section allows for a larger strength reduction factor, thus wall panels are often designed to meet the tension-controlled section criteria.

A panel that is tension controlled at nominal capacity may still fail at relatively low deformation limits. Consequently, the use of a tension-controlled panel does not ensure that the deformation/ductility capacity is enough to meet the requirements set by the USACE. Experimental tests conducted by (Naito et al. 2011b) showed that the ductility capacity of thin insulated concrete panels that met the tension control criteria were limited due to crushing of the concrete in the compression zone. This concept can be further illustrated by numerical evaluation of conventionally reinforced panels that meet ACI 318-11 R10.3.4 tension control criteria.

A series of fiber analyses are conducted on a standard reinforced concrete section. The section geometry, reinforcement depth, and concrete properties are kept constant for all cases. The reinforcement ratio, ρ, is varied from a section just meeting the tension control limit strain of 0.005 to one with a tension strain of 0.057 at the nominal flexural capacity. The fiber analysis approximates the cross section geometry by dividing the section into discrete fibers (Kaba, Mahin 1984). Each fiber is assigned an area, force-deformation relationship and compatibility relationship with other fibers. For simplicity, reinforcement layers are imposed on a single fiber layer despite diameter size. In the fiber model, strains at the extreme compressive fiber of the cross section are gradually increased, thus changing the strains in each fiber according to the assigned compatibility relationship. Once the strains on the compressive face reach a point where force equilibrium can no longer be

www.manaraa.com

satisfied, or a constitutive relationship reaches the maximum allowable value such as rebar fracture, the analysis is terminated. The fiber analysis produces a moment-curvature relationship for the section. By knowing the boundary and loading conditions of the specimen, in this case simply supported with a point load at center span, curvature over the length of the section is formulated. Finally, by numerically integrating curvature over the panel length the load-deflection curve is determined.

The ultimate deformation of a conventionally reinforced panel is dependent on the activation of the tension reinforcement. Figure 16 illustrates the load deformation response of nine panel designs, all of which according to ACI are tension controlled. The deformations are normalized to support rotation in accordance with USACE (US Army 2008). As illustrated, a section designed to be tension controlled at nominal moment capacity, designated by the filled squares, does not ensure large deformability. Even sections designed to fracture the tension reinforcement at failure, depicted by the curves below the shaded area, are still limited to rotations less than 10º.

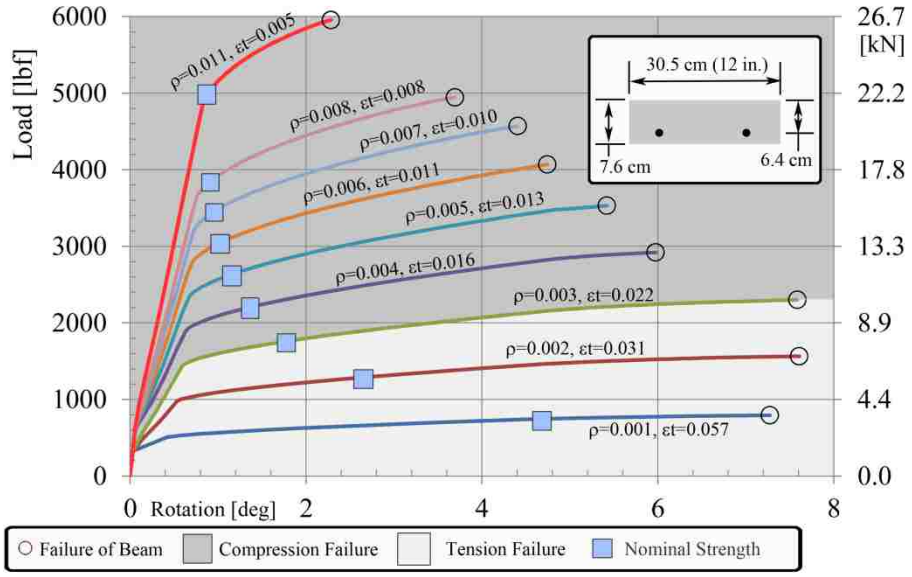

Figure 16: Load-rotation for various reinforcement ratios

www.manaraa.com

The issue arises of how to increase the deformation capacity of a wall panel while maintaining a thin profile. In order to achieve this goal without modifying the material property of the concrete, two alternative methods to establish a ductile failure mechanism in a thin concrete panel, allowing for support rotations equal to or greater than the 10º threshold required by the USACE are examined. Additionally, the failure mechanisms are predictable, allowing for accurate modeling of the panel behavior up to failure.

4.3.2. Research Significance

During extreme loading events, such as a blast loading, the exterior cladding components provide the first line of protection to the integrity of the structure and the occupants. Increasing the deformation capacity of reinforced concrete wall panels in a constructible and predictable manner is desirable for improving the resilience to blast events. Two methods to increase wall panel ductility are developed and presented in this paper. The analytical methods provided are based on first principles and can be readily adopted for design of blast resistant wall panels. It is important to note that the tests conducted in this paper were performed at static rates, under blast demands the system would be subject to dynamic rate of loading. Under high strain rates, the yield point of steel increases, the modulus remains the same, the ultimate strength is marginally increased, and the fracture strain remains unchanged or is slightly reduced (DoD 2008c). Consequently, the use of static test data provides a conservative estimate when used in blast assessment.

4.3.3. Flexural Mechanisms

The two ductile mechanisms explored in this paper are shown in Figure 17. The "Dogbone Joint" method involves attaching steel members to the exterior of the tensile face of the panel, while the "Unbonded Reinforcement" method relies on emulative reinforcement detailing.

www.manaraa.com

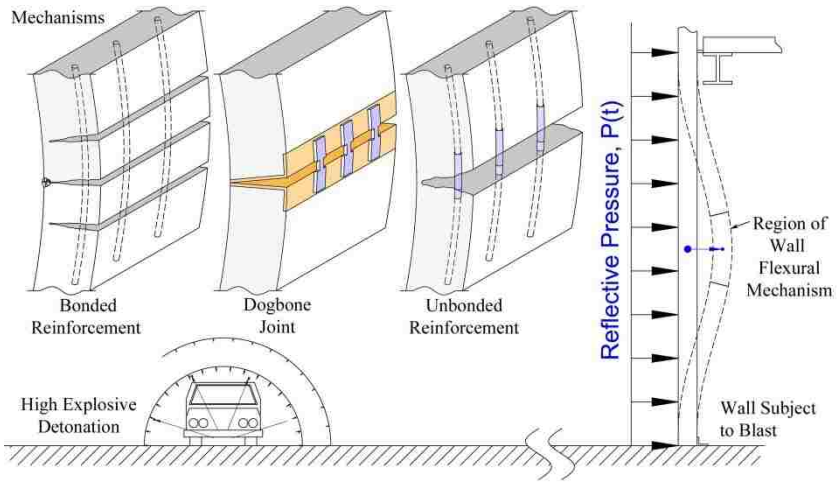

Figure 17: Flexural mechanisms in thin reinforced concrete panels

Wu has made an attempt at improving the response of a thin RC element through a method of compression yielding in which a specially designed steel member is embedded in the concrete (Wu 2006). Rather than relying on the compression strength of the concrete, the RC element's strength and ductility is derived from the performance of the steel member embedded in the compression zone. Similar to Wu's work, a method to examine the effect of creating a hinge mechanism at midspan of the panel was investigated (dogbone joint in Figure 17). The dogbone concept presented has been successfully used in seismic applications to provide reliable damage locations (Plumier 1997); however, the application has not been used in RC wall elements to improve out of plane ductility.

A dogbone panel was detailed to achieve a predictable flexural response. To achieve this, a joint was created in the panel at the region of maximum moment (i.e., midspan for a simply supported, single span panel under a point loading at the center). The joint consisted of a steel angle embed running the width of the panel. The angles were anchored to the concrete via 2 longitudinal rebars welded to each interior angle face. The two angles (and hence concrete sections) were then connected by welding specially designed steel

www.manaraa.com

"dogbone" members to the exposed side (tensile face or interior wall face) of each steel angle. A 12.7 mm (0.5 in.) long, 4.8 mm (0.2 in.) wide weld was applied to each of the two corners along the compression face edges of the steel angles to provide stability during handling and ensure the mechanism will hinge about the compression edges. To resist the flexural demands the dogbones act in tension while the angles bear on one another along the compression edges, creating a moment-couple that governs the global resistance of the panel. The dogbone cross-section was designed such that the dogbones would yield under the flexural response of the wall prior to reaching the tensile capacity of the angles or reinforcement. The length of the dogbone was chosen to control the amount of joint opening and hence the global deflection of the panel. To utilize the dogbone method in practice, design details would need to be considered to simplify construction.

The unbonded reinforcement method created a localized mechanism over the unbonded length. Localized unbonded methods have been successfully used for beam-column connections in seismic applications (El-Sheikh et al. 2000); however, this is the first time locally unbonding has been utilized in RC wall panels to improve out of plane deformation capacity. Unlike the dogbone method, the unbonded method was emulative, requiring little additional fabrication effort. The flexural reinforcement was locally unbonded from the surrounding concrete via Teflon tubing at midspan. In contrast to loading a conventionally reinforced panel that forms a distributed crack pattern, the unbonded panel was anticipated to form a single crack in the region of maximum moment. This is due to the fact that the tensile bond stresses developed between the reinforcement and the concrete necessary for crack formation are not present in an unbonded panel (Park, Paulay 1975). As the unbonded panel is loaded, the reinforcement will have uniform strain over the entire unbonded length rather than over a discrete crack width. Similar to local unbonding, tests

www.manaraa.com

on beams reinforced with undeformed reinforcing bars hooked at the ends exhibited near constant stress over the portion between the hooks (Mains 1951). Figure 18 depicts the difference in reinforcement strain between a bonded and unbonded panel. For a given displacement, a smaller original length over which the rebar stretches leads to larger strains; as opposed to the same rebar, at the same displacement level, straining over a larger original length.

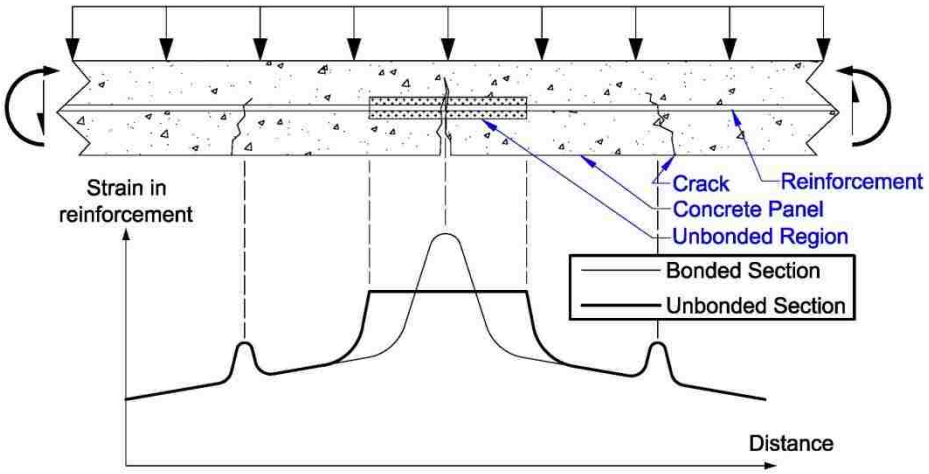

Figure 18: Bonded panel versus unbonded panel reinforcement strain

In order to maintain equilibrium, an equivalent compressive force must balance the tensile force; consequently, the larger the force in the tensile reinforcement, the larger the force in the concrete compression zone. By straining over a larger original length, the strains and thus the forces in the rebar are reduced, thus delaying crushing of the concrete in the compression zone, allowing larger ultimate displacements to be reached. Decreasing the compressive force also decreases the panel's maximum moment capacity due to the decreased force couple. Furthermore, unbonding the longitudinal reinforcement will soften the post cracking stiffness of the panel as the rebar bond is not present to slow the propagation of the crack formed at center span.

www.manaraa.com

4.3.4. Experimental Program

To assess the performance of the dogbone and unbonded panels, conventionally reinforced panels were fabricated, creating a total of eighteen panels tested to failure. To isolate experimental variables between specimens, the longitudinal and transverse reinforcement types and locations were consistent among each specimen type. Generic panel details are illustrated in Figure 19. Fully bonded panels with continuous longitudinal reinforcement served as the control group. The control panel design was selected based on a single wythe of specimen TS2 tested in (Naito et al. 2011b); however, to prevent shear failure from controlling, the depth of the longitudinal reinforcement was increased from 38.1 mm (1.5 in.) to 63.5 mm (2.5 in.) in order to increase the panel shear capacity. Local unbonding was achieved with 0.79 mm (0.03 in.) thick Teflon tubes placed over the rebars at center span. The thickness of the Teflon tubing was selected to prevent bar deformations from protruding, thus eliminating any effect of mechanical interlocking of the rebar and surrounding concrete. Three unbonded lengths were chosen (20, 40, and 60 bar diameters), where the $20d_b$ unbonded length was selected based on the requirement of 10º support rotation. The elongation needed for the unbonded reinforcement was approximated by the product of twice the support rotation and the reinforcement depth. The required unbonded length was then determined from the calculated bar elongation and the reinforcement strain at ultimate, provided through tensile tests. The experimental test matrix is provided in Table 5.

www.manaraa.com

Table 5: Test matrix		
Panel Name	Quantity	Length of Unbonding
Control	6	0
Unbond 1	3	$20d_b$
Unbond 2	3	$40d_b$
Unbond 3	3	$60d_b$
Dogbone	3	0

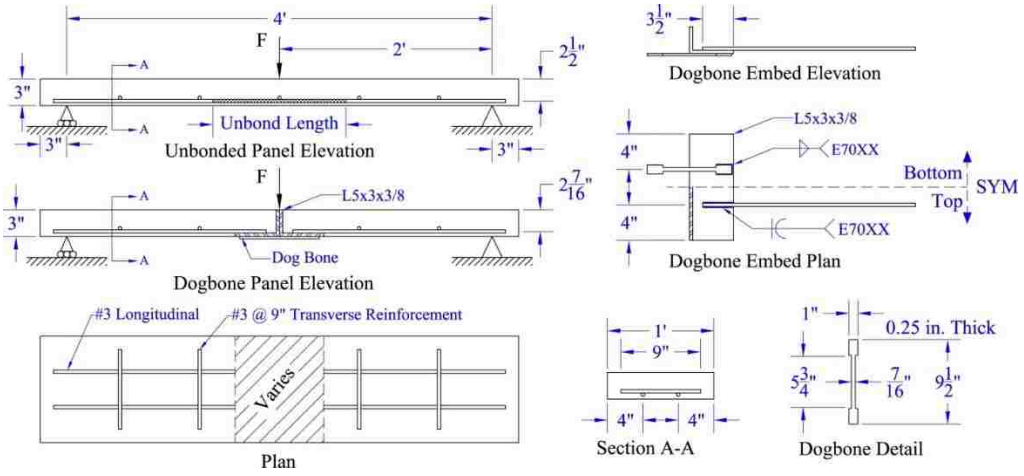

Figure 19: Panel layouts [1 in. = 25.4 mm]

Panels were monotonically loaded to failure via a displacement controlled line load applied at center span. The panels were simply supported with a roller free to move at one end and a clamped roller at the other. Stroke of the testing apparatus allowed the panels to reach a maximum support rotation of approximately 30º. Linear variable displacement transducers were placed at midspan on both sides of each panel to determine an average center span displacement.

Material strengths of the panels were determined by evaluating available reinforcement and concrete samples. Tensile testing of steel samples was conducted in accordance with ASTM E8-04 and ASTM A370-12. The elastic modulus, yield stress, ultimate stress,

www.manaraa.com

fracture strain, and a full stress-strain curve were determined through a series of tensile tests on reinforcement and dogbone members. All transverse and longitudinal reinforcement for the control and unbonded panels were ASTM A615-09 Gr.420 (Table 6) and ASTM A706 Gr.420 for the dogbone panels due to the welding detail. The dogbone members were fabricated from ASTM A572 Gr.345 6.35 mm (0.25 in.) flat plate (Table 6). Concrete compressive strength was evaluated in accordance with ASTM C39 and C469 (Table 7). Stress-strain curves for concrete were determined experimentally through the use of a 102x203 (4x8) cylinder compressometer collar. The concrete stress strain response was approximated using Popovics' model (Popovics 1973).

Table 6: Steel material properties

Property	A615 Gr.420	A706 Gr.420*	A572 Gr.345
Modulus GPa (ksi)	206.8±38.6 (30000±5600)	200 (29000)	N.A.
Yield Stress MPa (ksi)	485.4±8.3 (70.4±1.2)	452.3 (65.6)	377.1±4.8 (54.7±0.7)
Yield Strain	0.18%	.23%	N.A.
Ultimate Stress MPa (ksi)	734.3±6.2 (106.5±0.9)	650.2 (94.3)	513.7±5.5 (74.5±0.8)
Ultimate Strain	10.5%	N.A.	16.3%
Fracture Stress MPa (ksi)	N.A.	N.A.	357.8±2.8 (51.9±0.4)
Fracture Strain	18.9%	N.A.	27.2%
* Data from mill certification			

Table 7: Concrete properties

Property	Cylinder Data
Elastic Modulus GPa (ksi)	13.3 (1900)
Compressive Strength MPa (ksi)	31.8 (4.6)
Strain at Comp. Strength	0.46%

The constitutive properties of the concrete and steel are illustrated in Figure 20. The solid lines signify average experimental data curves while dashed lines signify approximate

www.manaraa.com

curves utilized in numerical and analytical models. Due to a malfunction in the testing apparatus, only one cylinder stress-strain curve was utilized. Popovics' model was cut off at a strain of 0.022 to coincide with the cylinder test data.

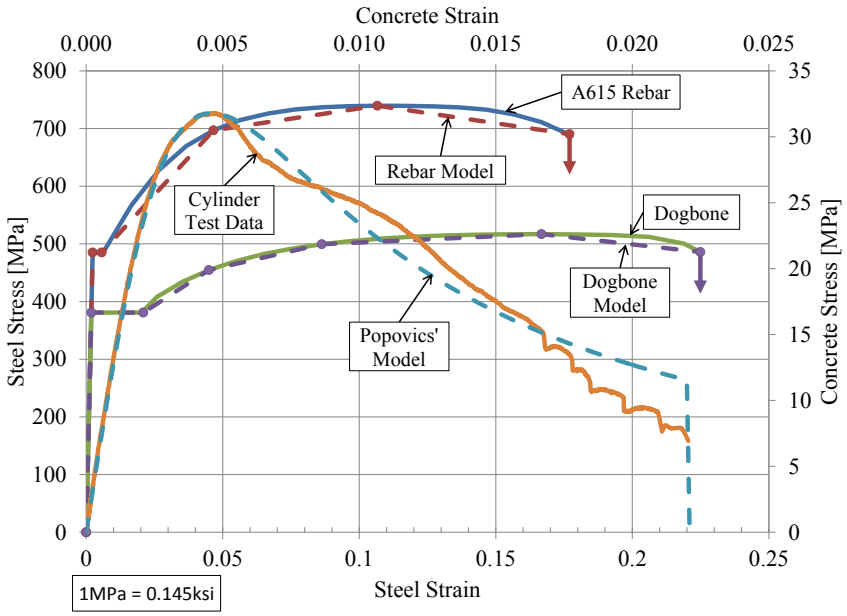

Figure 20: Steel and concrete stress-strain curves

The panel load–deflection results are summarized in Table 8. Force-rotation curves for the control panels are provided in Figure 21. The average response for each panel group was computed by averaging the force level of each panel at each given rotation interval. Figure 22 summarizes the average response of each specimen group, i.e. control, dogbone, $20d_b$, $40d_b$ and $60d_b$.

www.manaraa.com

Table 8: Summary of measured panel response						
Specimen	Max Load kN (kip)	Max Moment kN-mm (kip-in)	Deflection @ Max Load mm (in)	Rotation @ Max Load deg	Final Deflection mm (in)	Final Rotation deg
Control 1	17.7 (4.0)	5378 (48)	34 (1.3)	3.2	79 (3.1)	7.4
Control 2	17.4 (3.9)	5299 (47)	35 (1.4)	3.3	71 (2.8)	6.8
Control 3	18.3 (4.1)	5581 (49)	45 (1.8)	4.3	168 (6.6)	15.8
Control 4	18.5 (4.2)	5627 (50)	46 (1.8)	4.3	130 (5.1)	12.6
Control 5	18.0 (4.0)	5491 (49)	32 (1.3)	3.0	135 (5.3)	3.7
Control 6	19.0 (4.3)	5807 (51)	51 (2.0)	4.8	140 (5.5)	13.3
Dogbone 1	18.4 (4.1)	5604 (50)	82 (3.2)	7.7	102 (4.0)	9.6
Dogbone 2	18.5 (4.2)	5638 (50)	69 (2.7)	6.5	91 (3.6)	8.7
Dogbone 3	18.6 (4.2)	5672 (50)	79 (3.1)	7.4	102 (4.0)	9.5
$20d_b$ Unbond 1	16.2 (3.6)	4937 (44)	97 (3.8)	9.2	145 (5.7)	13.7
$20d_b$ Unbond 2	16.2 (3.6)	4949 (44)	121 (4.8)	11.4	175 (6.9)	16.8
$20d_b$ Unbond 3	17.9 (4.0)	5446 (48)	83 (3.3)	7.8	137 (5.4)	12.9
$40d_b$ Unbond 1	15.6 (3.5)	4745 (42)	135 (5.3)	12.9	201 (7.9)	19.1
$40d_b$ Unbond 2	14.7 (3.3)	4485 (40)	118 (4.6)	11.2	231 (9.1)	22.2
$40d_b$ Unbond 3	14.3 (3.2)	4373 (39)	119 (4.7)	11.3	196 (7.7)	18.8
$60d_b$ Unbond 1	14.8 (3.3)	4508 (40)	160 (6.3)	15.2	295 (11.6)	28.9
$60d_b$ Unbond 2	14.4 (3.2)	4395 (39)	16 (0.6)	1.5	249 (9.8)	24.1
$60d_b$ Unbond 3	13.4 (3.0)	4090 (36)	111 (4.4)	10.5	254 (10.0)	24.5

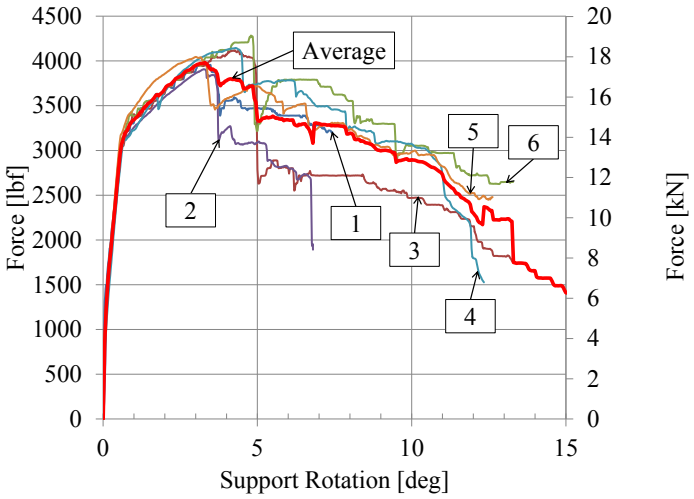

Figure 21: Control panel performance

www.manaraa.com

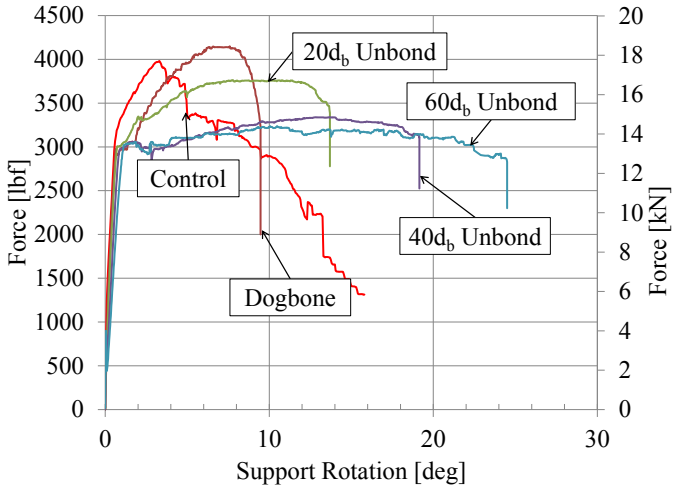

Figure 22: Panels averaged about the applied force

The six control panels tested in this program were of identical geometry and layout. All control panels exhibited similar behavior and failure mechanisms. Multiple shear-flexure cracks formed near midspan of the specimens and propagated upwards towards the loading head. The panels displayed a bilinear response consisting of an elastic regime followed by a hardening response, until approximately 17.8 kN (4.0 kip) at 4.0º of support rotation when the compression zone crushed, thus forming a mechanism leading to a continuous drop in the panels' resistance.

Three identical dogbone panels were tested in this experimental program. All dogbone panels exhibited similar behaviors and failure mechanisms. As each dogbone panel was loaded, the steel angle inlays at midspan began to open at the tensile face and hinge about the compression edge, forcing the load to be transferred primarily through the dogbone members in a combination of bending and axial force. The initial stiffness of the dogbone panel was decreased due to stretching of the reinforcement anchoring the steel angles. On average, the dogbone panels achieved a maximum load of 18.5 kN (4.2 kip) and an ultimate support rotation of 9.8º. As designed, the failure of each dogbone panel was

www.manaraa.com

characterized by yielding and fracture of the steel dogbone members at the necked region. The bending force acting on the dogbone at the edge of each angle inlay in conjunction with the axial force generated from the opening of the hinge caused the dogbone members to fail before the panels reached 10º of rotation. Detailed analysis of the failure of the dogbone panel is provided in the analytical modeling section.

The nine locally unbonded panels tested in this experimental program differed only in the unbonded length. Unlike the control panels, the unbonded panels formed only a single flexural crack at center span. As expected, locally unbonding decreased the post cracking stiffness due to the lack of bond to prevent crack propagation. Additionally, maximum resistance of unbonded panels was lower than the conventionally bonded panels due to the decrease in the tension-compression moment arm. At smaller displacements, the strain in the longitudinal reinforcement was controlled by axial stress; however, as the panel continued to deflect, bending stresses became more significant. The coupling of bending and axial stress led to fracture of the longitudinal reinforcement while allowing the compression zone to remain intact. The loading setup, control, dogbone, $20d_b$, $40d_b$, and $60d_b$ panels at ultimate displacement are shown in Figure 23.

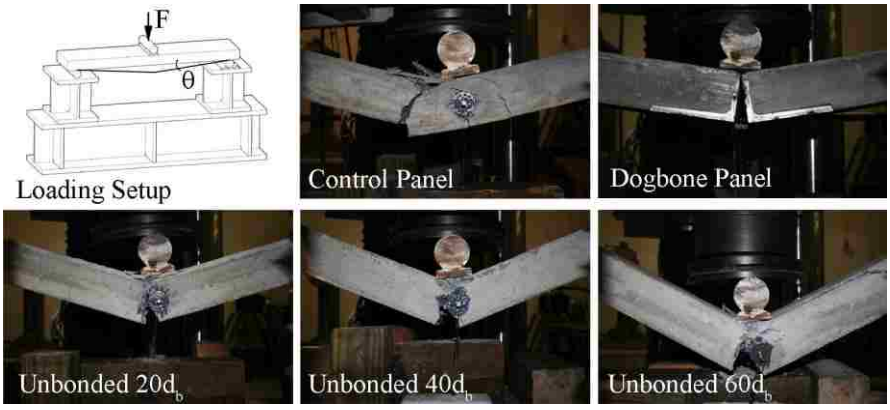

Figure 23: Loading setup and panels at ultimate

www.manaraa.com

4.3.5. Analytical and Numerical Modeling

The measured control, dogbone and unbonded panels are compared with numerical and analytical approaches for estimating response. The control is compared to a fiber analysis approach, the dogbone to a basic analytical approach and the unbonded system to a numerical approach.

Control Panel Performance

To predict the response of the control panel, a fiber analysis was performed (in accordance with the method previously discussed) on the cross section utilizing the material properties from Figure 20. Figure 24 illustrates the results of the fiber analysis against bounded experimental results of the control panel. The fiber analysis indicates that the numerical approach provides an accurate estimate of reinforced concrete panel response. Additionally, the approach justifies the concept of limited ductility when subject to out of plane demands due to failure of the concrete rather than fracture of the rebar.

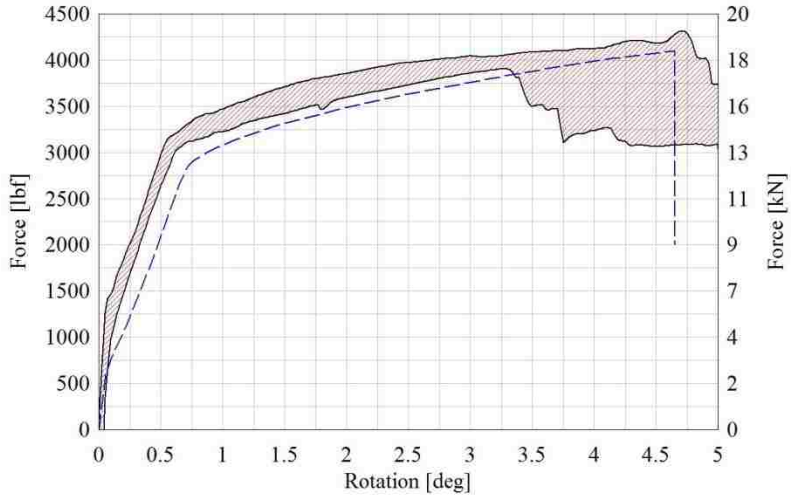

Figure 24: Fiber analysis (dotted) versus bounded experimental results

www.manaraa.com

Dogbone Panel Performance

The flexural response of the panel is primarily dependent on the axial deformations of the dogbones as the joint opens; however, the dogbone is also subjected to flexure as illustrated in Figure 25. The combination of axial and bending stress reduces the ductility of the dogbone panel. By utilizing constitutive relations, equilibrium, and compatibility, both of these mechanisms can be accounted for to determine the force-rotation response of the panel.

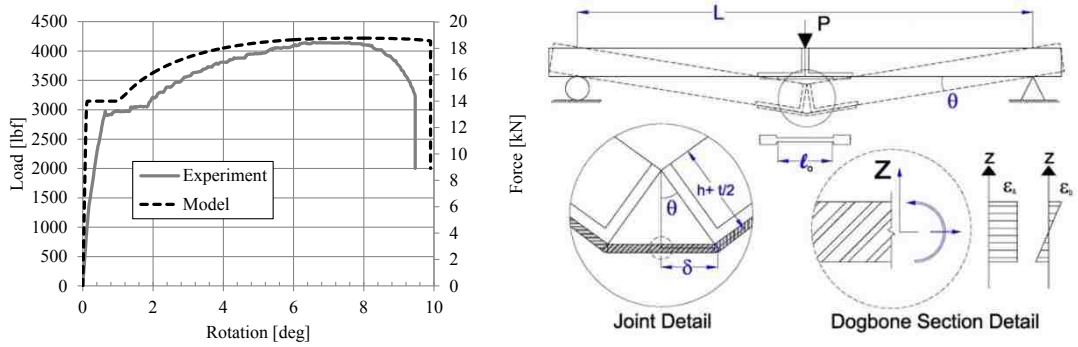

Figure 25: Average dogbone experimental versus analytical results

As shown in Figure 25, the axial deformation of half of the dogbone, δ, can be approximated by Equation 1, where h is the depth of the panel, t is the thickness of the dogbone and θ is the support rotation. Axial strain can then be determined by dividing the total axial dogbone deformation by the original undeformed length, ℓ_o. Bending curvature of the dogbone, φ, can be approximated by calculating a plastic hinge length, ℓ_{pl}, as given in Equation 2. A plastic hinge length of 14.7mm (0.58 in.) was determined by calculating the moment capacity of the section at the end of the yield plateau, M_{ey}, solving for the load applied at which M_{ey} is reached and then finding the point along the neck where yield first occurs. The bending strain distribution in the dogbone can be computed from the product of the curvature and the distance from the neutral axis of the dogbone to each fiber in question, z. The total strain is approximated by decoupling the axial and bending strains

www.manaraa.com

and summing as separate components as given in Equation 3. The stress distribution, σ_t, of each dogbone is then determined by utilizing the constitutive relation between stress and strain for the dogbone member given in Figure 20. The force in each dogbone can be calculated by integrating the stress distribution with Equation 4, where w is the width of the dogbone member. Although the contribution of the additional moment due to bending of the dogbone to the total bending moment is less than 1%, it is accounted for with Equation 5. The total bending moment is then approximated by assuming a moment arm, which decreases as a function of displacement, equal to the summation of the thickness of the panel and half the thickness of the dogbone, as given in Equation 6, where N_{dbone} is the number of dogbones on the panel. Finally, the applied load, P, can be determined through statics as provided in Equation 7. The analytical model is compared to the experimental average of the dogbone panels in Figure 25. The model neglects stretching of the angle anchorage, leading to an overestimation of the initial panel stiffness.

$$\delta(\theta) = \left(h + {}^{t}/_{2}\right)\sin\theta \qquad \text{Equation 1}$$

where δ is the approximate stretch of the dogbone at midspan, h is the depth of the panel, t is the thickness of the dogbone, and θ is the support rotation of the panel

$$\varphi(\theta) = {}^{\theta}/_{l_{p1}} \qquad \text{Equation 2}$$

where φ is the approximate curvature in the dogbone due to bending, and l_{p1} is the calculated plastic hinge length

$$\varepsilon_t(\theta, z) = \frac{2\delta(\theta)}{l_o} + \varphi(\theta)z \qquad \text{Equation 3}$$

where ε_t is the total strain in the dogbone, l_o is the original undeformed length and z is the distance from the neutral axis of the dogbone to each fiber in question

www.manaraa.com

$$F = \int_{-t/2}^{t/2} \sigma_t(\theta, z) dA = w \int_{-t/2}^{t/2} \sigma_t(\theta, z) dz \qquad \text{Equation 4}$$

where F is the total force in the dogbone, σ_t is the total stress in the dogbone, dA is an infinitesimal area of dogbone, and w is the width of the dogbone

$$M = \int_{-t/2}^{t/2} z\sigma_t(\theta, z) dA = w \int_{-t/2}^{t/2} z\sigma_t(\theta, z) dz \qquad \text{Equation 5}$$

where M is the total bending moment in the dogbone

$$M_o = \left[F * \left(h + {}^{t}/_{2}\right) * \cos(\theta) + M\right] * N_{dbone} \qquad \text{Equation 6}$$

where M_o is the bending moment of the panel at midspan and N_{dbone} is the number of dogbones

$$P = \frac{4M_o}{L} \qquad \text{Equation 7}$$

where P is the total applied force at panel midspan, and L is the panel span length

Unbonded Panel Performance

The unbonded panel was examined using numerical and analytical approaches. Numerical models were executed by a general-purpose finite element (FE) analysis package, Abaqus (Dassault 2010). FE models offered insight into the behavior and failure mechanism of the conventionally reinforced panel versus the unbonded panels. In this study, FE models were developed for the control, $20d_b$ unbonded, and $40d_b$ unbonded panels respectively and then validated by comparing the simulation results with experimental data.

Accurately modeling the damage behavior and fracture of reinforced concrete is difficult in FE modeling. In reality, concrete is comprised of a heterogeneous group of material properties. A single material model was selected to represent the concrete out of simplicity and minimize the number of assumptions for unknown properties. The concrete damaged plasticity model was selected to represent the inelastic behavior of the reinforced concrete elements based on the assumption of isotropic damage. This model takes into

www.manaraa.com

consideration the degradation of the elastic stiffness induced by plastic straining both in tension and compression, and provides a plasticity-based continuum damage model for concrete. In damaged plasticity, the two main failure mechanisms are tensile cracking and compressive crushing of the concrete material. Engineering stress-strain curves from Figure 20 were input into the damaged plasticity model for concrete and the plastic material card for the reinforcement. Concrete was modeled with 8-node quadratic brick solid elements (C3D8), while the reinforcement was modeled with 3-node quadratic truss elements (T3D3).

The nodes of the concrete and rebar parts were merged in the bonded region, to represent the physical behavior between the rebar and concrete. To model the physical behavior of the panel in the unbonded region, the concrete and rebar nodes were left unmerged, while stiff axial spring elements were added to the reinforcement in order to constrain the displacement of the rebar in the vertical or out-of-plane direction while allowing translation in the longitudinal direction. The panel was simply supported and a nodal displacement was enforced in the top centerline nodes. The vertical displacements of the nodes at the bottom centerline were monitored. To simulate the experimental loading condition, the displacement along the top line of nodes at the center of the panel was enforced, and the resistance was extracted from the reaction forces.

The results from the FE analyses provide an accurate estimate of the measured response up to a support rotation of 5º, as seen in Figure 26. Model and experimental results begin to diverge past 5º of rotation; however, all output extracted from the model was done within a support rotation of 5º.

www.manaraa.com

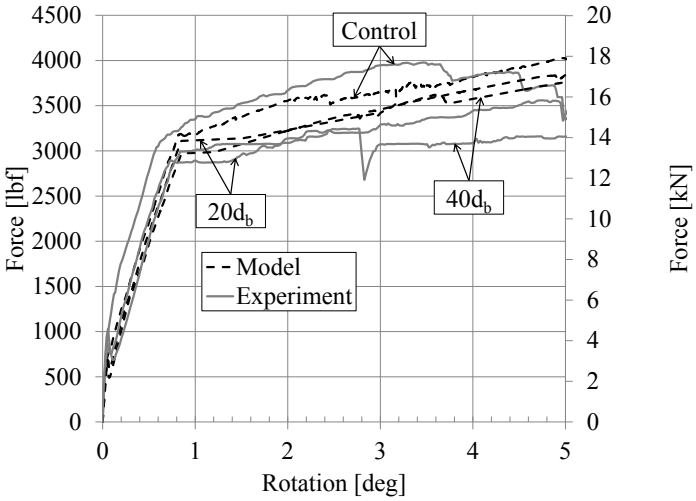

Figure 26: FE versus experimental

The flexural resistance of the panels is formed by the moment couple between the compression force developed in the concrete and the tension force in the rebar. The FE models were used to investigate the difference in the flexural mechanisms of the control and unbonded panels by studying these two components. The strain was used as a parameter to describe the effect of the unbonded reinforcement on the distribution of the stresses and the formation of the flexural mechanism.

The strain in the truss elements was output from the FE models along the length of the panel, as shown in Figure 27. The models agree that the unbonded reinforcement behaves as assumed in Figure 18. The unbonded reinforcement strains over the entire length of the unbonded region, while the bonded panel peaks at a crack location. This results in strain that is lower in the unbonded panels than the control panel at a given displacement.

www.manaraa.com

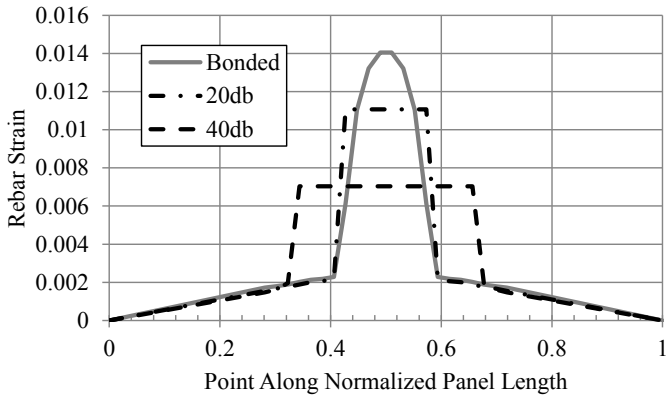

Figure 27: Rebar strain comparison at 19.1 mm (0.75 in.) of panel deflection

The compressive strain in the concrete elements was also output along the length of the panel. As the strain varies along the depth of the panel from the neutral axis to the extreme compressive fiber and along the width with the largest strains generally occurring at the center, an average strain value was plotted along the length of each panel (Figure 28). The figure indicates that the unbonded reinforcement decreases the ultimate strain in the concrete as well. Both unbonded panels have a lower peak strain at midspan than the control panel. Outside of the unbonded region, all panels provide similar strain results.

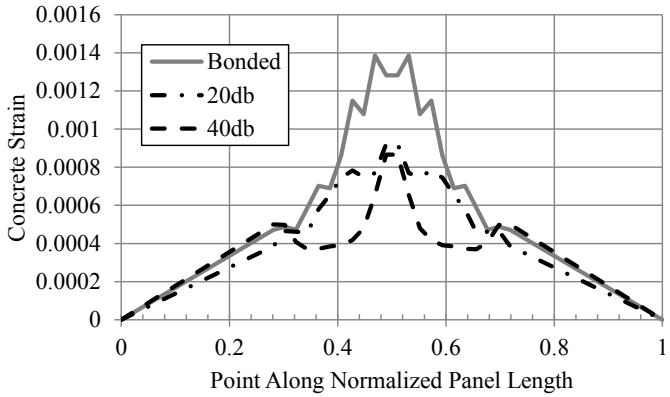

Figure 28: Concrete strain comparison at 19.1 mm (0.75 in.) of panel deflection

The FE models indicate that unbonding the reinforcement leads to smaller peak strains in

www.manaraa.com

the rebar and thus the concrete. As stated before, these two components form the flexural resistance of the panel; therefore, a local failure of one of these two components, fracture of the rebar or crushing of the concrete, controls the global failure of the panel. Thus, distributing the strains over the unbonded region and lowering the peak strain results in a panel that is able to deform further while decreasing the maximum load capacity.

Analytical Modeling of Unbonded Panel

Similar to the dogbone panel, an approach based on assuming a mechanism at center span is utilized to develop an analytical model to predict the response of the unbonded panels. Equation 8 calculates the stretch of the rebar at the opening of a crack at center span where d is the reinforcement depth and R is a reduction factor such that the moment arm is approximately equal to the centroid of the compression zone subtracted from the reinforcement depth. A value of R equal to 0.85 was determined through the fiber analysis of the conventionally bonded panel. Equation 9 approximates the curvature of the reinforcement from bending as the quotient of the support rotation and an assumed plastic hinge length, ℓ_{p2}, equal to two times the bar diameter. Equation 10 calculates the total strain distribution in the reinforcement as the summation of the axial and bending components where ℓ_b is the unbonded length of the panel and z is the distance from the neutral axis of the rebar to each fiber in question. From Figure 20, the stress distribution in the reinforcement can be determined from the calculated strain distribution. Equation 11 and Equation 12 calculate the total force and bending moment in the reinforcement by integrating the stress distribution over the area of the reinforcement. The width of the reinforcement is a function of the reinforcement thickness, $w(z)$, as the rebar has a circular geometry. Equation 13 calculates the total bending moment of the panel, where N_{rebar} is the number of rebars in the panel. The applied force is then determined through statics, as

www.manaraa.com

provided in Equation 14, where L is the span length of the panel. In addition to the mechanism at center span, deformation of the bonded region is accounted for with a fiber analysis, which primarily affects the initial stiffness of the panels.

$$\delta(\theta) = R * d \sin\theta \qquad \text{Equation 8}$$

where δ is the approximate stretch of the rebar at midspan, R is a moment arm reduction factor, d is the reinforcement depth and θ is the support rotation of the panel

$$\varphi(\theta) = {}^{\theta}/_{l_{p2}} \qquad \text{Equation 9}$$

where φ is the approximate curvature in the rebar due to bending, and l_{p2} is a plastic hinge length taken as two times the rebar diameter

$$\varepsilon_t(\theta, z) = \frac{2\delta(\theta)}{l_b} + \varphi(\theta)z \qquad \text{Equation 10}$$

where ε_t is the total strain in the rebar, l_b is the unbonded length of the rebar and z is the distance from the neutral axis of the rebar to each fiber in question

$$F = \int_{-d_b/2}^{d_b/2} \sigma_t(\theta, z)dA = \int_{-d_b/2}^{d_b/2} \sigma_t(\theta, z)w(z)dz \qquad \text{Equation 11}$$

where F is the total force in the reinforcement, d_b is the maximum diameter of the rebar, σ_t is the total stress in the reinforcement, dA is an infinitesimal area of rebar, and w is the width of the reinforcement

$$M = \int_{-d_b/2}^{d_b/2} z\sigma_t(\theta, z)dA = \int_{-d_b/2}^{d_b/2} z\sigma_t(\theta, z)w(z)dz \qquad \text{Equation 12}$$

where M is the total bending moment in the reinforcement

$$M_o = [F * (d * R) * \cos(\theta) + M] * N_{rebar} \qquad \text{Equation 13}$$

where M_o is the bending moment of the panel at midspan and N_{rebar} is the number of rebars

$$P = \frac{4M_o}{L} \qquad \text{Equation 14}$$

where P is the total applied force at panel midspan, and L is the panel span length

www.manaraa.com

The results of the analytical model versus the $20d_b$ and $60d_b$ unbonded panels are provided in Figure 29. Failure of the panel was restricted to rebar fracture in the analytical model. The model adequately captures the failure point of the unbonded section; however, the model unconservatively predicts the ultimate capacity of the panel at shorter unbonded lengths. Further research is necessary to determine the unbonded length at which the compression zone controls the failure mechanism of the panel and to develop a more accurate analytical model.

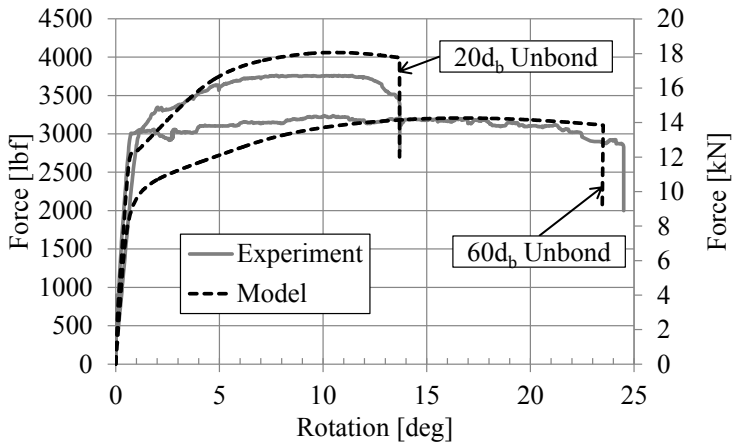

Figure 29: Analytical model versus average experimental results

4.3.6. Flexural Mechanism Conclusions

Developing a predictable flexural mechanism in thin, conventionally reinforced concrete elements is a concern for applications requiring large ultimate displacements, such as a blast design scenario. Two approaches for achieving this design objective were presented. The results of this research are:

- A flexural mechanism with sustained resistance does not occur in thin concrete elements due to crushing of the concrete in the compression zone. The fiber analysis model conducted in this paper confirms that panels which are classified as tension

www.manaraa.com

controlled by ACI 318-11 R10.3.4 may have limited ultimate deformation capacity due to concrete compression failure.

- A predictable hinge can be created by utilizing a specially designed steel mechanism at the center of the panel. Dogbone panels were designed to obtain a support rotation of 10° and a yield force equal to the nominal moment of a conventionally reinforced panel. Analytical methods based on first principles accurately predict the behavior of the dogbone panel.
- Dogbone panels require considerable effort to fabricate, deviating significantly from traditional cast-in-place techniques. Further research on alternative design details may be required for the dogbone method to be applicable in practice.
- Locally unbonding longitudinal reinforcement provides a predictable, ductile flexural mechanism in an emulative manner while maintaining enough development to allow transmission of the necessary bar forces to attain a high panel resistance.
- An analytical model based on a localized flexural mechanism and deformable beams was developed to predict the behavior of unbonded panels.

4.4. Insulated Panel Performance

Flexural mechanisms were developed to improve the response of solid concrete members; however, to improve the thermal resistance of a panel, an insulated panel must be used. In order to assess the performance of an insulated panel to a blast load, it is first necessary to understand the behavior of the insulated panel. Once the behavior is understood, the resistance function of the panel can be obtained and the standard, validated SDOF approach can be utilized to determine the response of an insulated wall panel to a blast

www.manaraa.com

load. The following sections experimentally and numerically discuss the behavior of an insualted wall system.

4.4.1. Introduction to Insulated Wall Panels

Energy consumption and preservation has become a major concern among the threat of climate change and the increasing cost of utilities. While many sectors in the U.S. contribute to the nation's energy consumption, building operations alone account for 41% (Preservation Green Lab 2011). The construction industry responded to the energy crisis by forming a U.S. Green Building Council (USGBC) to promote sustainability in the building and construction industry (Fedrizzi 2014). Since the establishment of the concept of "Leadership in Energy and Environmental Design" (LEED) certified buildings by the USGBC in 2000, the number of LEED projects has grown significantly. From 2011 to 2012, the number of LEED certified U.S. federal buildings grew by more than 50% (Katz 2012), while up to 48% of all new nonresidential construction is estimated to be green by 2015 (Research and Analytics 2010). One requirement for a building to become LEED certified is to minimize energy consumption through the use of efficient heating, ventilation, air conditioning, and other systems (USGBC 2005). For these systems to be effective, however, the facility must have a thermally resistant building envelope.

In 1954 Collins (1954) illustrated that energy saving benefits could be achieved through a composite cladding system comprised of concrete and insulating foam. Development of insulated wall panels continued with research on the effect of insulation properties on the flexural stiffness of panels by Pfiefer and Hanson (1964). With the recent emphasis on sustainable construction, researchers and developers have been refining the insulated panel to improve thermal resistance without compromising the structural integrity of the wall panel (Bush and Stine 1994). One method to improve the thermal behavior of the wall

www.manaraa.com

involves replacing highly conductive material, such as steel, with thermally efficient material. Thermally resistive shear ties comprised of carbon fiber-reinforced polymers (CFRP) glass fiber-reinforced polymers (GFRP) have been shown to provide the required flexural resistance (Frankl, Lucier, Hassan and Rizkalla 2011 and Woltman Tomlinson, and Fam 2013).

Multi-wythe insulated concrete panels are a popular form of exterior building cladding used by the precast concrete industry for residential and commercial buildings. Insulated wall panels have been produced in the United States for more than 50 years (PCI 2011). These wall systems consist of an exterior concrete wythe, an interior insulation layer, and an interior concrete wythe. These systems can be configured with the interior and exterior wythe connected via shear ties to provide composite action to out-of-plane loads. It can also be configured as non-composite with an interior structural wythe, an exterior architectural wythe, and nominal number of shear ties. Insulated panel systems lend themselves to precast construction allowing for expedited onsite erection of the building envelope. The insulation layer typically consists of expanded polystyrene (EPS), extruded polystyrene (XPS), or polyisocyanurate (Polyiso), and the type and thickness of the insulation materials depends on the energy efficiency requirement for the building envelope. The most common use of insulated panels is for exterior walls, but they can also be adopted as internal partition walls, especially when thermal transmission within the facility is restricted.

This part of the research experimentally and analytically examines the performance of prestressed and non-prestressed insulated non-loadbearing panels under uniform out-of-plane loading. Conventional insulated wall panel design in accordance with the precast/prestressed concrete institute (PCI 2011) is reviewed and assessed. The effect of

www.manaraa.com

reinforcement type is evaluated for both solid and insulated wall panels. The contribution of the insulation type to the panel performance is examined. The influence of the shear tie mechanical and geometric properties on the behavior of the panel is investigated. Finally, a mechanics based analytical approach for estimating the deflection of an insulated panel subject to flexure is provided.

4.4.2. Current Design Methodology

Insulated precast concrete wall panels, commonly referred to as sandwich panels, consist of a layer of insulation sandwiched between two layers, or wythes, of concrete. Due to the insulating layer, the panel provides a high thermal resistance without sacrificing an aesthetic design, economic fabrication and rapid installation inherit in precast products. In order to design an insulated concrete wall panel, the function of the panel must first be considered with respect to various life cycle requirements (handling, construction, required service demands, energy goals, architectural requirements, etc.). Strength and deflection limits are then determined in accordance with the IBC (ICC 2006), ACI 318-11 (ACI 2011), or other local building codes (flexure demands, minimum steel requirements, fire mandates, etc.). Up to this point, the process of designing an insulated wall panel has been no different than a traditional solid panel. A decision must now be made as to whether the sandwich panel is to act compositely, non-compositely (no designed shear transfer between the exterior and interior wythes), or somewhere between the two. All of this information dictates the necessary wythe and insulation thickness, material strengths, amount, and type and layout of reinforcement. Once the nominal strength of the panel is determined, the demands on the shear ties can be determined.

Shear ties are used to support the forces generated during fabrication, transportation, erection, and service life. Tie systems provide both shear and tension strength to the

www.manaraa.com

interface between the interior and exterior wythe. In most cases compression is assumed to be transmitted through the insulation. The forces transferred between wythes, and thus ties, vary based on the applied load on the wall as illustrated in Figure 30. The combinations of shear and tension on the tie vary over the life of the structure.

While the physical connection is necessary to create composite action allowing for a thinner, more structurally efficient panel, the connection allows heat to transfer directly between the concrete wythes in a phenomenon called "thermal bridging" decreasing the thermal efficiency of the panel (Trasborg and Naito 2013). By utilizing shear ties with a thermally resistive material, the effects of thermal bridging can be diminished or removed entirely. Many proprietary shear tie systems are available and can be selected based on strength, stiffness, thermal resistance, and cost.

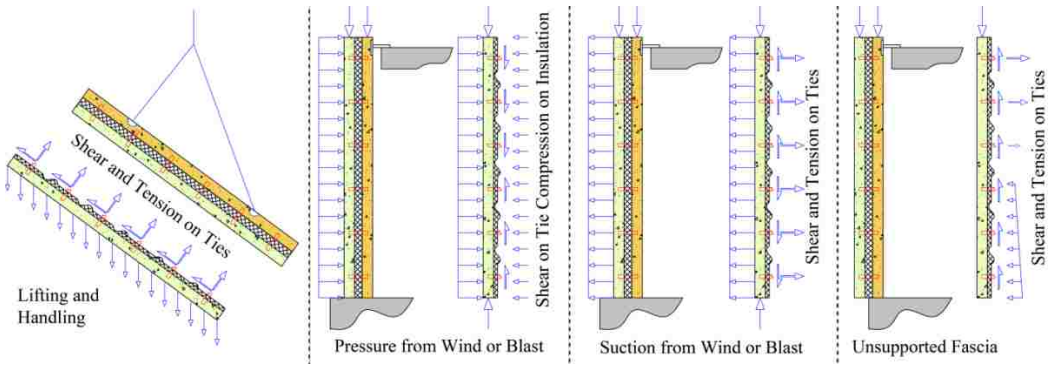

Figure 30: Forces on shear ties under various loading conditions

In the United States the use of shear ties are at the discretion of the precast producer. To provide more acceptance in various municipalities acceptance criteria have been developed for shear ties by the International Code Council (ICC). The ICC develops model codes and standards to ensure safe, sustainable, affordable and resilient structures. Currently, 50 states and the District of Columbia have adopted codes from the ICC at the state or jurisdictional level (ICC 2014). ICC AC320 (ICC 2006) and ICC AC422 (ICC 2010)

www.manaraa.com

dictate how to determine the strength, allowable service load, spacing, conditions of acceptance, quality control, etc. for discrete and continuous ties respectively. Additionally, AC422 specifies how to handle ties subjected to combined shear and tension forces. These acceptance criteria help to ensure that the various shear ties perform adequately for building applications.

Shear ties may be placed at discrete locations or distributed along the length of the panel. Shear ties can be used to allow the interior and exterior wythe to work in tandem to resist externally applied flexural loads. For insulated panels with shear connectors, the flexural behavior can be classified as non-composite, composite, or partially-composite. These scenarios are illustrated in Figure 31. Full composite behavior is characterized as flexural response based on a linear strain profile over the panel section and negligible relative slip between the exterior and interior wythes (Figure 31B). Non-composite behavior exists when the interior and exterior wythes act independently to resist applied loads. This can be compared to loading two stacked slabs with a frictionless interface between them. Due to compatibility, the stacked slabs must have the same curvature, rotation, and displacement along the length. This results in measurable relative slip between the two wythes (Figure 31C). Between the two extremes is the case of partially composite behavior. Partially-composite behavior is characterized by a level of shear transfer between the interior and exterior wythes and resistance to relative slip (Figure 31D). With a high degree of shear transfer the panel will tend toward that of a composite section and with a low degree of shear transfer the panel will tend toward the non-composite section.

www.manaraa.com

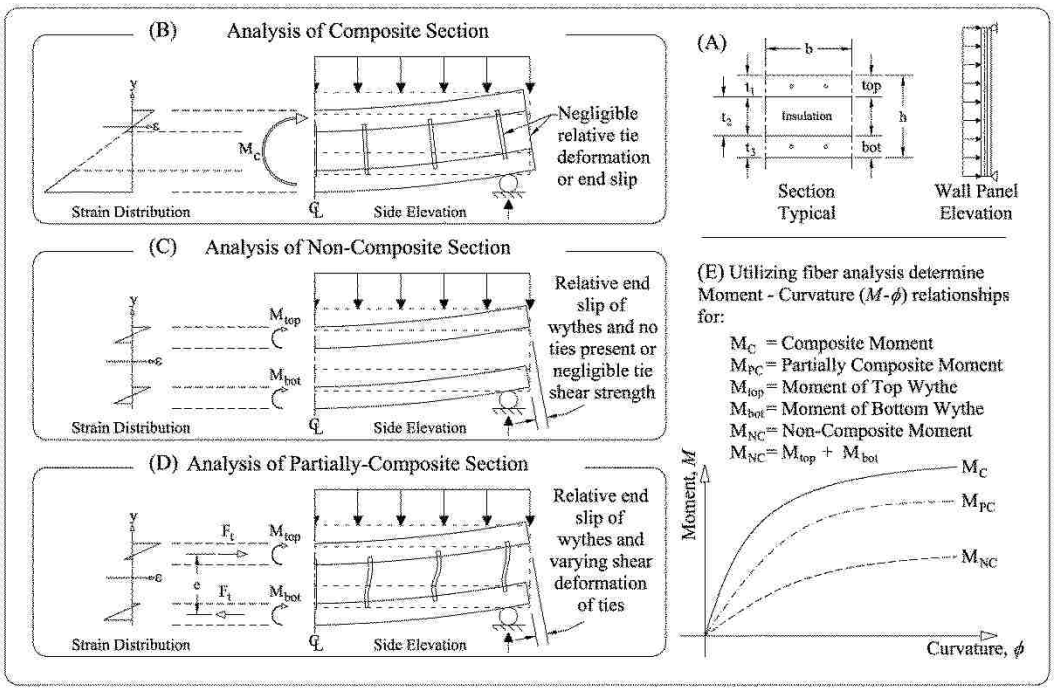

Figure 31: Flexural behavior of insulated concrete wall panels

The conventional approach for designing a composite panel is based on the horizontal shear generated from the balance of flexural compression and tension forces in the section (PCI 2011). For design against positive flexure, the tensile force from the reinforcement in the interior wythe, T, and a conservative estimate of the concrete compressive force in the exterior wythe, C, are calculated by Equation 15 and Equation 16 respectively. The interface shear demand on half of the panel, V_h, is then taken as the minimum of the worse-case tension or compression force on the section, Equation 17.

$$T = A_s \cdot f_y + A_{ps} \cdot f_{ps} \qquad \text{Equation 15}$$

Where A_s is the area of deformed bar, A_{ps} is the area of prestressing steel, f_y is the yield stress of the deformed bar, and f_{ps} is the stress in the prestressing steel stress at nominal strength.

$$C = 0.85 \cdot f'_c \cdot A_c \qquad \text{Equation 16}$$

Where f'_c is the compressive strength of the concrete and A_c is conservatively taken as the

www.manaraa.com

total area of the compression wythe.

$$V_h = \min(T, C) \qquad \text{Equation 17}$$

For a panel to be considered fully composite by the PCI method, the tie capacity multiplied by a reduction factor must be greater than V_h.

This design approach relies on the assumption that all ties in the section achieve their specified strength at the same time, when the panel reaches its nominal flexural strength. Variation in tie deformation along the span of the panel due to compatibility of deformations between the interior and exterior wythe are not considered. The approach also does not account for variations in stiffness and ductility from one tie system to the next. For example, a stiff tie system that achieves strength at 1 mm of shear deformation would be considered equivalent to a flexible tie system that does not achieve strength until 20 mm. Consequently, the actual level of composite action achieved in the approach may not be effectively met.

Partially composite behavior is achieved with the PCI approach by using less ties than that needed for the design interface shear demand. While this approach may be adequate for conventional demands such as erection and wind where the response of the panel remains elastic, under extreme loading such as blasts the nonlinearity of the panel and interface ties should be considered. If a panel has the potential to be loaded to its ultimate flexural response during service, the load-deformation response of the insulated wall panel must be predictable. The load-deflection response of composite and non-composite reinforced concrete wall panels can be readily determined using well-established approaches (Keba and Mahin 1984, DoD 2008). The response of a partially composite wall panel however is not discernable since the level of shear transfer cannot be accurately determined using the PCI design approach. An alternate approach was developed by Salmon and Einea (1995)

www.manaraa.com

for determination of partially composite panel deflections. The method however is limited to relatively small thermal bowing deflections and cannot be used to examine the response at flexural strength.

An experimental study is conducted to examine the performance of insulated wall panels and their sensitivity to tie strength and stiffness. The behavior observed is used to develop and validate an analytical approach for determining the load-deflection response of partially composite panels.

4.4.3. Experimental Program

A total of 19 panel configurations were examined through experimental testing. Due to repetition of the experiments a total of 51 panel tests are included in the study. The test matrix is provided in Table 9. Panels listed with the subscript "$^{+}$" in Table 9 are taken directly from (Naito et al. 2014a), with more detailed information available in Naito et al. (2011). The remaining panel configurations represent new experimental data. The first letter of the panel ID signifies the reinforcement type with "P" for prestressing steel, "R" for non-prestressed steel, and "B" representing the presence of both. The second letter of the panel ID signifies the total panel thickness with "t" representing 203.2 mm and "T" representing 228.6 mm. The third letter represents the foam type with "E" representing expanded polystyrene (EPS), "X" representing extruded polystyrene (XPS), and "P" representing polyisocyanurate (polyiso). The fourth and final letter represents the shear tie type with "L" representing C-Clip, "G" representing C-Grid®, "C" representing Thermomass® CC, "X" representing Thermomass® X-Series, "M" representing Thermomass® MC, and "N" representing #10 NU-Tie. Panel IDs "Pt" and "Rt" are for the prestressed and non-prestressed solid panels respectively. Note that there are two PtEG panels; however, $PtEG_2$ has an extra 914mm of C-Grid® at each end of the panel.

www.manaraa.com

Table 9: Complete test matrix						
Panel ID	**Reinforcement Per Wythe**	**Panel Width *[mm]***	**Foam Thickness *[mm]***	**Foam Type**	**Tie Type**	**# of Samples**
PtEL^{+}	2-9.53mm strand	813	50.8	EPS	Stainless C-Clip	3
PtEG^{+}	2-9.53 mm strand	813	50.8	EPS	C-Grid®	3
RtEG^{+}	2-#16 bar	813	50.8	EPS	C-Grid®	3
BtEG^{+}	2-9.53 mm strand 2-#16 bar	813	50.8	EPS	C-Grid®	3
PTXL^{+}	2-9.53 mm strand	813	76.2	XPS	Carbon C-Clip	3
PTXC^{+}	2-9.53 mm strand	813	76.2	XPS	CC	3
PTXG^{+}	2-9.53 mm strand	813	76.2	XPS	C-Grid®	3
RTXC^{+}	2-#16 bar	813	76.2	XPS	CC	3
PTPC^{+}	2-9.53 mm strand	813	76.2	Polyiso	CC	2
PTPG^{+}	2-9.53 mm strand	813	76.2	Polyiso	C-Grid®	3
$PtEG_2$	2-9.53 mm strand	813	50.8	EPS	C-Grid®	3
RtXN	6-#10 GFRP Bar	813	50.8	XPS	#10 NU	3
PtXN	2-9.53 mm strand	813	50.8	XPS	#10 NU	3
RtXX	2-#16 bar	813	50.8	XPS	X & CC	3
PtXX	2-9.53 mm strand	813	50.8	XPS	X & CC	3
RtXC	2-#10 bar	305	50.8	XPS	CC	1
RtXM	2-#10 bar	305	50.8	XPS	MC	1
Rt	2-#16 bar	813	Solid	None	None	3
Pt	2-9.53 mm strand	813	Solid	None	None	3

Figure 32 provides a quarter-symmetry of the different cross-sections tested. Panels were either 305mm or 813mm wide with all bars placed in approximately the mid-depth of each wythe. Two 203.2 mm thick solid panels, Rt and Pt, with reinforcement at the same location as the 203.2 mm thick insulated panels were tested as a control group.

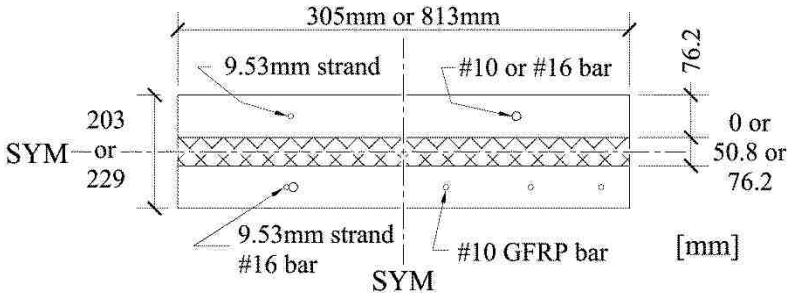

Figure 32: Quarter symmetry of panel cross sections

All panels measured 3.66 m in length and were simply supported with a clear span of 3.05

www.manaraa.com

m. Seven different distributed or discrete shear connector systems were tested as shown in Figure 33. Placement of the ties varied based on the expected horizontal shear demand and the tie strength. The expected shear capacity of each tie system was either determined from past tests conducted by Naito et al. (2012) or through manufacturer published design strengths.

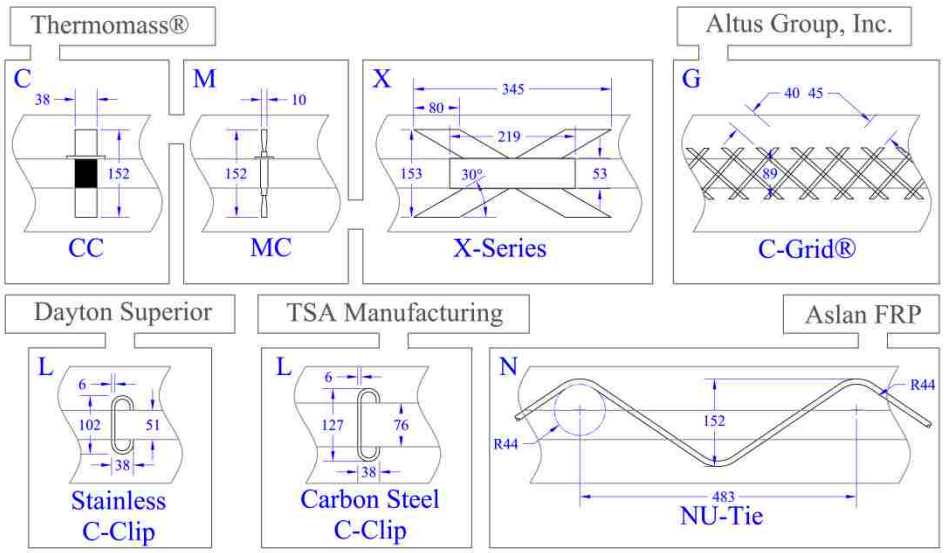

Figure 33: Tie systems

Naito et al. (2012) tested Thermomass® CC and MC ties, Dayton Superior stainless steel C-Clip, TSA Manufacturing carbon steel C-Clip and Altus Group C-Grid® with 50.8 mm of insulation to failure. The simplified shear load-displacement of each tie is shown in Figure 34 where discrete and distributed tie force values are shown on the primary and secondary ordinates respectively. For shear ties not tested by Naito et al., manufacturing data is used (Thermomass® 2012A) (Thermomass® 2012B). All tie strengths are tabulated in Figure 34.

www.manaraa.com

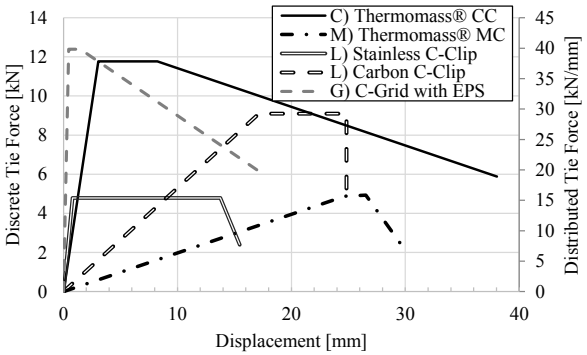

ID	Tie Name	Strength
C	Thermomass® CC	11.8 kN
M	Thermomass® MC	4.92 kN
X	Thermomass® X	54.3 kN
G	C-Grid with EPS	39.8 kN/m
L	Carbon C-Clip	9.10 kN
L	Stainless C-Clip	4.79 kN
N	NU-Tie	55.2 kN

Figure 34: Tie load-displacement and tabulated tie strengths

Tie placement is shown with each corresponding panel in quarter symmetry in Figure 35. Ties were laid out following manufacturer recommendations. Note panels RtXC and RtXM were not included in the drawing due to the smaller cross section width than the other panels; however, panel RtXC had a single line of Thermomass® CC connectors spaced at 406mm on center starting 203 mm from the panel end while panel RtXM contained only two Thermomass® MC connectors each located 914 mm out from center span.

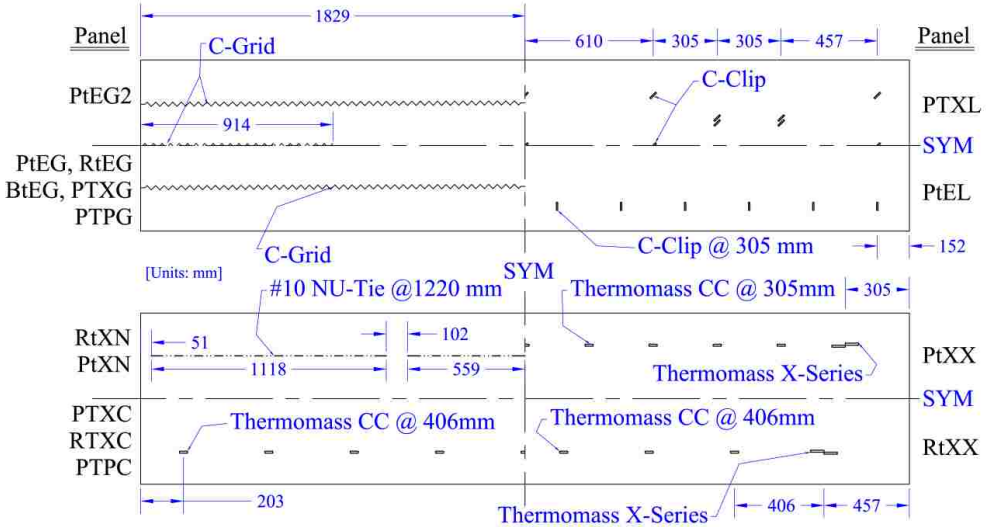

Figure 35: Quarter symmetry of panel tie layouts

4.4.4. Experimental Test

All panels were subjected to uniform loading either simulated with a loading tree (Naito et

www.manaraa.com

al. 2014a) or supplied via water bladder as shown in Figure 36. The loading tree consisted of a steel beam connected to a single actuator at the center of the tree. Bar sections were pin connected to each end of the steel beam sections. This procedure was repeated until reaching the loading points which consisted of 16 pipes evenly distributed along the span of the panel. The balanced rockers that make up the loading tree result in equal point loads along the span and provide a uniform load. The ends of the panel were restrained from vertical translation while the applied load was determined by monitoring the load of the actuator.

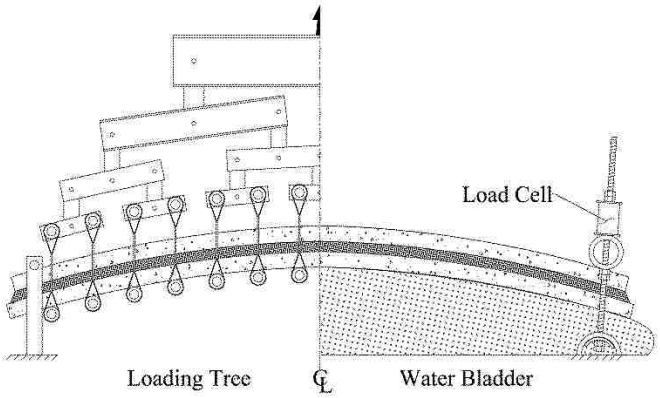

Figure 36: Uniform loading setups

The water bladder setup consisted of a 4 m long steel table with XX strong pipes at each end to provide the simple supports. Each pipe section was restrained by two threaded rods which were pin connected to the steel table to allow the pipe sections to rotate freely. As the water bladder filled, the panel lifted until the ends made contact with the pipe sections. The water bladder was capable of applying 103 kPa of pressure with a maximum displacement of 760 mm. Water was chosen as opposed to air due to its incompressibility, allowing the unloading branch of the load-displacement graph of each panel to be captured. A through-hole load cell was placed between the pipe section and the top of each threaded rod. The total applied load was determined by summing all four load cells.

www.manaraa.com

Panel displacement was determined by attaching a potentiometer to each side of the panel at mid-span as shown in Figure 37. Potentiometer results from each side were averaged to approximate the overall panel displacement. Linear variable differential transformers and string potentiometers were attached to the end of each insulated panel as shown in Figure 37 to record the relative displacement between the end of each wythe, for the load tree and bladder setups respectively. Panel displacement is normalized relative to the span by converting it to an effective support rotation, θ, which is approximated by Equation 18.

Figure 37: Center-span displacement and end-slip instrumentation

$$\theta = \tan^{-1}\left(\frac{2\Delta}{L}\right) \qquad \text{Equation 18}$$

Where Δ is the average center panel displacement and L is the clear span length equal to 3.05 m

4.4.5. Experimental Results

All panels were tested under monotonically increasing displacement until the reinforcement fractured, the testing apparatus reached maximum stroke, or the ends of the panel began to bear against the loading table. Figure 38 provides typical elevation views of different panel mechanisms and typical end-slip at the conclusion of each test.

www.manaraa.com

Prestressed insulated panel

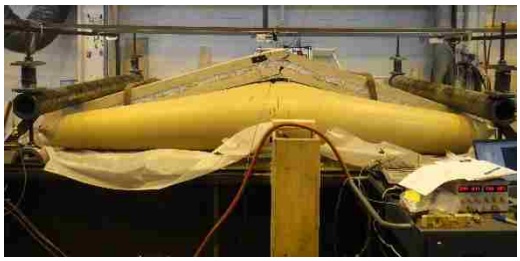

Non-prestressed insulated panel

Prestressed solid panel

Non-prestressed solid panel

GFRP insulated panel

Figure 38: Elevation views of typical panel mechanisms

Expected composite and non-composite moment capacities for each panel were determined based on the material properties and either the design dimensions or as built dimensions. The percent composite level obtained, $\%Comp_{act}$, was computed using Equation 19. Conversely, the percent composite level the panel was designed to reach, $\%Comp_{des}$, was determined with Equation 20.

$$\%Comp_{act} = \frac{M_{max} - M_{NC}}{M_C - M_{NC}} \qquad \text{Equation 19}$$

Where M_{max} is the maximum measured moment, M_{NC} is the design non-composite moment capacity, and M_C is the design composite moment capacity. If M_{max} is less than M_{NC} then $\%Comp_{act}$ is taken as zero.

$$\%Comp_{des} = \frac{V_{tie}}{V_h} \qquad \text{Equation 20}$$

www.manaraa.com

Where V_{tie} is the tie system capacity and V_h is the horizontal shear demand from Equation 17. V_{tie} is calculated by multiplying the number of ties by the tie capacity.

Table 10 summarizes the average results for each panel type. Panel rotation and end-slip are provided at the maximum panel moment. Concrete strengths, f'_c, are provided for each panel group based on design strengths or cylinder tests when available. Note that panel RtXM was designed to act non-compositely. Concrete strength is provided in MPa, rotations in degrees, moment in kN-m, and shear force in kN.

Table 10: Average panel results

ID	f'_c	θ @ M_{max}	M_{max}	Slip @ M_{max}	M_C	M_{NC}	$Comp_{act}$	V_h	V_{tie}	$Comp_{des}$
PtEL*	56.7	1.77	29.3	4.45	33.5	14.6	77.5%	215	115	53.4%
PtEG*	57.9	1.80	33.3	7.39	33.5	14.6	99.2%	215	146	67.7%
RtEG*	58.0	3.93	34.6	1.25	36.0	12.4	94.1%	165	146	88.1%
BtEG*	59.9	4.39	37.8	18.0	36.0	12.4	108.4%	381	146	38.3%
PTXL*	60.8	5.93	30.3	23.5	39.3	14.6	63.3%	215	N.A.	-
PTXC*	60.6	4.90	31.6	15.3	39.3	14.6	68.6%	215	135	62.5%
PTXG*	59.8	2.75	28.2	11.5	39.3	14.6	54.8%	215	-	-
RTXC*	61.1	5.91	30.3	21.3	41.6	12.4	62.2%	165	135	81.3%
PTPC*	60.9	4.59	27.1	17.2	39.3	14.6	50.1%	215	135	62.5%
PTPG*	59.4	1.99	36.5	6.60	39.3	14.6	88.6%	215	-	-
$PtEG_2$	48.3	1.25	39.9	0.43	37.5	14.9	110.4%	215	169	78.3%
RtXN	34.5	9.53	25.7	54.2	36.2	12.8	55.3%	445	165	37.2%
PtXN	34.5	1.33	34.7	2.54	37.5	14.9	87.6%	215	165	76.9%
RtXX	41.4	4.35	36.0	15.6	37.6	11.8	93.8%	165	179	108.3%
PtXX	41.4	4.80	37.0	11.9	37.5	14.9	97.7%	215	214	99.6%
RtXC	28.2	5.40	9.2	17.6	12.2	4.0	63.2%	59	53	90.2%
RtXM	28.2	3.61	3.9	16.2	12.2	4.0	0%	59	5	8.4%
Rt	48.3	7.90	44.9	0	37.6	-	-	-	-	-
Pt	48.3	2.38	50.0	0	37.5	-	-	-	-	-

*Calculated nominal capacities are based on measured as-built reinforcement depths

The representative moment-rotation and slip-rotation for each panel type were calculated by averaging the measured moment and slip at each measured support rotation. This

www.manaraa.com

approach is illustrated in Figure 39 for the three test results of panel RtXX. The moment and slip values are located on the primary and secondary ordinates respectively. The average curve terminates at the rotation corresponding to the point when all tests but one is complete due to failure or termination of the experiment. Figure 40 provides the average moment-rotations and slip-rotations for all the panels. Solid panels, Pt and Rt, are plotted against similar insulated panels in Figure 40a and Figure 40b respectively. Figure 40c and Figure 40d plot 229 mm thick panels of various shear tie type. Figure 40e plots three types of C-Grid® panels and finally Figure 40f plots 305 mm wide panels.

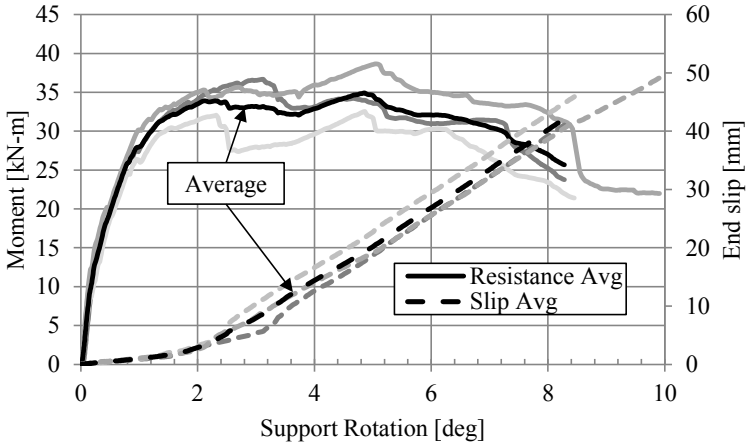

Figure 39: Curve averaging procedure example

www.manaraa.com

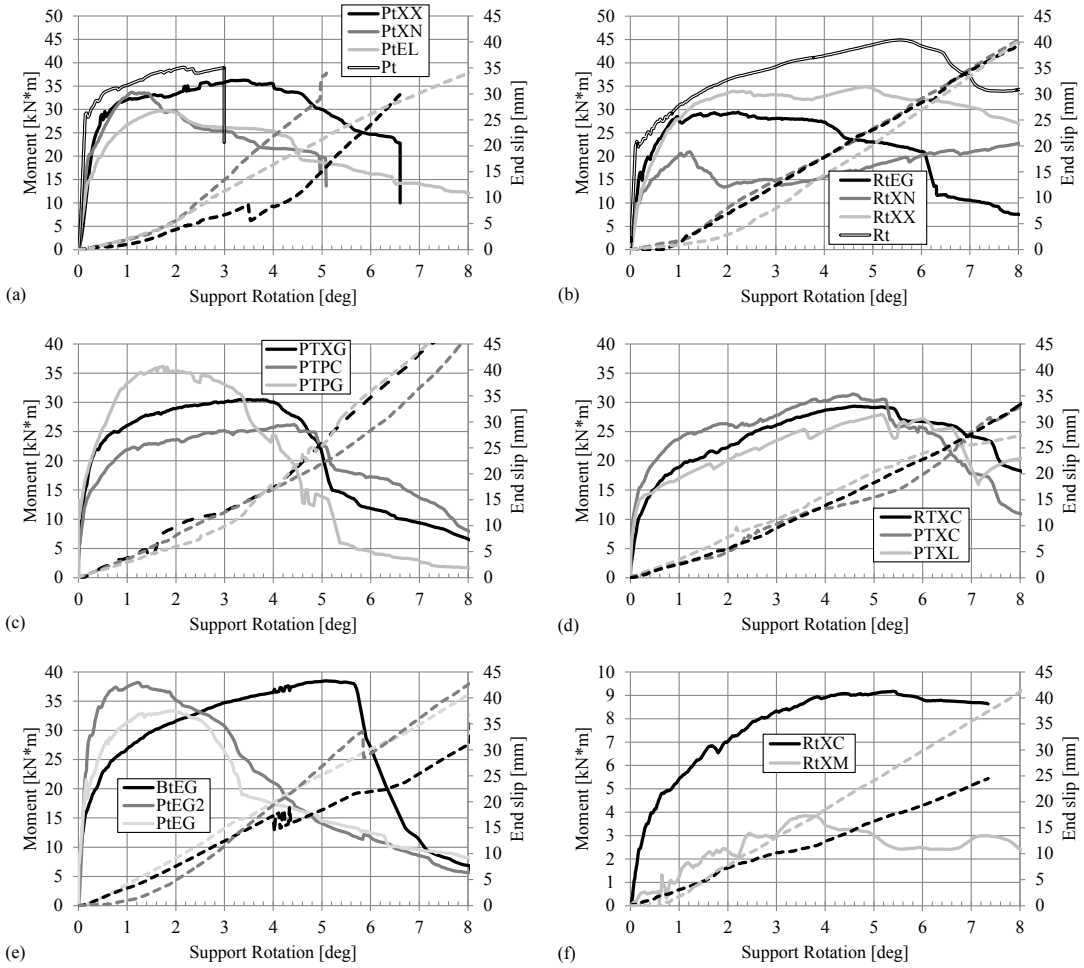

Figure 40: Average moment-rotation and slip-rotation for each panel

4.4.6. Discussion of Results

The majority of insulated panels examined exhibit a composite strength greater or comparable to what they were designed for. This is illustrated in a comparison of the $\%Comp_{act}$ and $\%Comp_{des}$ in Table 10. Only two of the panels achieved a measured strength greater than the estimated composite strength using the PCI strength based approach. As depicted in Figure 40, all insulated panels exhibit significant end-slip as lateral load is applied. As previously discussed, based on the principles of mechanics, for a panel to act composite under flexure a linear strain profile must exist. This requires negligible relative

www.manaraa.com

slip between the wythes. The fact that a panel can achieve a fully composite strength while exhibiting a substantial slip between the wythes is indicative that the assumption of composite behavior is not valid. This is further supported by the observation that the final end slips are on the same order of magnitude for all systems tested irrespective of tie type. Nevertheless, the global moment – rotation response of insulated panels are shown to be influenced by the insulation and tie type and distribution of ties.

Effect of Insulation

Panels with Polyiso and XPS insulation are compared to assess the effect of the foam on the panel behavior. Figure 41 presents the XPS insulation versus Polyiso insulation for panels with the C-Grid® shear tie system (a) and panels with the Thermomass® CC shear tie system (b). The use of Polyiso increased the strength of the C-Grid® panel over that of the XPS. It is noted that the Polysio used had a rough absorbent surface compared to the XPS insulation which is smooth and sealed. The additional roughness provided additional horizontal shear strength against flexural demands. The Thermomass® panels exhibited the opposite behavior. The use of Polyiso resulted in a decrease in strength over the XPS panel. The reason for this decrease is due to the fact that two 38 mm thick Polyiso sheets were used to make up the 76 mm foam thickness in the panel. This created a slip plane in the insulation thus reducing the shear strength. Based on these results the use of rough absorbent insulation foam can be used to increase the flexural strength of a panel. The use of multiple layers of foam or XPS foam will reduce these effects but will typically allow more deformation prior to failure.

www.manaraa.com

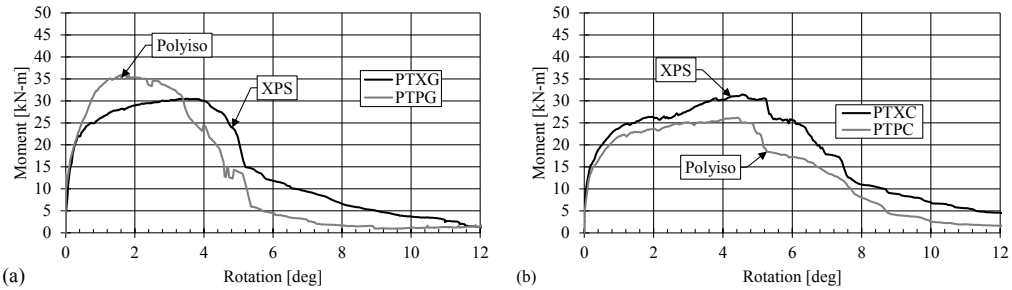

Figure 41: Insulation type comparison: (a) C-Grid® panels, (b) Thermomass ® panels

Effect of Tie Type and Distribution

Comparisons of the performance of each tie system are made for panels with the same geometry and flexural reinforcement. Where possible, comparisons are made to the solid panels with the same reinforcement. The tie systems are compared in four different categories: 1) Stiffness, 2) Rotation at maximum moment, 3) Maximum moment, and 4) Percentage of composite action obtained compared to design. No comparisons were made for panels with distributed shear tie systems as stiffness data was not available for the tie systems.

Four different discrete shear tie systems were tested for the prestressed panels: 1) Panel PtEL –Dayton C-Clips, 2) Panel PTXL – TSA C-Clips, 3) Panel PTXC - Thermomass® CC, and 4) Panel PtXX - Thermomass® CC and X-Series. The normalized post cracking stiffness and amount of end-slip of each system is shown in Figure 42 (a) and (b), respectively. The post cracking stiffness was calculated by the slope between 50% and 80% of the normalized maximum moment. Post cracking stiffness of panel PtEL, PTXL, PTXC, and PtXX was 0.631/deg, 0.119/deg, 0.226/deg and 0.799/deg, respectively. As shown in Figure 42b, panel PtXX had the smallest end-slip, followed by panel PTXC, PtEL, and PtXX. From the data, it was observed that smaller amounts of end-slip corresponded to stiffer panels. Additionally, PtXX contained the stiffest ties with an effective stiffness at 13.4kN/m, followed by PtEL (6.06 kN/m), PTXC (3.86 kN/m), and PTXL (0.53 kN/m).

www.manaraa.com

The panel stiffness was observed to correlate directly to tie stiffness, with stiffer ties leading to a stiffer panel.

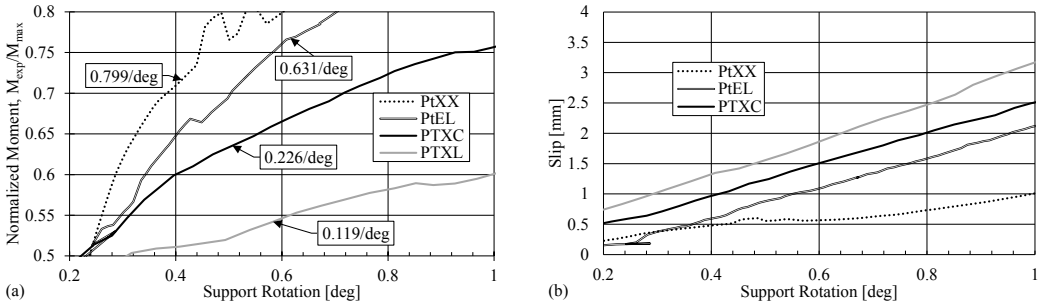

Figure 42: Prestressed panels with discrete ties (a) Post cracking stiffness, (b) End-slip

Support rotations at maximum moment were calculated for each of the four panel groups and found to be 5.9°, 4.9°, 4.8°, and 1.8° for PTXL, PTXC, PtXX and PtEL, respectively. Similarly, end-slips at maximum moment were calculated for each of the four panel groups and found to be 23.5 mm, 15.3 mm, 11.9 mm, and 4.45 mm for PTXL, PTXC, PtXX, and PtEL respectively. Thus, larger support rotations correlate to larger panel support rotations at maximum moment.

The maximum moment for each of the four panel groups was found to be 37.0 kN-m, 31.6 kN-m, 30.3 kN-m, and 29.3 kN-m for PtXX, PTXC, PTXL, and PtEL respectively. Additionally, shear tie strength for each of the four panel groups was found to be 56 kN, 12 kN, 9.1 kN, and 4.8 kN for PtXX, PTXC, PTXL, and PtEL respectively. Increased shear tie strength correlates with increased flexural capacity.

Likewise, comparisons were made between the non-prestressed panels. Two different discrete shear tie systems were compared for the non-prestressed insulated panels: 1) Panel RTXC with Thermomass® CC, and 2) Panel RtXX with Thermomass® CC and X-Series ties. Similarly to the prestressed panels, stiffer shear ties correlate with an increased initial

www.manaraa.com

panel stiffness, larger end-slip at maximum moment correlates to larger support rotation at maximum moment, and a stronger shear tie systems correlates to increased flexural strength.

Effect of Longitudinal Reinforcement Type

The effect of reinforcement type on the flexural response of the panels was examined. Panels were designed as both prestressed and non-prestressed with comparable flexural strength. A fiber analysis (Kaba and Mahin 1984) was conducted to assess the performance of the solid prestressed and non-prestressed panels (Trasborg et al. 2014b). The concrete behavior was approximated by Popovics' model (Popovics 1973) and the reinforcement was simplified to a multi-linear stress-strain relationship as shown in Figure 43a. The material properties of the prestressing strand were taken from mill certifications while the properties of the deformed bar were approximated from tensile tests conducted in accordance with ASTM A370 (2012). Failure of the analytical model was limited to either crushing of the concrete or fracture of the longitudinal reinforcement. Figure 43b compares the estimated response to the average measured response of the solid panels.

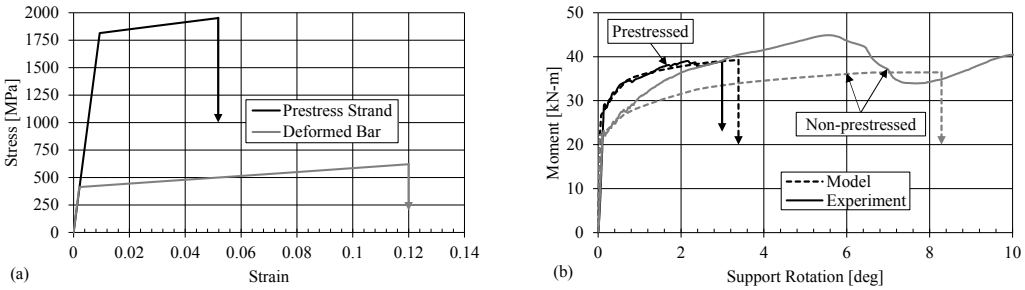

Figure 43: Solid analytical model (a) Material constitutive, (b) Model-experiment comparison

As shown in Figure 43, the prestressed panel fails prior to the non-prestressed panel. Failure in both models, just as with the experimental tests, occurs once the reinforcing

www.manaraa.com

strand and bar fracture. From the analytical model, it was determined that the deformation capacity of the prestressed panel was limited by the strain capacity of the reinforcing strand. Unlike the prestressed panel, the non-prestressed panel is reinforced with deformed bar with a strain capacity over two times greater allowing the panel to reach over twice the rotation before bar fracture.

Longitudinal reinforcement type is also shown to influence the response of the insulated panels tested. Insulated panels having the same shear tie system, insulation type, and insulation thickness are compared in Figure 44. The use of prestressing in the insulated panels reduced the ductility in the system from that of non-prestressed reinforcement when comparing the response of highly composite panels such as the C-Grid® (Figure 44a) and Thermomass® X-Series (Figure 44b) panels which achieved 92 to 108% of their estimated composite flexural strength. The improvement in ductility, however is diminished when panels have lower levels of composite action as illustrated in the Thermomass® CC panels (Figure 44c), PTXC and RTXC which achieved only 62 to 69% composite action.

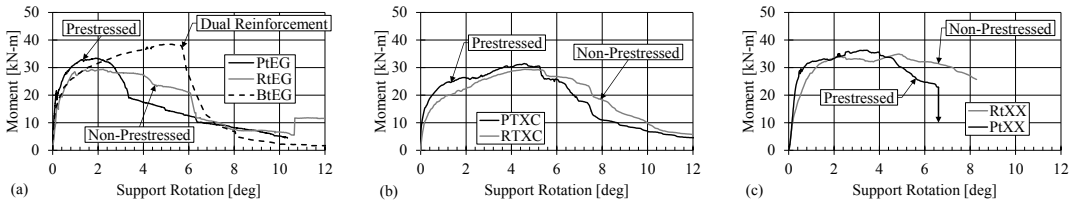

Figure 44: Reinforcement comparison: (a) C-Grid®, (b) Thermomass® CC, (c) Thermomass® X-Series

The experimental results indicate that all of the insulated panels examined exhibit measurable relative slip between the interior and exterior wythes indicative of partial or non-composite action. Furthermore, the flexural response of the insulated wall panels are correlated to the mechanical behavior of the shear tie system, including the stiffness and

www.manaraa.com

strength of the shear tie. To better represent these conditions an analytical model is proposed to predict the response of an insulated panel utilizing the load-deflection characteristic of the shear connector and accounting for the shear tie location along the panel.

4.4.7. Analytical Model

The proposed analytical method presents a deformation based approach for designing shear tie systems accounting for the effectiveness of each shear tie based on the tie properties and location within the panel. The analytical model utilizes the full load-displacement behavior of the shear tie connector. The modeling procedure is briefly described and illustrated, followed by a validation with experimental data. Finally, parametric studies are carried out to assess the effect of the tie stiffness, strength, and deformation capacity on the global performance of the insulated wall panel.

As an insulated panel is subjected to an out-of-plane load, the two panel wythes begin to deflect. As the load increases, the horizontal shear on the panel increases causing relative slip between the two wythes placing demands on the shear ties. This relative slip invalidates the assumption of plane sections through the entire panel thickness; however, the assumption is still valid for each individual wythe. As presented in the experimental results, all the insulated panels exhibit measurable end-slip indicating that the panels are not acting composite or that the assumption of composite behavior is not correct. To this end, the analytical model assumes that end-slip will occur regardless of the level of composite behavior achieved.

First, a section analysis is performed to compute the moment-curvature relationship for A) Composite section and B) Non-composite section as shown in Figure 31. The moment-curvature relationship for the composite section, M_C-φ, is calculated by assuming a linear

www.manaraa.com

strain profile through the entire cross section. For the non-composite section, moment-curvature relationships are calculated for both the interior, M_{bot}-φ, and exterior wythe, M_{top}-φ. From compatibility, the relative deflection of each wythe must be equal assuming no out-of-plane separation occurs. For the deflection of each wythe to be equal at all points along the length, the curvature along the length of each wythe must also be equal. The moment-curvature relationship of the exterior and interior wythe are then summed to form the non-composite moment-curvature relationship, M_{NC}-φ.

Once the moment-curvature relationships are determined for the composite section and the non-composite section, curvature over the length of each panel can be computed by A) Applying an incremental load, w_i, B) Computing the moment distribution by applying the boundary conditions for each incremental load, and C) Utilizing the moment-curvature relationship to determine curvature over the length as shown in Figure 45. D) Load-deflection points for the composite and non-composite panels are computed by virtual work or another method for each load increment, w_i, while full load-deflection responses are computed through iteration, step E1.

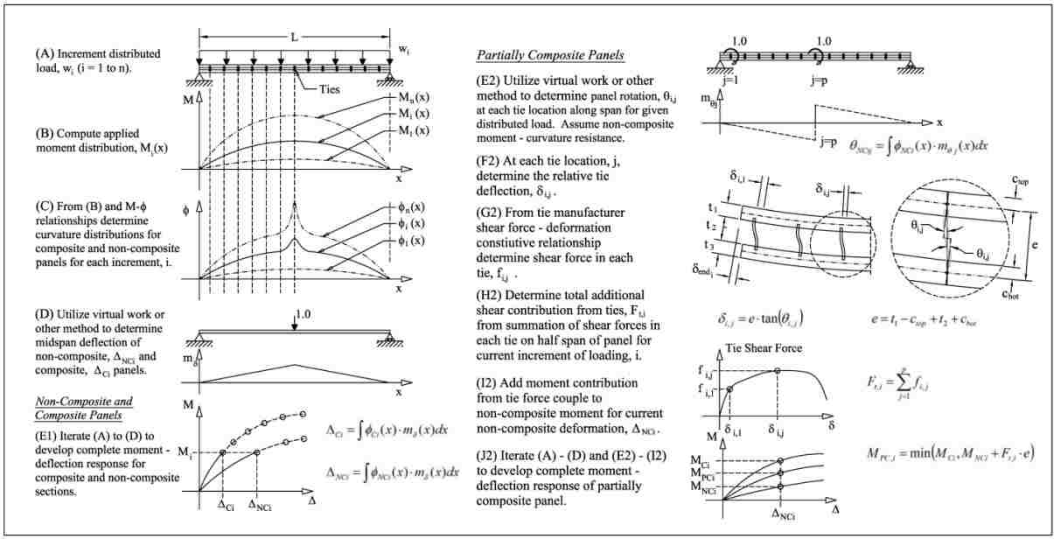

Figure 45: Response estimation for partially-composite panels

www.manaraa.com

To compute the load-deflection response of a partially-composite panel, M_{PC}-Δ_{PC}, the procedure for the non-composite panel is followed up to step D in Figure 45. Once M_{NC}-φ is known, rotations are computed at each tie location for each $\varphi_i(x)$ as shown in step E2 in Figure 45. At each tie location, the relative tie deformation is computed in step F2 and converted to an equivalent force using the tie constitutive properties (step G2). The force contribution from the shear ties at each φ_i is added as an additional panel moment to the non-composite moment at each $\Delta_{NC,i}$ by multiplying the summation of the shear tie forces by the distance between the interior and exterior wythe neutral axis, e, as shown in step H2 and I2. The total M_{PC} must be less than M_C as it is not possible to exceed the composite moment capacity. The process is iterated in step J2 until the complete M_{PC}-Δ_{PC} is computed.

Validation of Analytical Approach

The proposed analytical method is validated against four different experimental panel averages, PtEL, PtEG, RtEG, and RtXC. The panels were selected to check the robustness of the model for different shear ties including distributed and discrete ties, as well as prestressed and non-prestressed reinforcing. Figure 46 (a), (b), (c) and (d) plot the average experimental results of panels PtEL, PtEG, RtEG, and RtXC, respectively against the partially-composite analytical model titled “estimated response”. Expected composite and non-composite panel behaviors computed using the aforementioned procedure act as bounds and are shown in each plot. The computed end-slip is plotted against the experimental end-slip of each panel on the secondary ordinate. In general, the analytical model conservatively predicts the response of each panel.

www.manaraa.com

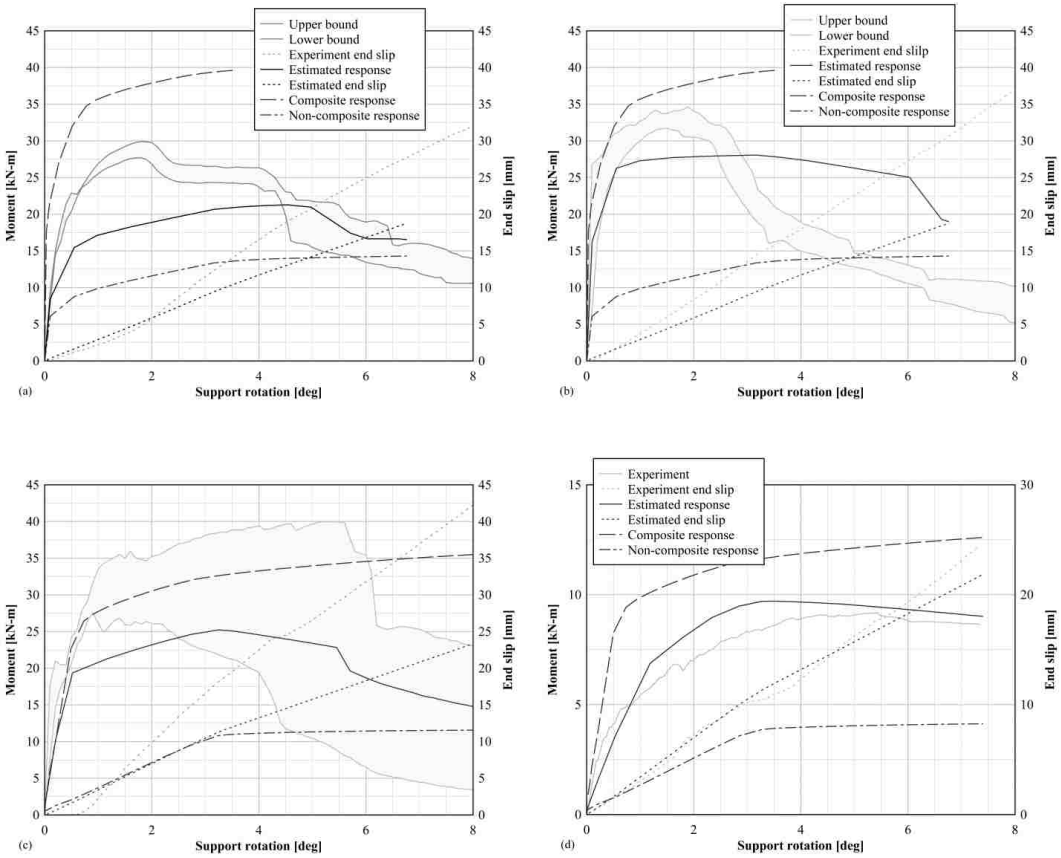

Figure 46: Analytical model validation (a) PtEL, (b) PtEG, (c) RtEG, (d) RtXC

Influence of Ties on Insulated Panel Response

A parametric study is conducted to assess the effect of shear tie constitutive property on overall panel performance. A panel measuring 813 mm wide, 3.66 m long panel with 76.2 mm thick wythes and 50.8 mm of insulated was reinforced with two #16 deformed bars in each wythe. The wythes were connected with two rows of eight shear ties spaced at 406 mm. The stiffness, strength, and ductility was varied for the shear tie system as shown in Figure 47. Six different hypothetical ties were considered: 1) Linear-elastic tie, 2) Elastic-plastic tie with the same stiffness as the linear-elastic tie, 3) Elastic-brittle tie with the same stiffness as the linear-elastic tie and fails at the yield point of the elastic-plastic tie, 4) Elastic-softening tie with the same properties as the elastic-plastic tie with a post yield

www.manaraa.com

softening branch, 5) 8x as stiff tie with the same properties as the elastic-softening tie but with eight times the initial stiffness, 6) ½ as stiff tie with the same properties as the elastic-softening tie but with half the initial stiffness. All six panels were identical other than the shear tie system.

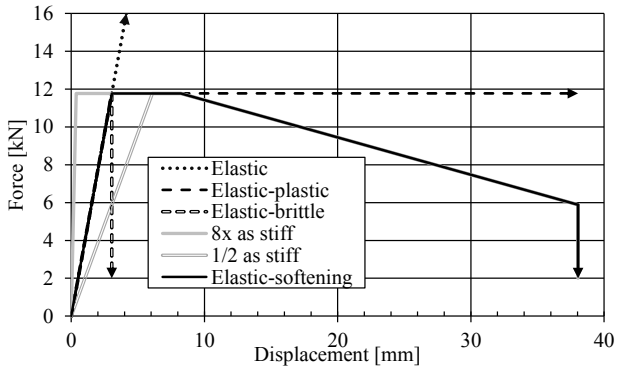

Figure 47: Parametric study tie parameters

The moment-rotation response and force in each shear tie at 1.5° of support rotation are provided in Figure 48 (a) and (b) respectively. The parametric study reveals the dependence of the overall panel response to the tie-behavior. Additionally, the parametric study results agreed with the results observed in experimental tests: 1) A stronger tie provides a higher moment-capacity, 2) A tie with larger deformation capacity increases the panel deformation capacity, 3) A brittle tie initially increases the panel capacity but the panel strength degrades to that of the non-composite behavior as the ties fail, 4) A stiffer tie increases the initial stiffness of the panel, 5) A less stiff tie decreases the initial stiffness of the panel.

Additionally, tie force is shown to vary along the span length. The distribution of tie forces along the half-span is illustrated for all cases at a panel rotation of 1.5° in Figure 48b. Ties located at different locations along the length of the panel contribute different amounts to

www.manaraa.com

the overall resistance. At a given demand level some ties in the panel may have fractured, some may be at yield, while others are still elastic and not contributing their full capacity.

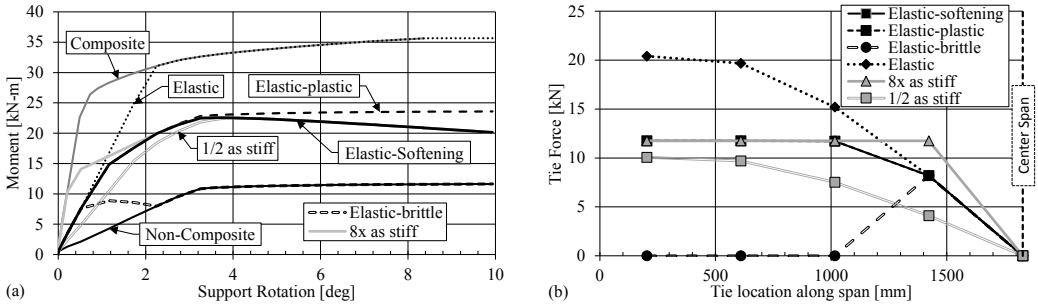

Figure 48: (a) Moment-rotation behavior, (b) Force in each shear tie along span length

4.4.8. Insulated Panel Performance Conclusion

A total of 51 insulated and solid panels were tested under a uniform load increasing monotonically. Various insulation types, insulation thicknesses, shear tie systems, and shear tie layouts were utilized. The results are used to develop an analytical approach for determining the response of insulated concrete panels subjected to flexure. Several conclusions were drawn from the experimental tests and modeling:

- As illustrated through experimental tests on solid panels and analytical modeling, prestressed panels have less deformation capacity than non-prestressed panels due to smaller ultimate material strains; however, prestressed panels have a stiffer initial response compared to non-prestressed panels due to the initial jacking force of the prestressed delaying the onset of cracking. The improvements in ductility are diminished for insulated panels with low levels of composite action.

- All insulated panels tested have measurable end-slip despite the fact that some of the panels achieve a fully composite behavior, indicating that the assumption of composite behavior is incorrect.

www.manaraa.com

- The PCI design approach is based on force equilibrium alone and does not consider the constitutive properties of the connector or compatibility between the wythes. This methodology may be acceptable for handling and service loads, but for panels loaded to their nominal strength a deformation based approach is necessary. Additionally, the PCI approach may lead to an unconservative design, particularly if brittle shear ties are utilized.
- For the panels examined, the PCI design approach generally provides a conservative estimate of percent composite action. The design composite level was typically lower than the actual composite level achieved.
- As illustrated through experimental testing and parametric studies, the global performance of an insulated panel is dependent on the constitutive properties of the shear connector: stiffness, strength, and deformation capacity, as well as tie placement within the panel.
- An analytical approach is developed which accounts for equilibrium, compatibility, and the constitutive properties of the ties. The approach provides an accurate method for determining the moment-deflection of partially-composite panels.

4.5. Shear Tie Development

From the conclusions of the Insulated Panel Performance section, the shear tie constitutive properties play a large role in controlling the overall behavior of the panel. In order to improve the response of an insulated wall panel while at the same time making the panel more economical to fabricate, a new shear tie system was developed. The following section outlines the procedure for designing the new shear connector.

www.manaraa.com

4.5.1. Shear Tie Background

Insulated reinforced concrete wall panels have become an increasingly popular cladding system since their conception. Precast insulated wall panels provide the same benefits as their counterpart solid wall panels including structural strength, efficient erection, and economic fabrication; however, insulated panels provide the additional benefit of increased sustainability due to the enhanced thermal resistance provided by the insulating layer. To match the structural strength of a solid wall panel, insulated wall panels often contain a series of discrete or distributed shear connectors which pass through the insulating layer, directly connecting the interior and exterior wythes allowing the wythes to resist applied demands conjunctly.

The shear connectors must be designed such that the capacity is greater than the expected factored service loads or the overall wall panel stiffness/strength will be reduced to a partially composite level. Additionally, shear ties must utilize thermally resistive material to negate the costly effect of thermal bridging. Many popular contemporary shear tie systems are fabricated from glass fiber reinforced polymer (GFRP) which often has a lower thermal conductivity than the wall insulating material, typically extruded or expanded polystyrene, thus preventing thermal bridging.

Although insulated panels are designed utilizing shear ties to meet a prescribed demand and thermal resistance, they often suffer from quality control problems during fabrication. For shear ties to reach the capacity for which they are designed, they must be placed at specific locations and with defined embedment otherwise the capacity of the ties may be controlled by the strength of the concrete, due to pull-out or pry-out failure mechanisms, rather than the strength of the tie. Additionally, in poorly executed installations concrete may bleed past the shear tie creating a large thermal bridge reducing the overall panel

www.manaraa.com

thermal resistance. To ensure proper installation, extra effort must be taken by the fabricator during shear tie placement translating to a longer production time and additional expense.

Finally, shear ties currently available are designed to withstand conventional life cycle loads such as lifting during construction and wind loads during service; however, no shear ties exist which account for extreme events such as a blast load. Most government facilities mandate both energy and security requirements. An ideal solution to both requirements is a precast insulated wall panel with shear ties designed for high explosive detonations. In blast design, the primary mode of energy dissipation is panel deformation. By designing a shear tie with a large amount of ductility, the wall panel can displace more energy generated during a detonation before failing reducing the risk to inhabiting occupants.

4.5.2. Shear Tie Goal Goal

The goal of this part of the research is to design, fabricate and test a prototype shear connector capable of achieving nearly full-composite action under factored service loads. The shear tie will be constructed from a thermally resistant material and will prevent concrete from bleeding past the connector to diminish any effect from thermal bridging. Additionally, installation of the tie system will be simple to decrease labor time required for panel fabrication and reduce overall cost without comprising the integrity of the connector. Finally, the tie will be designed to improve the insulated panel response to a blast demand by inducing a ductile response with sustained resistance under large deformations.

www.manaraa.com

4.5.3. Material

Ties will be cut from a sheet of GFRP, namely G10 Garolite. Carbon fiber was initially considered for the tie material; however, the cost to produce each tie greatly exceeded the cost savings rendering the tie as unmarketable. GFRP is currently a popular material for the fabrication of shear ties due to the high strength, excellent insulating properties, ease of fabrication, and economic production. Furthermore, GFRP has a similar thermal expansion coefficient and Poisson ratio to concrete mitigating additional stresses from temperature changes and in directions other than the loading surface. Table 11 provides ranges of pertinent G10 Garolite properties while the typical Poisson's ratio is 0.12 (Steinberg 2000).

Table 11: G10 Garolite mechanical properties (McMaster-Carr 2013)	
Nominal Density (lbf/cu.in.)	0.069
Tensile Strength (psi)	32,000-40,000
Compressive Strength (psi)	35,000-68,000
Flexural Strength (psi)	45,000-55,000

4.5.4. Calculations

For initial sizing, a generic prestressed insulated wall panel section is assumed. The panel consists of a 2 in. (50.8mm) layer of insulation sandwiched between 3 in. (76.2mm) thick exterior and interior concrete wythes as shown in Figure 49. A single 3/8 in. (9.53mm) 270kip (1201kN) low relaxation prestress strand is located at the center of each wythe and is initially jacked to 60% of ultimate stress. Concrete strength was assumed to be 7000psi (48.26MPa) at 28 days. The width of the panel was determined to be 21.5 in. (546mm) such that the average compressive force in the concrete was equal to 225psi (1551kPa), meeting ACI 318-11 18.11.2 requirements to minimize transverse reinforcement (ACI 2011). The panel was taken as simply supported with a span length of 20.5ft (6.25m). Once the geometry of the panel is known, the nominal moment capacity of the section is

www.manaraa.com

determined via strain compatibility.

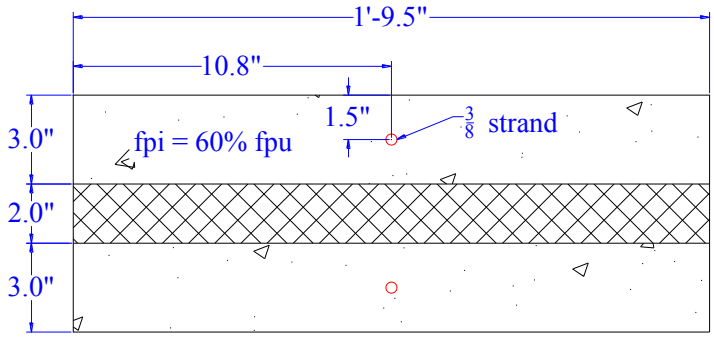

Figure 49: Panel cross section

4.5.5. Tie Demands

The following sections list the demands expected on a shear tie in an insulated panel.

Direct Tension Demand

The tension demand is determined by calculating the weight the exterior panel wythe. During fabrication, lifts are casted into interior wythe of the panel. Once the concrete has cured, the panel is lifted at the installed lift points thus creating a demand on the shear ties equal to the weight of the exterior panel wythe, w_{dem}, as shown in Equation 21. An additional 10% is added to the panel weight to account for suction between the concrete and the formwork. Normal weight concrete was assumed at 150pcf (23.5kN).

$$w_{dem} = 1.1bt_{wythe}\gamma_c L \qquad \text{Equation 21}$$

where b is the width of the panel, t_{wythe} is the thickness of the exterior wythe, L is the panel span length and γ_c is the unit weight of concrete

Horizontal Shear Demand

Horizontal shear demand, v_{dem}, is calculated by taking the maximum of two different methods: 1) Mechanics of materials approach, 2) PCI Approach. The mechanics of materials approach first calculates the vertical shear in the panel by assuming a distributed

www.manaraa.com

loading case where the distributed load, w, is the load required to reach the nominal moment capacity. The maximum shear, v_{max}, is then found with Equation 22 while the average shear, v_{avg}, is calculated with Equation 23. Horizontal shear force is then determined by calculating the shear flow, q, as shown in Equation 24 and multiplying by half the span length.

$$v_{max} = w * {}^{L}/_{2} \qquad \text{Equation 22}$$

where w is the distributed load

$$v_{avg} = \left[{}^{1}/_{2}\left(\frac{L}{2}\right)v_{max}\right] * \frac{2}{L} \qquad \text{Equation 23}$$

where w is the distributed load and L is the span length of the panel

$$q = \frac{v_{avg}Q}{I} \qquad \text{Equation 24}$$

where Q is the first moment of area and I is the gross moment of inertia for the uncracked composite section

The PCI approach takes the minimum of the ultimate force in the strand at fracture, T, as shown in Equation 25, and the compression force from the entire exterior wythe, C, as shown in Equation 26. The horizontal shear demand for the panel, v_{dem}, is then taken as the maximum between the mechanics of materials approach and the PCI approach.

$$T = A_{ps}f_{pu} \qquad \text{Equation 25 (PCI 2011)}$$

where A_{ps} is the area of the strand in the interior wythe and f_{pu} is the ultimate stress in the strand

$$C = 0.85f'_c bt_{wythe} \qquad \text{Equation 26 (PCI 2011)}$$

where f'_c is compressive strength of the concrete

Tie Flexure Demand

The moment demand, M_{dem}, was calculated by summing moments about one end of the shear tie as shown in Figure 50. The shear tie was assumed to have fixed-fixed boundary

www.manaraa.com

conditions (Woltman, Tomlinson, Fam 2013). The result is provided in Equation 27, utilizing the horizontal shear demand calculated previously.

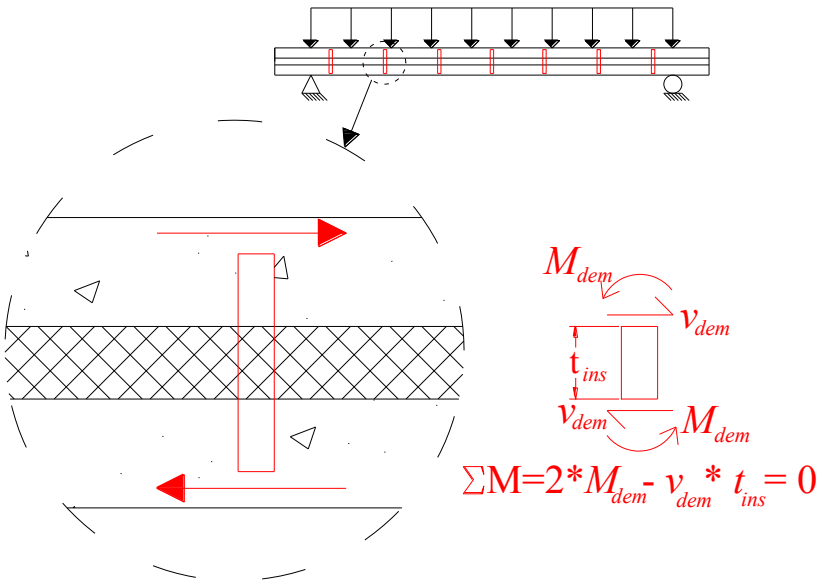

Figure 50: Calculating moment demand

$$M_{dem} = v_{dem} \frac{t_{ins}}{2} \qquad \text{Equation 27}$$

where t_{ins} is the insulation thickness

Rigid Body Rotation

Finally, the vertical force, F_{vert}, developed in each leg of the tie due to rigid body rotation can be approximated by assuming the magnitude of the vertical force in each leg is equal. The force can be solved for by applying equilibrium and utilizing the horizontal shear demand solved for previously. As shown in Figure 51 and Equation 28, the force is a function of the number of legs, leg spacing, and insulation thickness.

www.manaraa.com

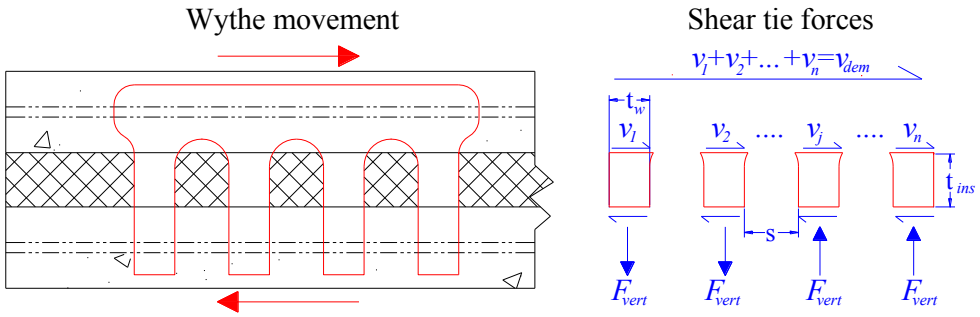

Figure 51: Fictional shear tie with rigid body rotation forces

$$0 = v_{dem}t_{ins} - \sum_{i=0}^{\left(num_{legs}/2\right)-1} \left[2 * F_{vert}\left\{\left(\frac{1}{2}+i\right)(s+t_w)\right\}\right] \quad \text{Equation 28}$$

where L_o is the length of the shear tie, num_{legs} is the number of shear tie legs, s is the spacing between each leg, t_w is the width of each leg and i is a vector from (0, 1, 2,…, (num_{legs}/2)-1) if the number of legs is even or (0, 0.5, 1.5,…, (num_{legs}/2)-1) if the number of legs is odd

4.5.6. Tie Capacity

The tie must be sized in order to have the capacity to meet the demands previously described. Variables that affect the strength of the tie include the number of tie legs (num_{legs}), the width of each leg (t_w), the thickness of the tie (t_t), the spacing between each leg (s), the total tie length (L_o), and the number of ties to be used in the panel (num_{ties}). The following sections detail the sizing of the tie for tensile capacity, pull-out strength, pry-out strength, and plastic moment capacity.

Direct Tension Capacity

The tensile capacity is controlled by the weight of the exterior wythe, w_{dem}, and the tensile strength of the material. Equation 29 below provides the area required for each leg, A_{reqF}, based on the tensile demand.

www.manaraa.com

$$A_{reqF} = {}^{w_{dem}}/_{(f_y num_{legs} num_{ties})} \quad \text{Equation 29}$$

where f_y is the tensile strength of the material

Concrete Pull-out Strength

The pull-out strength of the tie from the concrete is based on ACI 318-11 requirements for anchorage, section D.5.2.1. The projected concrete failure area, A_{NC}, of a group of anchors is approximated as the base of the rectilinear geometrical figure that results from projecting the failure surface outward $1.5h_{ef}$, where h_{ef} is the effective embedment depth of the anchor, from a line through a row of adjacent anchors as shown in Figure 52 (ACI 2011). Equation 30 provides the projected concrete failure area of a single anchor with an edge distance equal or greater to $1.5h_{ef}$.

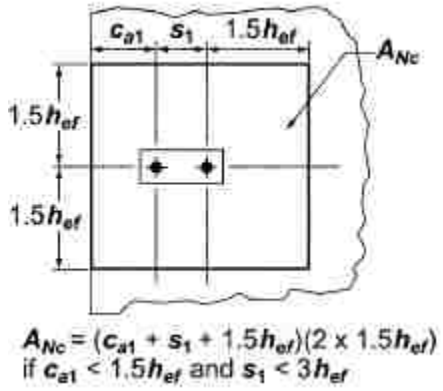

Figure 52: Projected concrete failure area of a group of anchors (ACI 2011)

$$A_{NCo} = (2 * 1.5h_{ef}) * (2 * 1.5h_{ef}) = 9h_{ef}^2 \quad \text{Equation 30 (ACI 2011)}$$

where h_{ef} is the effective embedment depth of the anchor

The basic concrete breakout strength of a single anchor, N_b, is given by Equation 31 while the pull-out strength of a group of anchors, N_{cbg}, is given by Equation 32. The shear ties in this research project are approximated as cast-in-place anchors without any eccentricity with a distance greater than $1.5h_{ef}$ from any edge. The pull-out force, calculated by the

www.manaraa.com

product of the pull-out strength, N_{cbg}, the area of each tie (the summation of each leg cross sectional area) and the total number of ties must be greater than the tensile demand i.e. the weight of the exterior wythe, w_{dem}.

$$N_b = k_c \lambda_a \sqrt{f'_c} h_{ef}^{1.5} \qquad \text{Equation 31 (ACI 2011)}$$

where k_c is a constant equal to 24 for cast-in-place anchors, λ_a is equal to 1.0 for normal weight concrete, and f'_c is the compressive strength of concrete in psi

$$N_{cbg} = \frac{A_{Nc}}{A_{Nco}} \psi_{ec,N} \psi_{ed,N} \psi_{c,N} \psi_{cp,N} N_b \qquad \text{Equation 32 (ACI 2011)}$$

where $\psi_{ec,N}$ is a modification factor for eccentrically loaded anchors taken as 1.0, $\psi_{ed,N}$ is a modification factor for edge effects taken as 1.0, $\psi_{c,N}$ is a modification factor for anchors located in regions where analysis indicates no cracking at service load levels taken as 1.25 for cast-in-place anchors, $\psi_{cp,N}$ is a modification factor that only applies to post-installed anchors (taken as 1.0 for cast-in-place anchors)

Concrete Pry-out Strength

The pry-out strength is calculated from ACI 318-11 section D.6.3.1, which is the product of the pull-out strength, N_{cbg}, and k_{cp} where k_{cp} is a modification factor equal to 1.0 for effective embedment depths less than 2.5 in. or 2.0 for embedment depths greater than or equal to 2.5 in. The force required for pry-out is calculated as the product of the pry-out strength, the area of each tie (the summation of the cross sectional area of each leg) and the number of ties. Pry-out force must be greater than the shear demand, v_{dem}.

Tie Moment Capacity

The moment capacity is determined by the standard plastic section analysis typically performed for steel sections. To be conservative, the capacity is calculated up to yield of the material as shown in Figure 53. Stress-strain behavior of the material may be adjusted once material tests are performed. The moment capacity provided in Equation 33 must be

www.manaraa.com

greater than the moment demand, M_{dem}.

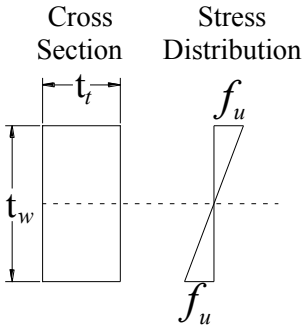

Figure 53: Stress distribution for moment capacity calculation

$$M_p = \left[\frac{1}{2} f_u \left(\frac{t_w}{2}\right)\left(2/3 \frac{t_w}{2}\right)\right] 2t_t \qquad \text{Equation 33}$$

where t_w is the width of each leg, t_t is the thickness of the tie, and f_u is the flexural strength of the tie

Resin Matrix Shear Capacity

Finally, assuming the tie is fabricated such that the fibers are running in one direction, the strength of the vinyl-ester resin in shear may control the capacity of the tie. A basic mechanics of materials approach approximates the area required based on the strength of the resin in shear, A_{reqR} (Woltman, Tomlinson, Fam 2013) shown in Equation 34.

$$A_{reqR} = \frac{k v_{dem}}{f_{ur}} \qquad \text{Equation 34 (Woltman, Tolinson, Fam 2013)}$$

where v_{dem} is the horizontal shear demand, f_{ur} is the strength of the resin, and k is the shear factor taken as 1.5 for a rectangular cross section

4.5.7. Additional Design Considerations

Hard design constraints require that the shear tie thickness, leg width, number of legs, leg spacing, and leg depth are selected such that the capacity satisfies the demand. The calculations presented in the previous section were performed on the aforementioned panel

www.manaraa.com

size to determine the shear tie size. Additional soft design constraints were considered including the practicality of fabrication, ease of installation in the wall panel, and efficient use of material for economic savings.

The end treatment of each leg of the shear tie was selected based on a series of experimental parametric studies. Four different end treatments were tested for straight connectors: pointed ends, notched ends, ties with lock washers, and threaded ties with special nuts (Woltman, Tomlinson, Fam 2013). None of the ties failed due to pull-out from the concrete, indicating that all the end treatments were sufficient despite the relatively short embedment depth of 2.0 in. (51mm). A pointed end was selected for the shear tie design due to the ease of fabrication. Furthermore, a shear tie with a pointed end facilitates installation by allowing the fabricator to perforate the insulation simply by apply pressure to the connector. Finally, by penetrating the insulation directly with the shear tie rather than precutting a hole to fit the connector further reduces cost and minimizes the probability of thermal bridging due to concrete bleeding along the tie. To be conservative, the embedment depth was selected by comparing the pull-out capacity to the tension demand.

The cross sectional shape, rectangular versus circular, did not have a significant effect on the strength or stiffness of the shear tie (Woltman, Tomlinson, Fam 2013). A rectangular shape was chosen for the connector design, allowing the shear tie to be cut from a sheet of GFRP. The thickness of the GFRP sheet, the width and spacing of each leg was determined by comparing various capacities to limit states.

In addition to performing capacity calculations to determine the spacing of each shear tie leg, the spacing and overall length of the shear tie was checked against the human hand ensuring that the fabricator can comfortably install shear ties in a rapid and repeatable

www.manaraa.com

manner. The overall shape of the shear tie was selected for optimal ergonomics. Finally, the dimensions of the shear tie were also selected to allow for the most efficient use of the GFRP material. The shear tie with primary dimensions and manufacturing layout is shown in Figure 54. Calculations determined that a total of 6 shear ties would be required for a 20.5ft (6.25m) panel, 3 at each end as shown in Figure 55.

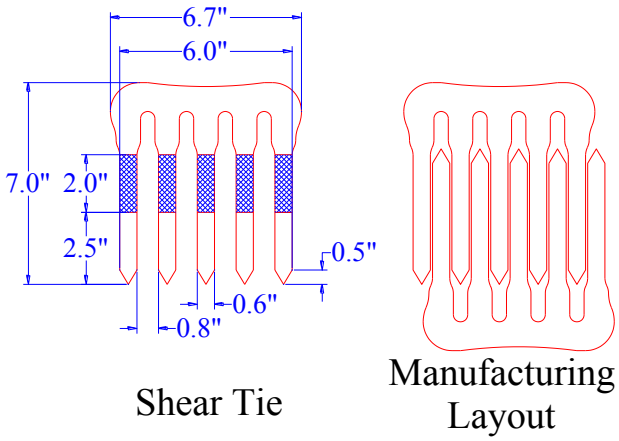

Figure 54: Initial shear tie dimensions and layout

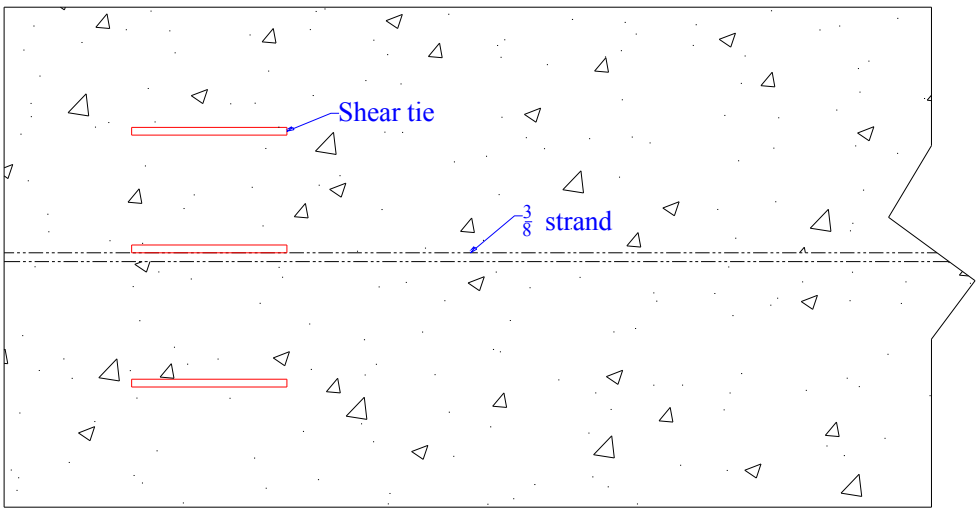

Figure 55: Shear tie layout in panel

www.manaraa.com

Finally, the use of uni-directional fibers in resin will allow the tie to form a ductile mechanism suitable for large deformations. During failure, cracks begin to form in the resin gradually allowing the fibers to delaminate from the matrix (Woltman, Tomlinson, Fam 2013). Failure of the ductile resin matrix as opposed to the brittle fiber allows the tie to reach larger deformations, increasing the maximum obtainable global deflection of the panel.

4.5.8. Tie Redesign

To improve economy the tie was redesigned in order to fabricate more ties per single sheet of G10 Garolite. The redesign included decreasing the overall width of the tie by reducing the number of legs and increasing each leg size. The tie capacity was checked against the tie demands by the aforementioned procedure. Figure 56 depicts the tie redesign with dimensions. The same manufacturing layout as shown in Figure 54 was applied to reduce material waste and to leave space to fabricate material coupons.

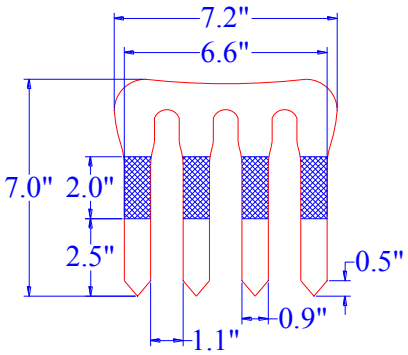

Figure 56: Tie redesign

4.5.9. Material Tests

Three concrete cylinders were prepared according to ASTM C31/C31M-12 (ASTM C31/C31M-12 2012) and tested according to ASTM C39 (ASTM 2005). Metal caps were

www.manaraa.com

used during testing in accordance with ASTM C617/C617M-12 (ASTM C617/C617M-12 2012). The three cylinders had an average compressive strength of 6400psi with a standard deviation of 150psi and a variance of 2.3%. The elastic modulus of the concrete was empirically calculated by assuming normal weight concrete, w_c of 150pcf, and using equation 8.5.1 in ACI 318-11 provided as Equation 35 for convenience.

$$E_c = w_c^{1.5} 33 \sqrt{f'_c} \qquad \text{Equation 35 (ACI 2011)}$$

In addition to design values provided by the manufacturer (McMaster-Carr 2013), material tests were performed to assess the material strength of the G10 Garolite. Tensile coupons were fabricated and tested according to ASTM D638-10 (ASTM 2010) in an Instron 5567 electromechanical load frame. Video was recorded of each test in order to perform digital image correlation. Digital image correlation allowed the strain to be computed at each frame without physically applying gauges. Frames automatically began recording as the load frame commenced. Figure 57 shows a typical speckle pattern applied to one of the tensile coupons as well as a screen capture of the digital image correlation software.

www.manaraa.com

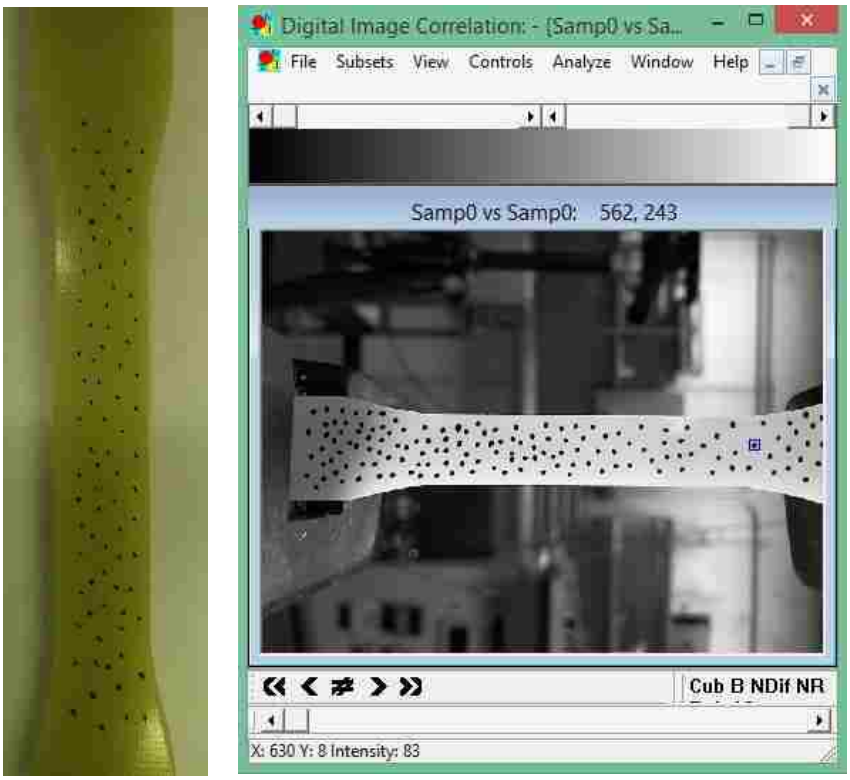

Figure 57: Typical speckle pattern and digital image correlation

The digital image correlation software tracks the movement of an indicator, such as a black dot on a white surface, with the progression of each frame. The movement of the indicator relative to the original frame is reported for each frame in pixels. A second indicator with the precise distance known, in pixels, to the first indicator and the process is repeated. Engineering strain is calculated by taking the quotient of the difference between the first and second indicators and the original distance between the first and second indicators. The stress is calculated by taking the quotient of the load reported by the Instron frame and the cross section of the tensile coupon. The cross section of the tensile coupon was measured with a digital caliper with a precision of 0.005in at three different locations along the neck and averaged. Figure 58 provides the stress-strain results for the two tensile tests performed on the G10 Garolite.

www.manaraa.com

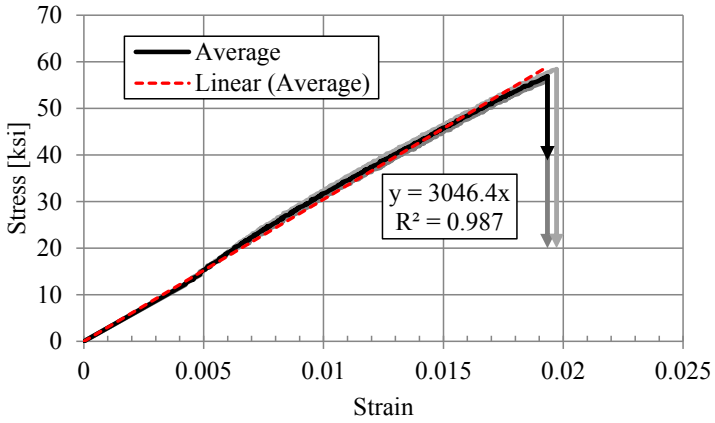

Figure 58: G10 Garolite tensile test results

An average stress-strain curve was produced from the two stress-strain results by averaging the stress levels at each strain increment. As shown in Figure 58, the Garolite performs in a nearly elastic-brittle manner. A linear trend line was fitted to average curve with an R^2 of 0.987 to be used in modeling.

As shown in Figure 51, as the insulated panel is subjected to an out-of-plane load the interior and exterior wythes begin to slip relative to one another. The relative slip results in a horizontal shear demand applied to the shear ties connecting the wythes. In order to assess the material strength of the G10 Garolite in shear, shear coupons were devised as shown in Figure 59. To maintain a direct comparison the coupons were designed such that the shear portion had the same length and width as the fingers on each tie. The rest of the tie was made significantly thicker to attempt to force failure in shear rather than tension or bending.

www.manaraa.com

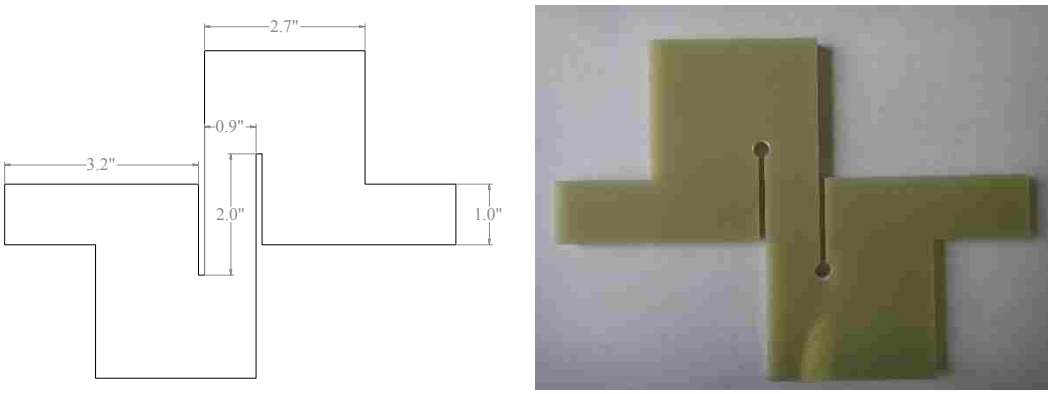

Figure 59: G10 Garolite shear coupon

After testing the first shear coupon it was noted that failure occurred by a crack forming as shown in Figure 60. The crack formed at the slit where the shear leg connects to the rest of the shear coupon due to prying action. To prevent the crack from forming, stress relieving holes were drilled at the tip of each slit as shown in Figure 59; however, the same failure mechanism occurred.

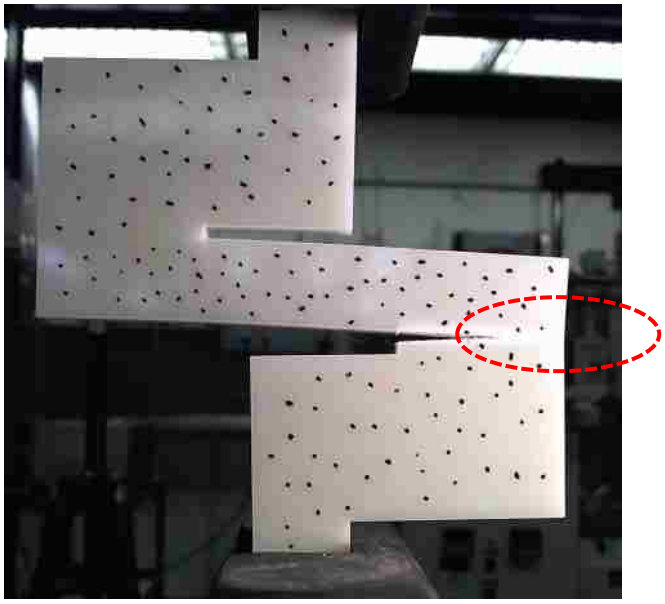

Figure 60: Shear coupon failure

The load-displacement for the two shear coupons tested is shown in Figure 61. Digital

www.manaraa.com

image correlation was performed to determine the total tie displacement rather than using head travel where slip occurring in the grips cannot be distinguished from actual tie displacement. Pixels were converted to inches by measuring the neck width of the shear coupon prior to testing and then calculating the width of the neck in pixels. The same procedure applied to the tensile coupons for averaging curves was applied to the shear coupons.

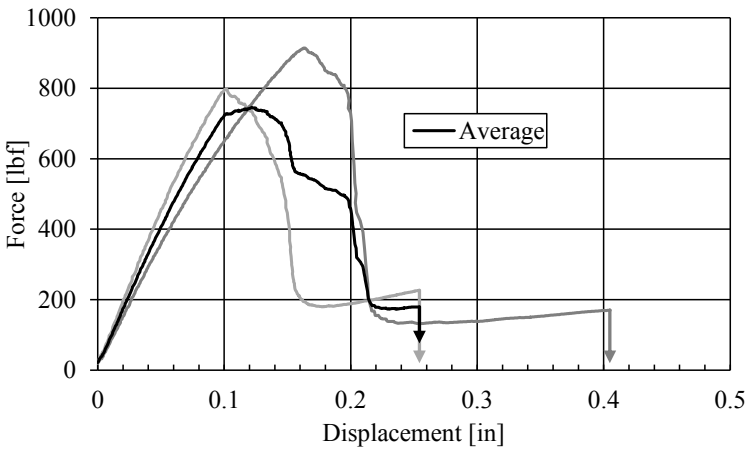

Figure 61: Shear coupon load-displacement

4.5.10. Finite Element Analysis

Finite element models were created for both the original design and the redesign using the multi-purpose finite element software Abaqus. Drawings of the shear tie were uploaded directly from AutoCAD. Ties were embedded in three inch thick concrete wythes on each side to replicate actual conditions as shown in Figure 62. The bottom concrete wythe was fixed from translating or rotation while a displacement was applied to the top concrete wythe. An embedded interaction (Dassault Systemes 2010) was selected between each host instance (concrete wythe) and the embedded instance (shear tie).

www.manaraa.com

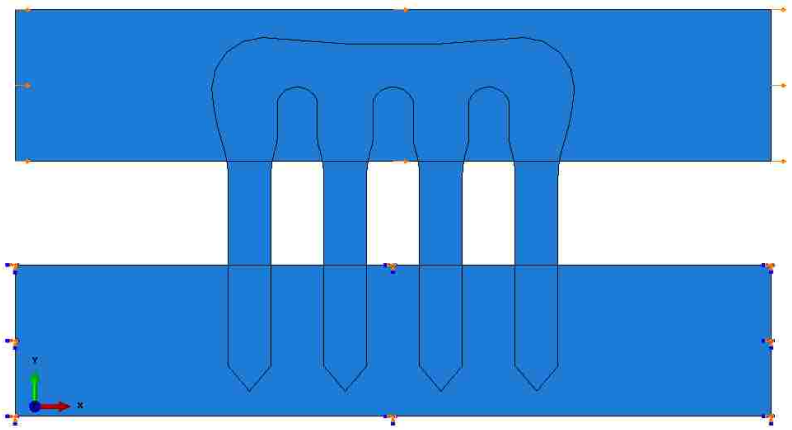

Figure 62: Finite element shear tie embedded in concrete wythes with boundary and loading conditions

The concrete wythes and shear tie were meshed with 6-noded quadratic plane stress triangles in order to capture flexure of each tie leg. To simplify modeling, both the concrete and tie material were treated as elastic using the aforementioned material properties. Additionally, G10 Garolite is an anisotropic material; however, the tensile properties were only determined in one direction. The finite element model was created to qualitatively determine any areas of high stress concentration and assess if changes in the design are necessary. Figure 63 depicts Von Mises stress contours for both the original tie and the redesigned tie.

www.manaraa.com

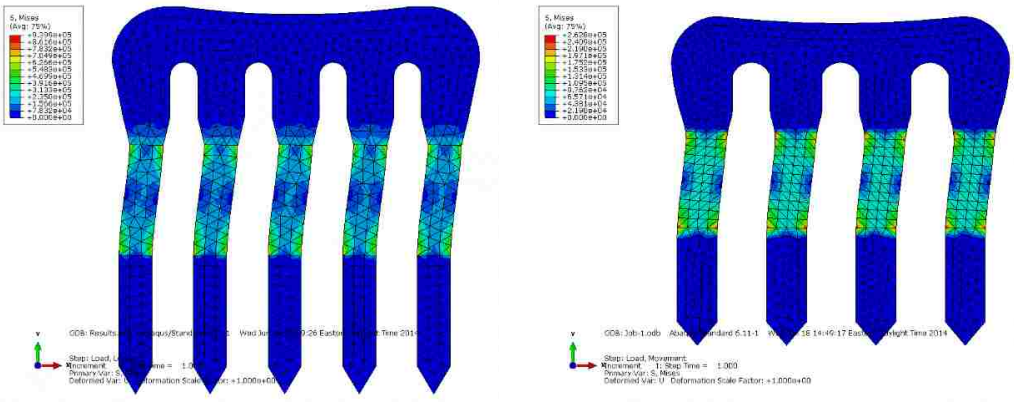

Figure 63: Von Mises stress contours of the original tie and the redesigned tie

Figure 64 provides a close-in view of the Von Mises stress contour for the redesigned tie legs. High stress concentrations were noted at the interface of the concrete and tie. No additional redesign was performed, but it was concluded that this would be the location for incipient failure.

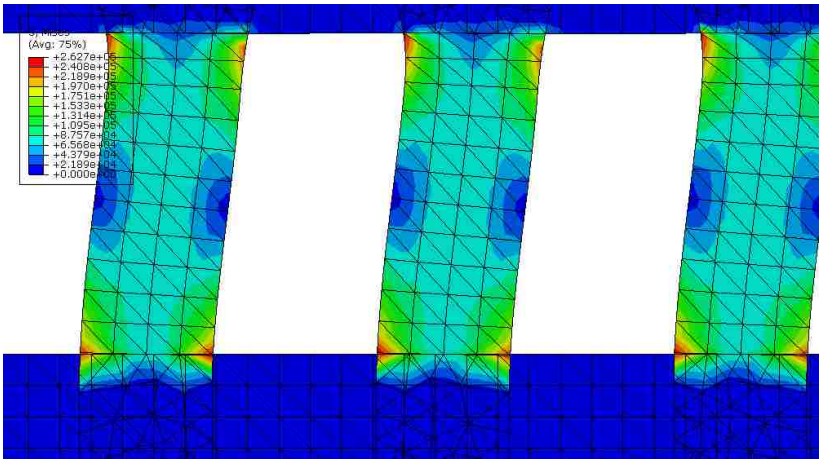

Figure 64: Close-in of Von Mises stress contour of redesigned tie legs

4.5.11. Tie Fabrication

Eighteen shear ties were cut from a two feet by three feet sheet of quarter inch thick G10 Garolite purchased from McMaster-Carr. Cuts were made by a waterjet with a precision of

www.manaraa.com

.001in. No information was provided by the manufacturer to indicate the fiber orientation of the laminate. Figure 65 shows a single shear tie after cutting.

Figure 65: Final shear tie

Four double shear test specimen (Naito et al. 2012) were fabricated with four ties in each specimen. Welded wire was placed in each wythe to secure the concrete during handling and loading. Threaded bar with a washer at the end was attached to a coupling nut and embedded at the top of the specimen to allow for easy lifting with eyebolts. Holes were precut into the two inch thick extruded polystyrene (XPS) via a hot knife. Shear ties were then inserted through the precut holes and pushed to the prescribed depth. Figure 66 depicts the fabrication of the test specimen

www.manaraa.com

Test specimen with welded wire

Embedded threaded rod for lifting

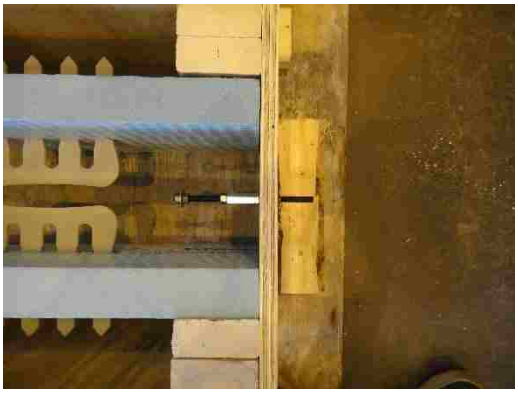

Shear tie placed through XPS

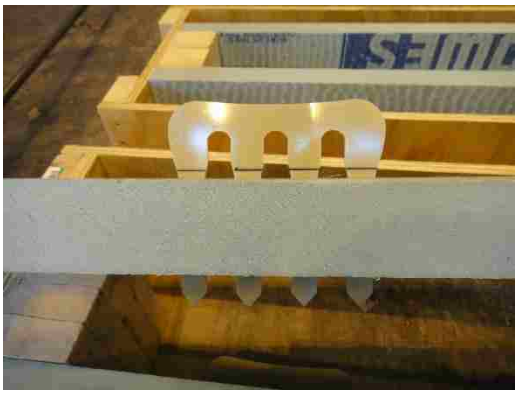

Setting tie at prescribed depth

Figure 66: Fabrication of test specimen

4.5.12. Specimen Test Setup

Ties were tested via a double shear test specimen (Naito et al. 2012) shown in Figure 67. Unlike Naito et al., each test specimen was comprised of four ties rather than two to prevent separation from occurring between the insulation layers and the exterior wythes. The two exterior wythes and insulation layers were three and two inches thick respectively to simulate a typical 3-2-3 wall panel. The interior concrete wythe was six inches thick as ties were embedded on each face. All layers were 34 inches long and 10 inches wide. The ties were spaced to meet ACI 318-11 requirements for embedded anchors. An alternative method for testing ties specified in ASTM E488 Strength of Anchors in Concrete and Masonry Elements (ASTM 2003) was not used, as the aforementioned method provides

www.manaraa.com

similar demands on shear ties in actual insulated concrete panels.

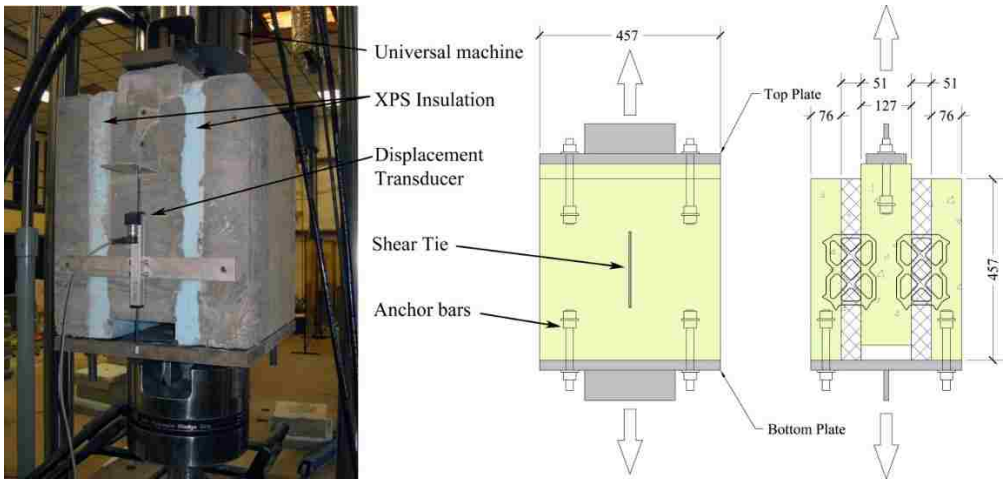

Figure 67: Double shear test setup (Naito et al. 2012)

The test specimen was placed in the universal testing machine standing upright supported by the two exterior concrete layers. The interior concrete wythe was offset from the base of the exterior concrete wythes by 3.5 inches. Ties are then tested by pushing down on the center concrete wythe, thus distributing the compressive force from the interior wythe to the exterior wythes via horizontal shear force. String potentiometers were attached to both sides of the center concrete wythe with an epoxied bolt and connected to the base of the universal testing machine with a hook magnet. Potentiometer readings were averaged to obtain the total deflection. String potentiometers were used rather than the universal testing head travel due to slipping of the loading head. Force was recorded by the load cell inside the universal testing machine. Figure 68 depicts the test specimen in the universal testing machine and the string potentiometers used to record displacement. The specimen was made longer than the tests conducted by (Naito et al. 2012) to prevent pryout from occurring at the ends of the specimen.

www.manaraa.com

Figure 68: New double shear test setup and string potentiometer

4.5.13. Tie Performance

The four double shear test specimen were loaded monotonically to failure. Figure 69 plots the load-deflection response of each test specimen as well as the test specimen average. The average curve was computed by the same procedure used to develop the average tensile test curve. The average performance of each individual shear tie is computed by dividing the average double shear test load-displacement curve by the number of shear ties the double shear specimen.

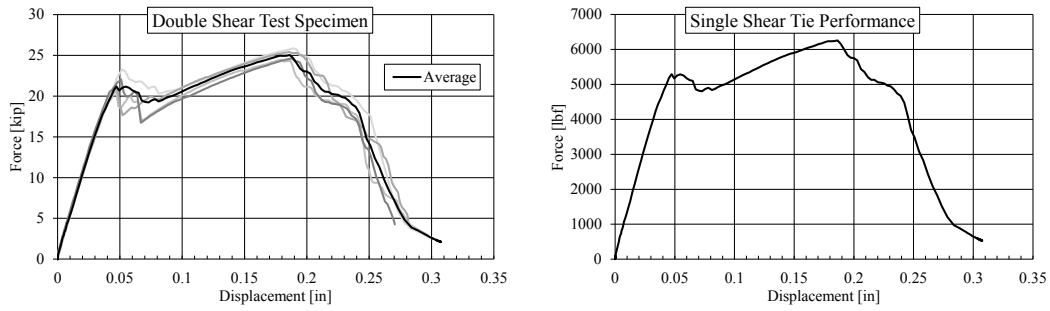

Figure 69: Double shear test and single shear tie performance

A post-failure examination was performed by removing the foam insulation and viewing the exposed shear tie legs. As shown in Figure 70, each of the tie legs failed at the interface between the tie and the concrete. This failure location was expected from the

www.manaraa.com

high stress concentrations show in the finite element model in Figure 64.

Figure 70: Post-failure examination of exposed shear tie legs

The shear tie is compared to other shear connector systems currently available on the market. Figure 71 plots the performance of the shear tie system, dubbed as the "finger tie" due to the design, against other discrete tie systems. As seen in Figure 71, the finger tie lacks the deformation capacity of other discrete ties but is stronger. The small deformation capacity is attributed to the brittle nature of the G10 Garolite material. Additionally, post failure examination revealed that the tie legs were cut perpendicular to the fibers in the laminate, as shown in Figure 72. Thus the fibers were oriented in a direction causing the tie to act in a more brittle manner.

www.manaraa.com

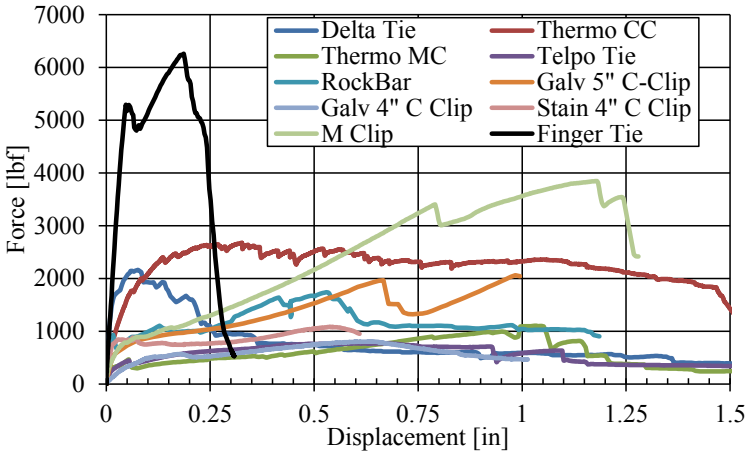

Figure 71: Finger tie comparison to other shear tie systems

Figure 72: Post failure analysis of fiber orientation

4.5.14. Tie Development Conclusion

A shear tie utilizing G10 Garolite was designed based on the nominal moment capacity of a standard insulated panel with a single 3/8 in. (9.53mm) 270kip (1201kN) low relaxation prestress strand in each wythe. The following design criteria were met:

www.manaraa.com

- Minimized thermal bridging by fabricating the tie from thermally resistive GFRP material and utilizing a direct installation method rather than precutting holes to fit the tie
- Maximized panel resistance by designing the tie to meet the nominal moment capacity of the insulated panel
- Decreased cost and installation time by requiring placement of less ties

Based on tests from the initial prototype, several refinements can be implemented to improve the design of the finger tie:

- The finger tie leg size should be decreased while the number of legs should be increased. This would allow for easier installation for panels with thicker insulating foams.
- If the space between each leg is decreased, fingers will no longer be able to fit between each leg. Holes for fingers should be cut to allow for comfort which will increase the installation speed. The hole size and spacing should be based on ergonomics while a new FEA should be performed to assess the integrity of the tie with holes incorporated.
- Garolite is thermally resistive and inexpensive, an ideal material for a shear tie; however, the tie was fabricated from Garolite sheet in such a way that the fiber orientation decreased the deformation capacity of the tie. Either a different inexpensive, uni-directional pultruded material should be used, or the fiber direction should be specified in the Garolite in order to increase the ultimate deformation capacity.

www.manaraa.com

4.6. Flexural Mechanism in Insulated Panels

In an attempt to further improve the flexural response of an insulated wall panel, flexural mechanisms developed for solid panels provided in Flexural Mechanism Development were tested in insulated panels. The dogbone flexural mechanism was not tested due to fabrication difficulties. Further research would be necessary to implement the dogbone method in a larger panel in such a way that construction is feasible, cost is minimally increased, and that the thermal resistance of the panel is not diminished. Thus, to improve the ductility of reinforced concrete wall panels and insulated panels, local unbonding is applied to the longitudinal reinforcement at center span.

4.6.1. Test Matrix

A total of 35 panels were tested with 12 different panel types. Panels varied in reinforcement, shear tie type, and unbonding. A cross section and plan view of the panels is provided in Figure 73. Reinforcement is centered in both wythes. Reinforcement is located at the same depth for solid panels and insulated panels.

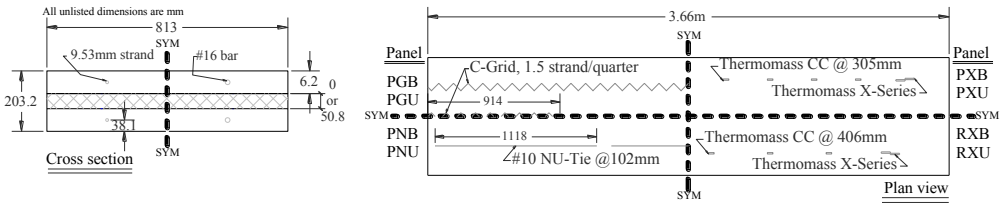

Figure 73: Panel cross section and plan view

Table 12 provides a test matrix giving the panel ID, reinforcement type, shear tie type, whether the specimen was unbonded, and the number of specimen tested. The first letter of the panel ID represents the reinforcement type with "R" for non-prestressed or "P" for prestressed. The second letter of the panel ID represents the tie type with "N" for Nu-Tie,

www.manaraa.com

"G" for C-Grid®, "X" for Thermomass® X-Series, or "S" for a solid panel with no shear ties. The final letter of the panel ID represents unbonding with "B" signifying the reinforcement was completely bonded and "U" signifying the panel was locally unbonded.

Table 12: Test matrix

Panel ID	Reinforcement	Shear Tie	Unbonded	Samples
RSB	Non-prestressed	Solid	No	3
RSU	Non-prestressed	Solid	Yes	3
PSB	Prestressed	Solid	No	3
PSU	Prestressed	Solid	Yes	3
PNB	Prestressed	Nu-Tie	No	3
PNU	Prestressed	Nu-Tie	Yes	3
PGB	Prestressed	C-Grid	No	3
PGU	Prestressed	C-Grid	Yes	3
PXB	Prestressed	X-Series	No	3
PXU	Prestressed	X-Series	Yes	3
RXB	Non-prestressed	X-Series	No	3
RXU	Non-prestressed	X-Series	Yes	2

All unbonded panels were locally unbonded 508mm at center span with Teflon tubing or prestressing sheathing. The ends of the unbonding were taped closed to prevent grout from entering. Figure 74 shows a panel with local unbonding on all four longitudinal bars and a close-up of the unbonding tubing. Panels were simply supported with a clear span of 3.05 m and a total length of 3.66 m. Uniform load was applied via the water bladder described previously. String potentiometers were attached at mid-span and at the ends of each panel to record center span displacement and relative end slips. Panel displacement was converted to support rotation via the method described previously.

www.manaraa.com

Figure 74: Local unbonding of reinforcement

4.6.2. Results

All panels were loaded to failure, to maximum stroke, or until the ends of the panel began to bear against the loading table. Results for each panel are tabulated in Table 13. The end-slip, δ, and support rotation, θ, are provided at maximum moment, M_{max}.

Table 13: Tabulated panel results

Panel ID	**δ @ Mmax**	**θ @ Mmax**	**Mmax**
	[mm]	***[deg]***	***[kN-m]***
RSB	-	5.5	44.9
RSU	-	10.0	42.0
PSB	-	2.2	39.0
PSU	-	1.9	38.4
PNB	2.4	1.2	35.1
PNU	4.3	2.0	35.2
PGB	3.0	1.7	38.5
PGU	3.4	1.3	32.0
PXB	8.3	3.4	36.3
PXU	11.6	4.0	37.4
RXB	3.9	2.3	33.7
RXU	5.6	2.9	33.7

Figure 75 plots the average insulated panel responses comparing unbonded and bonded

www.manaraa.com

panels with the moment on the primary ordinate and the end-slip on the secondary ordinate. Average panel results were calculated via the method described previously at each support rotation increment. Figure 75a plots the prestressed Nu-Tie, Figure 75b plots the prestressed C-Grid®, Figure 75c plots the prestressed Thermomass® X-series, and Figure 75d plots the non-prestressed Thermomass® X-series.

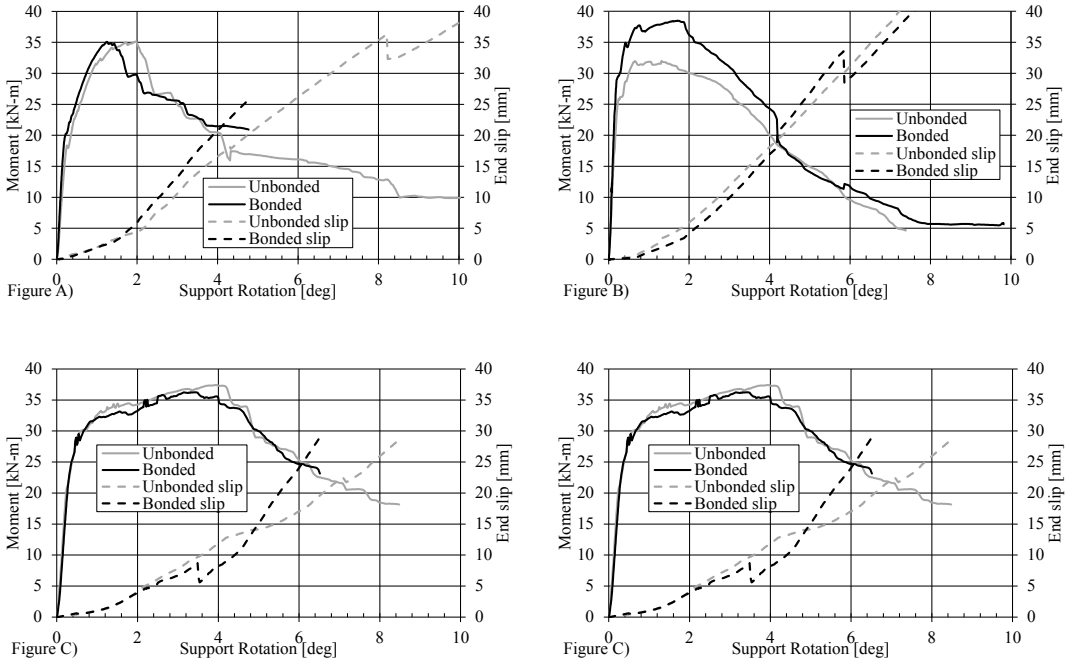

Figure 75: Average panel response A) Prestressed Nu-Tie, B) Prestressed C-Grid®, C) Prestressed Thermomass® X-Series, D) Non-prestressed Thermomass® X-Series

As tabulated in Table 13 and as seen in Figure 75, unbonding appears to make no contributable difference to the insulated panel response. This is attributed to the fact that insulated wall panels utilize shear connectors as shown in Figure 73 which control the panel response. In solid panels where shear ties are not present; however, unbonding may affect the panel response. Figure 76 plots the performance of prestressed and non-prestressed solid panels to local unbonding.

www.manaraa.com

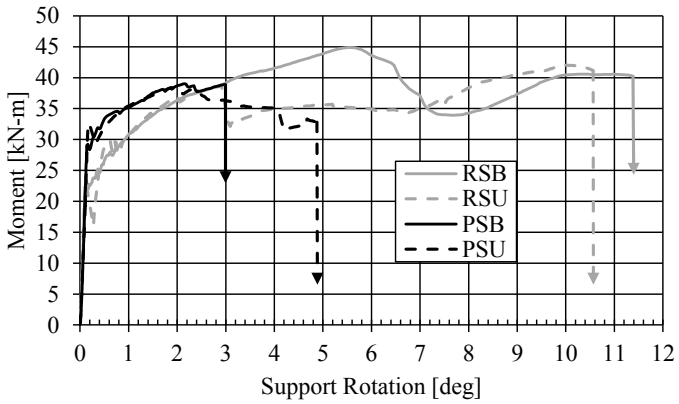

Figure 76: Prestressed and non-prestressed solid panel response to local unbonding

As seen in Figure 76, locally unbonding the prestressed panels increases the ultimate ductility while for non-prestressed panels, locally unbonding decreases the ultimate ductility. However, Table 13 indicates that locally unbonding increases the support rotation at maximum moment for non-prestressed panels while it slightly decreases the support rotation at maximum moment for prestressed panels. Unlike the small slabs tested previously, the localized unbonding does not have a significant effect on the capacity of the panel. Additionally, the effect of localized unbonding on the panel ductility is unclear. Numerical models are recommended to further investigate the performance of the panels.

4.6.3. Analytical Model

The analytical model developed previously for the small slabs is applied to both the non-prestressed and prestressed solid panels. The model is not considered for insulated panels as the response is controlled by the shear ties rather than localized unbonding. Figure 77 provides a comparison between the analytical model for the non-prestressed and prestressed panel to the experimental data. Mill certification and tensile test data provided previously is used for the material constitutive properties. Despite the uncertainty in the effect of unbonding on doubly reinforced panels, the analytical model developed for singly

www.manaraa.com

reinforced slabs provides accurate results for predicting the ultimate deflection and maximum moment for both prestressed and non-prestressed panels. However, the analytical model provides a conservative moment-response in general when compared to the experimental data. A better understanding of the behavior of the system will allow for an improvement in the analytical model.

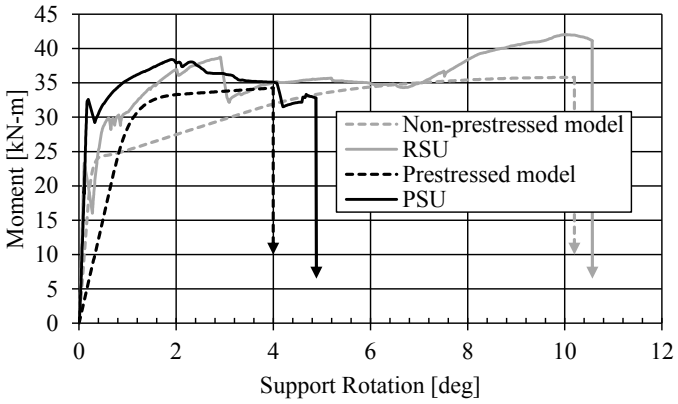

Figure 77: Comparison of experimental data to analytical model

4.6.4. Fleuxral Mechanism in Insulated Panels Conclusion

35 panels of 12 different panel types were tested to assess the sensitivity of a reinforced concrete wall panel's behavior to locally unbonding. The following conclusions were made:

- Experiments indicate that locally unbonding has no significant effect on the performance of an insulated panel. This is attributed to the fact that the response of the insulated panel is controlled by the shear ties.
- The effect of locally unbonding solid, double reinforced prestressed or non-prestressed panels is unclear. Future numerical modeling would provide insight into the behavior of a locally unbonded wall panel.

www.manaraa.com

- The analytical model developed for singly reinforced slabs provides an accurate estimate of the ultimate deflection and maximum moment for both prestressed and non-prestressed panels. However, the method provides a conservative response of both panels in general.

www.manaraa.com

5. CLOSE-IN DETONATIONS

The following section outlines the current methodology for designing a solid reinforced concrete slab for close-in detonations (DoD 2008c). The performance of insulated wall panels to close-in detonations is then discussed with experimental, empirical, and numerical evaluation (Naito et al. 2014b).

5.1. Current Methodology

The assessment of the structural response of buildings subjected to accidental or man-made explosions is important for critical facilities. Generally blast generated demands can be categorized into the far field design range and close-in design range. In the far field design range blast generated pressure demands can be considered uniform on the structure and basic single degree of freedom approximate analysis is often implemented. In the close-in design range blast pressures are non-uniform and the pressure magnitudes can be very high (DoD 2008c). These ranges are categorized by the scaled distance of the detonation relative to the structure. The scaled distance is measured in terms of distance, R, divided by the weight of explosive, W, in kg (lb_f) of TNT to the 1/3 power. A close-in detonation is often considered to exist when the scaled distance is less than 1.2 $m/kg^{1/3}$ (3.0 $ft/lb^{1/3}$).

Following the detonation of a high explosive at a small scaled-distance from a concrete wall a shock wave is generated. Part of the shock wave that strikes the wall surface is transmitted to the concrete, resulting in a compressive wave. When the transmitted shock wave reaches the back surface, it reflects resulting in a tensile wave. If the tensile stress on the back face is greater than the dynamic concrete tensile resistance the concrete will fragment, i.e., spall (DoD 2008c). The front zone can also spall by excessive compressive stress, or if it is subject to a sufficiently strong tensile shock wave as with the back face.

www.manaraa.com

The failure of both back and front face to a depth of at least half the wall thickness each will produce a breach. A breach can also form if the shock front contains enough energy to completely fragment a localized zone through the depth of the wall, or if the tensile waves surpass the tensile capacity of the concrete, creating a void through the entire member.

The amount of spall may vary from the exterior to interior face of a panel depending on the mechanics of the shock wave propagation through the material. Since breach represents the void generated, a singular breach diameter is measured on the wythe. A schematic of spall and breach are shown for an insulated wall panel in Figure 78.

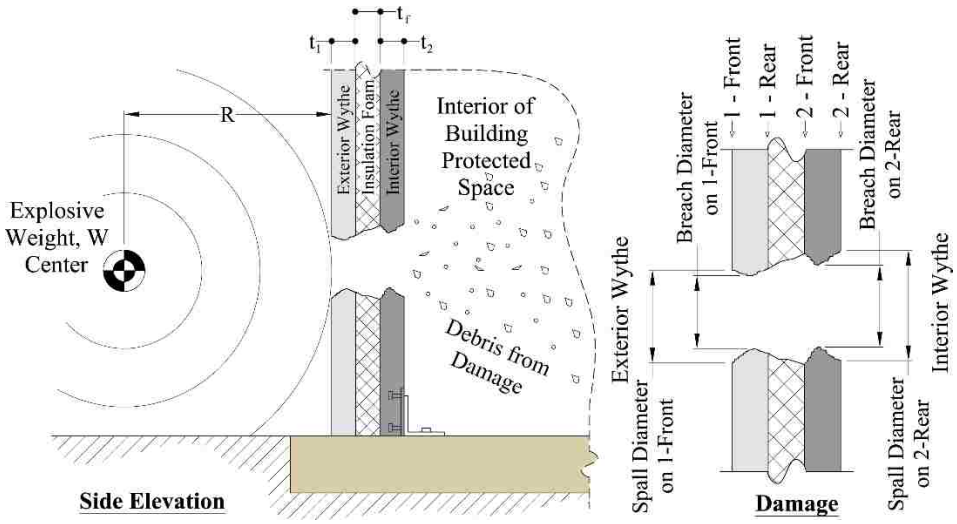

Figure 78: Spall/breach schematic

Resistance to spall and breach in concrete elements is an important design consideration when close-in detonations of high explosives are possible. Spall on the interior face of the structural element can result in the formation of small concrete fragments that can travel at hundreds of feet per second (DoD 2008c). These fast moving fragments in the protected space of the building can result in fatalities and damage to equipment. When breach occurs, the protected space of the building becomes accessible which can be undesirable

www.manaraa.com

for secure facilities. The formation of spall or breach can be predicted for solid elements using empirical methods developed by McVay (1988), Marchand et al. (1994) and DoD (2008). While these methods have been validated for solid concrete elements minimal research has been conducted on multi-wythe concrete panels.

An empirical approach for predicting spall or breach of solid concrete elements is provided in the UFC 3-340-02 (DoD 2008c). In this section, the occurrence of spall and breach is empirically examined for the panels evaluated experimentally. The empirical formulas, provided by the UFC 3-340-02 (DoD 2008c) are used for the solid panel and are adapted to the case of the insulated panels.

The spall and breach threshold curves are extrapolated by experimental tests and are plotted as functions of the spall parameter (ψ) and the ratio between the height of wall section (h) in feet and the stand-off distance (R) in feet. More details about these curves are provided by UFC 3-340-02 (DoD 2008c) in Chapter 4-55. Experimental tests comprised of a cylindrical charge in contact with the ground, oriented side-on at a prescribed stand-off distance from a wall as shown Figure 79. Various contact charges with spherical and hemispherical shape were also tested, as consequence an empirically derived spall threshold curve (Eq. Equation 36) and breach threshold curve (Eq. Equation 37) were developed as functions of the ratio h/R and the spall parameter ψ.

www.manaraa.com

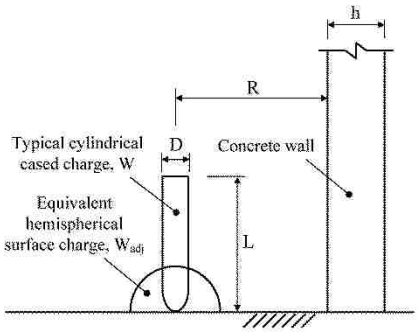

Figure 79: Typical geometry for spall and/ breach predictions

$$\frac{h}{R} = \frac{1}{a + b\psi^{2.5} + c\psi^{0.5}} \qquad \text{Equation 36}$$

$$\frac{h}{R} = \frac{1}{a + b\psi + c\psi^{2}} \qquad \text{Equation 37}$$

Where a, b and c are constants per UFC 3-340-02 (DoD 2008c) listed in Table 14; and the spall parameter ψ is a function of both the stand-off and contact charges, as given in Eq. Equation 38 for non-contact and Eq. Equation 39 for contact detonations.

Table 14: Spall and breach threshold curve constants

Constant	Spall	Breach
a	-0.02511	0.028205
b	0.01004	0.144308
c	0.13613	0.049265

$$\psi = R^{0.926} f_c'^{0.266} W_{adj}^{-0.353} \left(\frac{W_{adj}}{W_{adj} + W_c}\right)^{0.333} \qquad \text{Equation 38}$$

$$\psi = 0.527 R^{0.972} f_c'^{0.308} W_{adj}^{-0.341} \qquad \text{Equation 39}$$

Where f'_c is the concrete compressive strength expressed in psi; W_c is the steel casing weight expressed in lb_f; and W_{adj} is the adjusted charge weight expressed in lb_f. W_{adj}, given in Eq. Equation 40, is the weight of a hemispherical surface charge that applies an equal

www.manaraa.com

explosive impulse as that of the actual charge.

$$W_{adj} = B_f C_f W \qquad \text{Equation 40}$$

where W is the equivalent TNT charge weight expressed in lb_f; B_f is the burst configuration factor, equal to 1.0 for surface bursts, and to 0.5 for free air bursts; and C_f is the cylindrical charge factor given in Eq. Equation 41 and Eq. Equation 42.

$$C_f = 1 + 2 \cdot \left(\frac{L \cdot D}{\pi(3 \cdot L \cdot D^2/16)^{0.667}}\right)\left(1 - \frac{R}{2\sqrt[3]{W}}\right); \quad L > D \; and \; \frac{R}{\sqrt[3]{W}} < 2 \qquad \text{Equation 41}$$

$$C_f = 1; \quad \text{all other cases} \qquad \text{Equation 42}$$

Where L and D are the charge length (in.) and diameter (in.) respectively. A specific threat scenario provides the h/R and ψ values. Once the ratio h/R and the spall parameter ψ are known, the response of a concrete panel in terms of spall, breach, or neither can be determined. The threshold curves for spall and breach are illustrated in Figure 80. The figure is divided into three sections, each region corresponding to breach, spall, or neither (safe).

www.manaraa.com

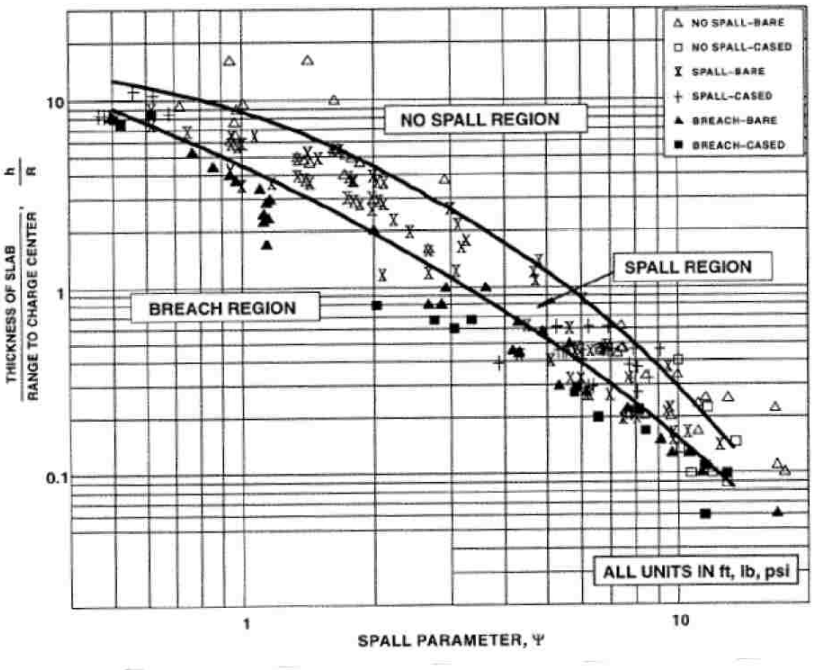

Figure 80: Spall and breach thresholds (DoD 2008c)

5.2. Spall and Breach Response of Insulated Panels

The aim of this part of the research is to assess the behavior of insulated panels subjected to close-in explosions through experimental evaluation and numerical modeling. Then, the behavior of a conventional 6 in. (152 mm) precast concrete wall is compared with the behavior of insulated wall panels. Several insulated panel configurations are considered for investigating both the influence of the foam layer and the performance sensitivity to foam thickness. Since only a localized region near the explosive charge is affected by a close-in explosion, similar to a localized impact (Ozbolt and Sharma 2011), the global behavior of the wall is not considered in this study.

5.2.1. Experimental Program

The experimental program consisted of an assessment of conventional insulated wall

www.manaraa.com

panels subjected to close-in detonations of high explosives. The explosive charge and standoff distance are the same for all the simulations, and the main goal of the study is to assess the behavior of insulated wall panels subjected to close-in detonations in comparison to the behavior of the conventional solid RC panels. As the demand is the same for all simulations and the goal is to compare the results of the various models, conclusions can be made without referring explicitly to the explosive weight. The panels are subjected to a detonation of high explosives at a stand-off distance of 5 in. (127 mm) which is estimated to produce a reflected pressure of 43,000 psi (296 MPa). All the insulated panels are comprised of an exterior and interior reinforced concrete wythe with a thickness (t_1 and t_2) of 3 in. (76 mm). The foam is varied with thicknesses (t_f) of 2 in., 4 in., and 6 in. (51, 101, 152 mm) as well as a case where two concrete panels are tested with no foam. The panels have a planar dimension of 64 in. by 64 in. (1626 x 1626 mm) and are reinforced with #4@10 in. (Φ No.13 12.7 mm diameter, spaced at 254 mm) and 6 x 6 W4.0 x W4.0 (Φ 5.7 mm diameter, spaced at 152 mm). Furthermore, a solid 6 in. thick panel is also examined and it was tested separately as part of an earlier study and therefore has a smaller planar dimension. The details for the two panel types are illustrated in Figure 81.

www.manaraa.com

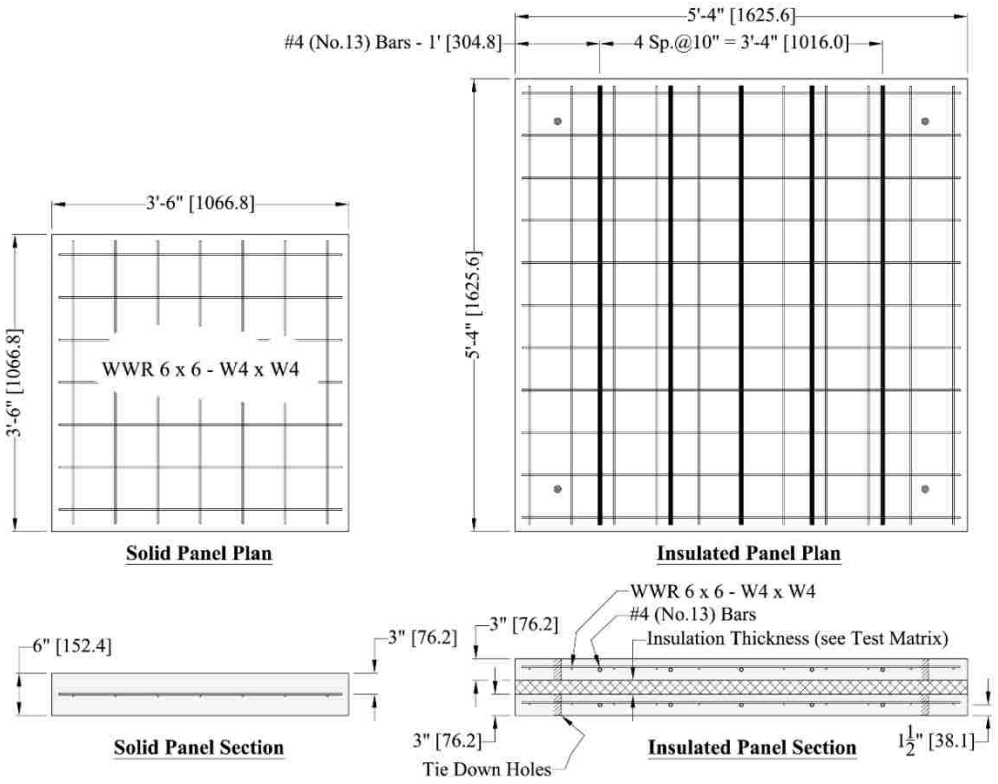

Figure 81: Plan and elevation views of tested panels

The panels represent standard construction details used by the Precast Concrete industry in the United States. The specified concrete design strength for all panels was 5000 psi (34.5 MPa); then, the concrete strength was measured in accordance with ASTM C39 (2012) within 7 days of the detonation experiments and was found to be 5560 +/- 150 psi (38.3 MPa) and 7160 +/- 110 psi (49.4 MPa) for the solid and insulated panels respectively. The bar reinforcement met the requirements of ASTM A615 (2012) Grade 60 (420 MPa) and the welded wire reinforcement (WWR) met the requirements of ASTM A1064 (2010). Yield stress for both materials is assumed to be 60 ksi (420 MPa).

The research study focused on the most economical insulation option, EPS foam. The considered EPS foam has a specific weight of 1.4 lb_f/ft^3 (220 N/m^3) (PCI 2011), elastic

www.manaraa.com

modulus of 250 psi (1.72 MPa) and Poisson's coefficient of 0.05 (Widdle et al. 2008; Masso-Moreu and Mills 2003). Wythes were connected via 0.5 in. (12.5 mm) diameter bolts 6 in. (152 mm) from each corner. Fender washers with a diameter of 3 in. (76 mm) were applied to mitigate concentrated load effects at the corners. Insulation layers were formed by stacking individual 2 in. (50 mm) thick EPS sheets to meet the prescribed foam thickness. The test matrix is summarized in Table 15.

Table 15: Test matrix

ID	Description	Thickness of exterior wythe, t_1 [in. (mm)]	Thickness of EPS insulation, t_f [in. (mm)]	Thickness of interior wythe, t_2 [in. (mm)]
6C	6 in. solid	6.0 (152)	0.0	Not Applicable
3C-0F-3C	Stacked 3 in. panels	3.0 (76)	0.0	3.0 (76)
3C-2F-3C	3 in. panels with 2 in. EPS	3.0 (76)	2.0 (51)	3.0 (76)
3C-4F-3C	3 in. panels with 4 in. EPS	3.0 (76)	4.0 (102)	3.0 (76)
3C-6F-3C	3 in. panels with 6 in. EPS	3.0 (76)	6.0 (152)	3.0 (76)

5.2.2. Empirical assessment

In Figure 82 the expected results for tested concrete panels are presented relative to the spall and breach threshold curves shown in Figure 80. The charge is assumed to be a free air blast explosion. The burst configuration factor is taken as 0.5 and the charge shape factor as 1.0 for all cases. The performance of the insulated panels is assessed with the conservative assumption that the exterior wythe and insulation are not present. For example the 3C-4F-3C is analyzed for a panel thickness, h, of 3 in. (76 mm) at a standoff distance, R, of 12 in. (305 mm). Recall that the specimens are tested with a stand-off from the exterior front face of 5 in. (127 mm). Based on the empirical formulations the solid

www.manaraa.com

panel is expected to spall and the 3C-0F-3C panel, neglecting the protection provided by the exterior wythe, is expected to breach. Using the adaption of the empirical formulas, provided by the UFC 3-340-02 (DoD 2008c), to the insulated wall panels the addition of foam layers, and consequently standoff-distance to the front of the interior wythe, results in a marginal improvement in breach resistance; however, for all cases spall is expected.

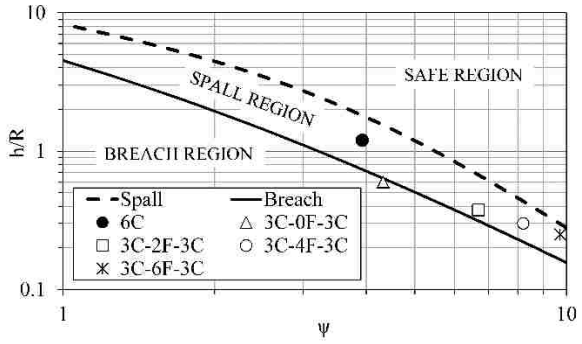

Figure 82: Spall/breach threshold curves with expected damage plotted

5.2.3. Experimental results

The results of the experimental program are summarized in this section. Each panel was subjected to one detonation as previously discussed. The results of the damage incurred on each panel are illustrated in Figure 83. Damage photos are taken for each panel face that sustained damage. In the discussion, exterior refers to the wythe on the exterior of the wall closest to the detonation while the interior refers to the wythe on the interior of the building furthest from the detonation. The face locations correlate to the designation used in Figure 83 (i.e., 1-front, 1-rear, 2-front, 2-rear). The diameter of spall was measured on each face and the breach was measured on each panel if it occurred. The effective diameter of the spall or breach was determined graphically from high-resolution images. The area of the damaged region on each image was used to determine an equivalent circular area and subsequently equivalent diameter. The results are summarized in Table 16. For cases

www.manaraa.com

where no spall or breach occurred a value of 0.0 is reported.

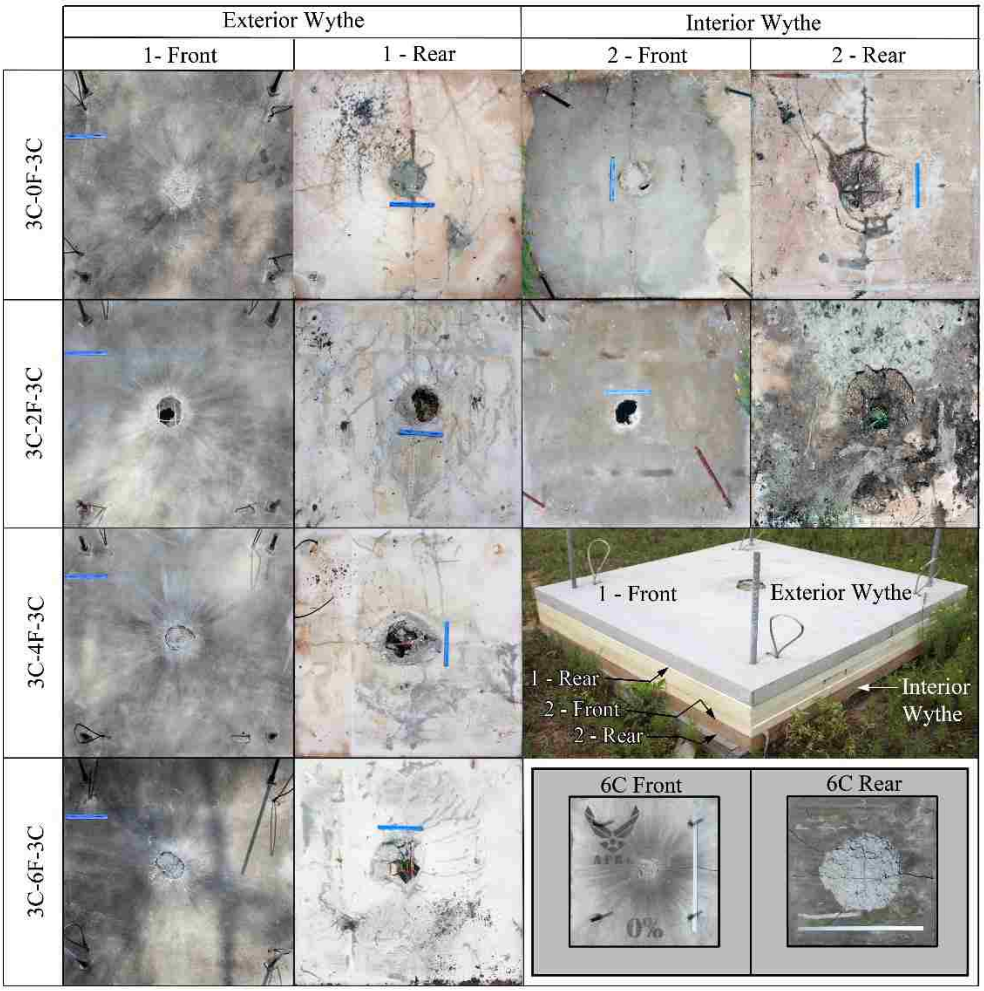

Figure 83: Damage observed from close-in detonations

www.manaraa.com

Table 16: Experimental spall and breach results

Panel	Exterior Wythe			Interior Wythe		
	1 - Front	1 - Rear	Breach Diameter [in. (mm)]	2 - Front	2 - Rear	Breach Diameter [in. (mm)]
	Spall Dia. [in. (mm)]	Spall Dia. [in. (mm)]		Spall Dia. [in. (mm)]	Spall Dia. [in. (mm)]	
3C-0F-3C	7.9 (200)	9.9 (252)	0.0	9.4 (239)	21.3 (541)	2.5 (64)
3C-2F-3C	8.3 (211)	11.7 (297)	8.3 (211)	6.3 (160)	21.1 (536)	6.3 (160)
3C-4F-3C	7.7 (196)	11.0 (279)	7.7 (196)	0.0	0.0	0.0
3C-6F-3C	7.6 (193)	15.5 (394)	7.6 (193)	0.0	0.0	0.0
6C	5.6 (142)	22.4 (569)	0.0	N.A.	N.A.	N.A.

The greatest amount of spall occurred on the solid 6 in. thick concrete panel (6C). A comparable level of damage was observed on the panel composed of two 3 in. thick concrete panels with no insulation (3C-0F-3C), however the failure mechanism changed. The damage differed in that the stacked arrangement resulted in a breach of the interior section. This interior breach however would not change the protection level since the exterior wythe was not breached and access would not be possible. The breach of the interior wythe on the stacked arrangement, however, may result in a greater quantity of ejecta than that of the 6 in. solid.

The use of insulation foam provided mixed results as the thickness of foam was increased. A small amount of insulation (3C-2F-3C) resulted in the lowest performance. A full breach of both wythes occurred on the 3C-2F-3C panels with a similar amount of interior spall diameter to that of the 6C and 3C-0F-3C panels. This indicates that small separations created by insulation may provide enough space to allow for the damage to the exterior wythe to eject and impact the interior wythe. This is further supported by comparing the damage to the exterior wythe of the 3C-0F-3C and the 3C-2F-3C panels. The damage levels are similar with the exception that no breach occurs when the exterior wythe is bearing against the hard surface of the interior concrete wythe.

www.manaraa.com

The use of a greater amount of foam on the 3C-4F-3C and the 3C-6F-3C panels resulted in a complete protection of the interior concrete wythe. For both cases, no damage was observed on either the front or rear of the interior wythe. The amount of spall on the exterior wythe remained comparable between the 3C-2F-3C and 3C-4F-3C but increased for that of the 3C-6F-3C. This may indicate that larger amounts of foam may result in less containment of the exterior wythe.

The empirical prediction of spall and breach was in line with the measured values for the solid concrete panel (6C). The spall occurred as expected (compare the 6C panel in Figure 82, Table 16 and Figure 83). Nevertheless, utilizing the empirical formulation assuming that the exterior wythe is not present is not accurate. The stacked 3C-0F-3C was expected to have a breach; however, only spall was present. The 3C-2F-3C was expected to have spall however a breach occurred and the larger foam thicknesses was expected to produce spall but no damage was observed. Based on these observations it is clear that the mechanics of the shockwave propagation through insulated panels is complex and consequently a numerical evaluation is required.

5.2.4. Numerical model

Numerical analyses are carried out in order to both design the experimental tests and further investigate the response of the insulated wall panels subjected to close-in detonations. The numerical investigation is valid for all three types of insulated wall panels (non-composite, composite, and partially-composite) as the shear connectors, which provide coupling between the two concrete layers, are significant for the global response of the insulated panel (Naito et al. 2011a). For the analyses performed, only the local effect of the insulation is of concern, the ties (Naito et al. 2012) are therefore not included.

Several studies have focused on high load demands on slabs and/or protective metal plates.

www.manaraa.com

The research indicates that numerical simulations can accurately predict the response of structures loaded by both close-in detonations (Zhou et al. 2008) and impact loads (Flores-Johnson et al. 2011).

Zhou et al. (2008) conducted numerical and experimental studies on concrete slabs, comprised of conventional and steel fiber reinforced concrete, subjected to two consecutive detonations. Furthermore, Zhou et al. (2008) adopted a damage model for the concrete using the erosion algorithm (LSTC 2012a) in order to model the fracture in the concrete. A similar set of numerical methods was conducted by Flores-Johnson et al. (2011) who presented an investigation on the ballistic performance of monolithic, double- and triple-layered metallic plates. Finite element models, examining high rate loading effects, are further validated by the experimental works of Børvik et al. (2009) and Forrestal et al. (2010), and many of the physical characteristics of the penetration process observed experimentally were numerically reproduced, allowing for a reduction in the number of experiments required.

Furthermore, about the study of high load demands on structures, analytical formulations were developed in order to both estimate the damage of concrete pavement slabs under close-in explosions (Luccioni and Luege 2006) and the penetration of projectiles into concrete panels (Li et al. 2005). Several experimental tests were also carried out in order to assess the behavior of panels fabricated with various types of concrete under close-in detonations (Ohkubo et al. 2008). Concerning the study developed in this paper, a comparable effort was made by Yamaguchi et al. (2011) on the use of thin shock absorbing materials for using between concrete panels. The results of their work indicated that the adoption of thin layers of foam and rubber does not improve the resistance to the spall. The examined thickness however, was 15 mm, much lower than insulation thicknesses

www.manaraa.com

used in conventional construction in the United States.

Many numerical solution techniques can be utilized for this evaluations including the "Lagrangian", "Eulerian", "Eulerian-Lagrangian" methods (Bontempi and Faravelli 1998; LSTC 2012b), and the "Smoothed Particle Hydrodynamics" method (LSTC 2012b;Manenti et al. 2012). Furthermore, two methods exist to take into account the interaction between the shock wave and the structural component: the coupled and the uncoupled approach (NCHRP 2010). In this study the "Lagrangian" method and the un-coupled approach are utilized (Davidson et al. 2005) in order to reduce the computational effort, the blast load is computed and applied independently from the fluid-structural interaction between the insulated panel and the shock wave. Consequently, the Load Blast Enhanced keyword (LSTC 2012a) is used to provide the blast load demand (Coughlin et al. 2010); thus the blast pressure is computed and applied in each finite element face belonging to the defined load surface giving the proper non uniform distribution of pressures on the insulated panel.

The finite element models have constant solid stress elements for modeling the concrete and foam materials, and truss elements for modeling the reinforcement (LSTC 2012a). To bond the truss and solid elements, the LS-DYNA keyword Constrained Lagrange in Solid is used.

The material model of the reinforcement is provided by the kinematic hardening plasticity model (Chen and Hao 2012). This is an elastic-plastic material model with a bilinear stress-strain curve and strain rate dependency; thus after the yield a plastic modulus is provided and the plastic stresses increase linearly until the ultimate plastic deformation is reached leading to the erosion of the finite element without dependence on the triaxiality. The rate dependence is taken into account by the Cowper-Symonds exponential strain rate

www.manaraa.com

model (LSTC 2012a; Cowper and Symond 1957; Su et al. 1995), and the parameters required for this model are C= 500 1/sec, and p=6 (Su et al. 1995).

The adoption of an appropriate constitutive model for the concrete (Bontempi and Malerba 1997) is imperative to accurately model the response of concrete structures under close-in explosions. In this study, the Karagozian & Case (K&C) Concrete Damage Model (Malvar et al. 1997), Material 72R3, with automated parameter generation (LSTC 2012a) was selected for modeling the concrete. The K&C concrete model is a damage plasticity model that decouples the failure criteria for the hydrostatic and deviatoric part of the stress tensor taking also into account the increased strength of the material due to the strain velocity by a user defined dynamic increase factor for both tension and compression stresses. For the hydrostatic regime an equation of state is assigned, while for the deviatoric stresses three failure surfaces are considered: the yield, the maximum, and the residual failure surface; furthermore, the stresses and the failure surfaces are then defined in the space of the three invariants, see Chen (1982). When the stresses reach the yield the failure surface moves as a function of the damage parameter which is dependent on the accumulated plastic deformations. Therefore, the actual failure surface moves from the yield to the maximum surface modeling the hardening of the concrete, and moves from the maximum to the residual surface modeling the softening of the concrete. As mentioned, more details on the material model are in the original paper of Malvar et al. (1997).

The implementation of the strain-rate effects in the concrete model is also crucial to properly simulate the behavior of concrete wall panels subjected to impulsive loads (Xu and Lu 2006). In fact, the concrete has different strain-rate effects in tension and compression; furthermore, the hydrostatic component of the stress tensor is important for the concrete behavior (Li et al. 2005), which complicates the experimental assessment of

www.manaraa.com

the strain-rate effects (Grote et al. 2001). The results of numerical simulations are influenced by the strain-rate dependence and several strain-rate curves are proposed in the literature: Li et al. (2005); Grote et al. (2001); CEB (1993); Tedesco et al. (1997). However, the research by Williams and Williamson (2011) suggested that the compressive dynamic increase factor for the concrete constitutive model are not necessary because the finite element models are able to capture the strain-rate effect by the inertia confinement only. In this paper the strain-rate curves developed experimentally by Tedesco (1997) are adopted for the numerical models neglecting the compressive dynamic increase factor over the strain rate of 63.1 sec^{-1}; Figure 84 shows the dynamic increase factor as presented in Tedesco et al. (1997).

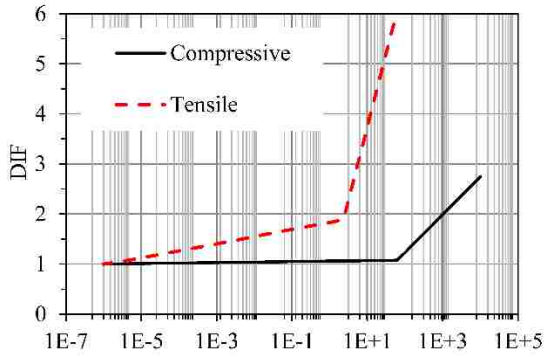

Figure 84: Dynamic Increase Factor (DIF) versus strain-rate for concrete

The foam is modeled using the Modified Crushable Foam (LSTC 2012a), Material Type 63. The disadvantage of this material model is the elastic unloading; however, since the study is focused on the max inbound effects the unloading is not critical to the analysis. The foam constitutive law is characterized by the stress versus volumetric strain curves for each strain-rate deformation regime.

The stress versus volumetric strain relationship of the EPS foam is taken from comparative experimental tests conducted on different foam types by Croop and Lobol (2009). The

www.manaraa.com

values are obtained for the insulating foam at many load rates and the stress axis is normalized by the static yield stress. Data on the yielding stress of EPS foam is taken from PCI recommendations (PCI 2011), from which the stress versus volumetric strain chart is obtained via the previously derived normalized chart. This approach assumes that the two foams have approximately the same chemical and morphologic characteristics, resulting in the same behavior at high load rate. The two foams have only a different specific weight, a parameter which mainly influences the foam resistance (Di Landro et al. 2002). Table 17 and Figure 85 summarize the foam characteristics used.

Table 17: Assumed physical properties of the EPS insulating foam

Property	Imperial	SI
Density	1.4 lbf/ft^3	220 N/m^3
Water absorption	< 3 %	< 3 %
Compressive strength	15 psi	103 kPa
Tensile strength	25 psi	172 kPa
Linear coefficient of expansion	40x10^6 / °F	72x10^6 / °C
Shear strength	35 psi	241 kPa
Flexural strength	40 psi	276 kPa
Thermal conductivity	0.26 Btu-in./hr/ft^2/°F	0.037 W-m/m^2/°C
Maximum use temperature	165 °F	74 °C

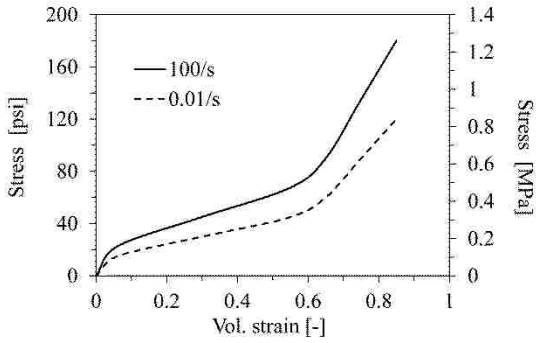

Figure 85: Stress vs. volumetric strain chart of the used EPS foam

In order to capture the interaction between the two concrete wythes the LS-DYNA Contact

www.manaraa.com

Eroding Single Surface parameter was used. Furthermore, in order to avoid both numerical instability and excessively short time steps ($\Delta t < 10^{-7}$ second), the foam is allowed to erode through the use of the LS-DYNA Mat Add Erosion. At a volumetric strain of 1.0 the insulation foam undergoes numeric instability. To prevent this instability from occurring over one time step the erosion criterion is based on the volumetric strain in the foam reaching a value of 0.95.

5.2.5. Numerical Results

Figure 86 illustrates the predicted concrete damage patterns on the front of the exterior wythe, the rear of the interior wythe, and on a section view respectively. The damage parameter of the concrete model has been used in order to illustrate both the cracking and the spall patterns on the concrete wythes, mainly because the damage parameter is cumulative so no time dependent. The threshold values for evaluating the failure of the concrete were adopted from Wang et al. (2008) and used to capture the failure of the concrete; thus the failure patterns in Figure 86 are illustrated using the damage parameter fringe level from 1.95 to 2.

www.manaraa.com

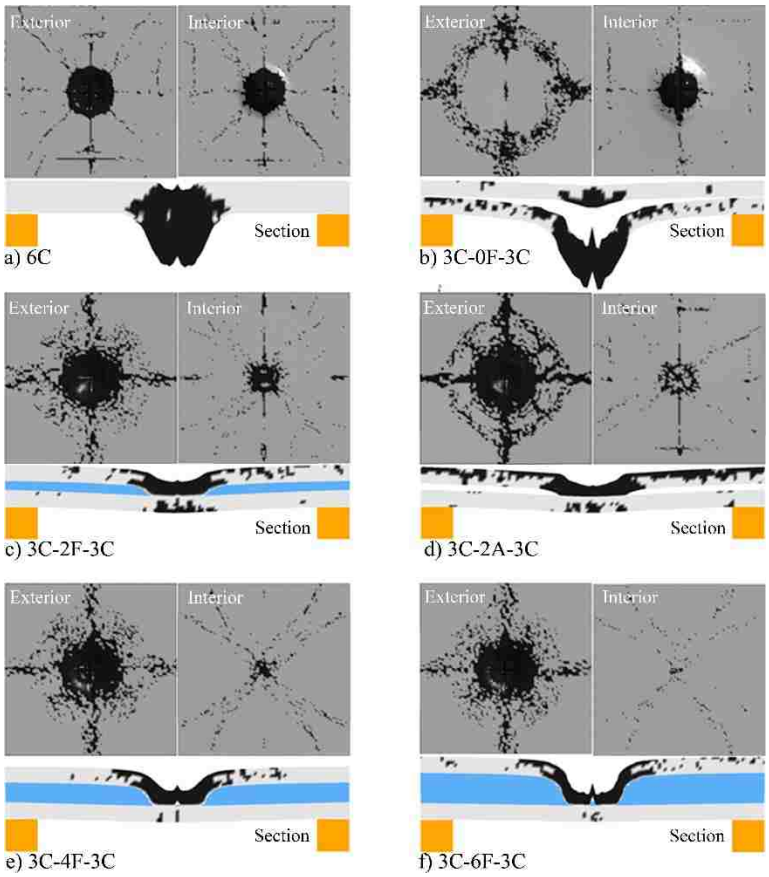

Figure 86: Numerical spall and breach results for damage parameter from 1.95 to 2.00

As illustrated in Figure 86, the numerical analysis provides a sufficiently accurate estimation of the insulated wall panels' behavior. The occurrence of spall and breach on the panels is the same as the experiment. The solid panel and the 3C-2F-3C panel resulted in breach while the 3C-4F-3C and 3C-6F-3C panels had damage only on the exterior wythe. The stacked panel 3C-0F-3C resulted in damage primarily to the interior wythe.

The predicted spall diameter on the rear face of the internal wythe is compared with the experimental data in Figure 87. The horizontal axis denotes the insulated wall panel under investigation (with the amount of foam increasing from left to right), while the vertical axis is the spall diameter (in the rear face of the interior wythe). As mentioned previously the

www.manaraa.com

spall diameter is measured by the plot of the damage parameter; furthermore, two ranges of the damage parameters are considered in order to provide a minimum and a maximum threshold for the predicted spall diameter. The minimum value is assessed by the plot of the primary damage into the concrete, while the maximum value is assessed by the plot of the primary plus the secondary damage into the concrete. The primary and secondary damage are represented by the damage parameter in the range from 1.95 to 2 and from 1.8 to 1.95 respectively (Wang et al. 2008). The numerical model matches the response of the insulated panels; however, the stacked and solid panels are marginally under-predicted.

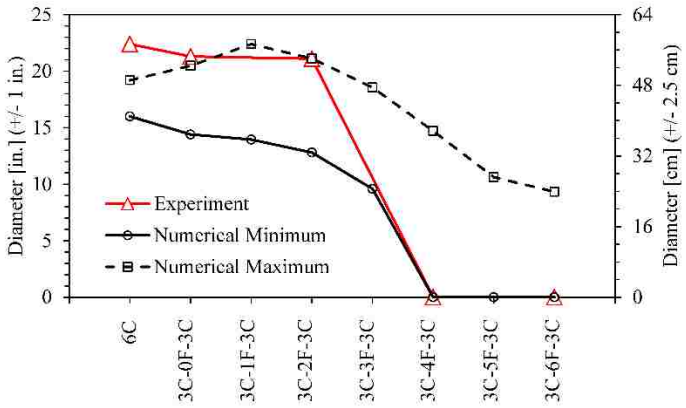

Figure 87: Measured and predicted spall diameter on protected face (rear face of the interior wythe)

The mechanism of damage of the interior wythe can be characterized by the impact of the concrete debris of the exterior wythe on the front of the interior wythe. For the blast demand examined, the exterior 3 in. (76 mm) thick wythe spalls for all foam thicknesses; consequently, when the concrete spalls the debris impacts the interior wythe. The impact force is measured in the numerical model over a 4 in. (102 mm) diameter region on the center of the 2-front surface by the means of a circular control section in the finite element models, and the force demand is illustrated in Figure 88. The impact force decreases

www.manaraa.com

considerably as the foam thickness increases from the base level of 2 in. (51mm) to the insulated wall panel with 6 in. (152 mm) of foam.

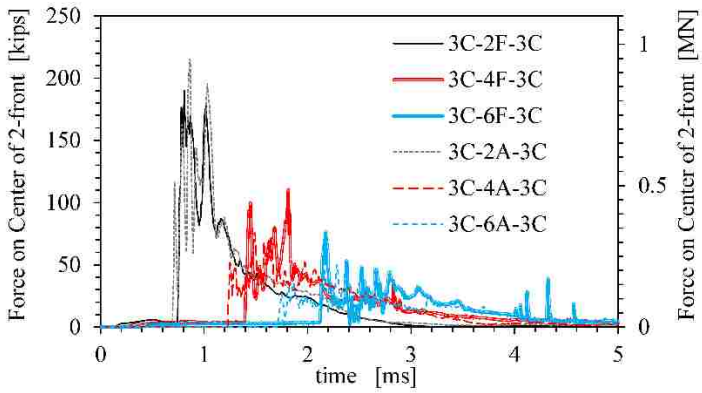

Figure 88: Impact force demand on the front face of the interior wythe

The numerical simulations are also used to investigate the effect of the insulation material on the resistance of the insulated wall panel to spall and breach. The use of air over that of three foam types (A, B and C) is examined. The foam A is the material used in the experimental investigation. As mentioned, this material has a density of 1.4 lb_f/ft^3 (22.4 kg/m^3), a compressive strength of 15 psi (103 kPa) and represents the medium grade of EPS foam (PCI 2011). Foam B represents denser EPS foam and has a density of 1.8 lb_f/ft^3 (28.8 kg/m^3) and a compressive strength of 25 psi (172 kPa). Foam C represents XPS with a density of 1.8 lb_f/ft^3 (the same as Foam B) and a compressive strength of 40 psi (276 kPa).

The results of the parametric numerical analyses are summarized in Figure 89. As illustrated, the damage to the interior wythe of the insulated wall panels increases as the density of the foam increases. Air provides the best defense against the transfer of the demand from the exterior wythe while dense and strong XPS foam provides the lowest resistance to damage. Evidently, the air provides improved resistance by spreading the

www.manaraa.com

damage over a larger portion of the exterior wythe. This is illustrated in a comparison of the fringe plots for the 2 in of air (3C-2F-3C) versus 2 in of foam A (3C-2A-3C) panels in Figure 86.

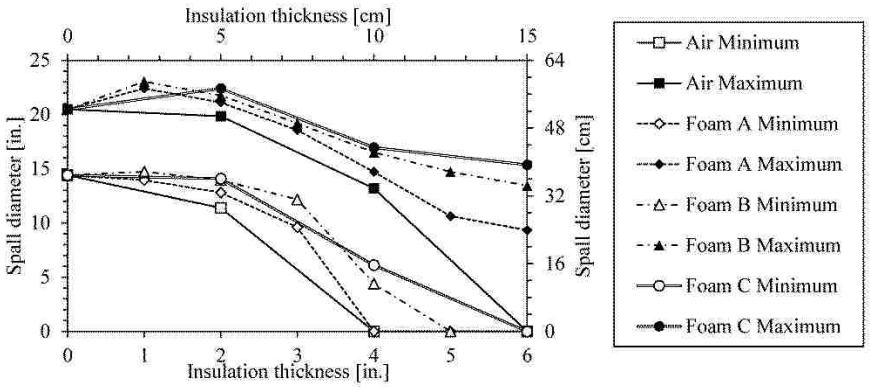

Figure 89: Parametric examination of insulation type and thickness for spall

5.2.6. Spall and Breach Response of Insulated Panels Conclusions

A research program was conducted to assess the viability of insulated reinforced concrete wall panels in mitigating spall and breach from close-in detonation of high explosives. The performance was assessed relative to experimental tests, existing empirical formulations, and numerical analyses. The experimental tests were conducted on full scale panels built in accordance with the standard practice of the United States Precast/Prestressed Concrete Industry. The panels consisted of conventional geometries and included an internal and external concrete wythe 3 in. (76 mm) thick and EPS insulation varying from 0 to 6 in. (152 mm). The empirical formulations developed by the DoD (2008) were used as a basis of comparison. The numerical simulations were conducted using LS-DYNA finite elements program (LSTC 2012a). The following conclusions are drawn from the results presented:

www.manaraa.com

- The solid 6 in. concrete panel (6C panel) and the panel composed of two stacked 3 in. wythes (3C-0F-3C panel) provide a comparable level of resistance to close-in detonations. The mechanism of failure however is altered in that the stacked panel prevents the occurrence of a complete breach with minimal damage on the exterior wythe and breach only on the interior wythe.

- The use of EPS insulation foam resulted in mixed performance as a function of the insulation foam thickness. Small amounts of insulation, 2 in. (51 mm), resulted in a full breach (similarly as the experimental results of Yamaguchi et al. (2011)) while the case with no insulation (3C-0F-3C panel) had no breach. Greater thicknesses of insulation resulted in full protection of the interior wythe with no damage on either the front or rear face of the interior wythe.

- The empirical formulations for spall and breach matched the data for the solid panel (6C panel).

- The use of empirical formulations for predicting the spall and breach on the insulated wall panels was made by assuming that the exterior wythe was not present and the stand-off distance was increased. This approach was found to be inaccurate as it does not represent the complex behavior that occur, as the shockwave propagates through the various panel materials and the external wythe debris impacts the interior wythe.

- The numerical simulations are able to predict the occurrence of the spall and breach for insulated panels subjected to close-in detonations; the breach diameters on the rear face of the interior wythe were found to be marginally unconservative for small foam thickness but bound the response at higher thicknesses.

www.manaraa.com

- The numerical models indicate that the density and strength of the insulation foam is the main factors in transfer of demand to the interior wythe.
- The numerical models supported the experimental data and could be used to further develop semi empirical spall and breach curves for insulated wall panels subjected to close-in detonations.

In conclusion, the insulated wall panels have enhanced spall and breach performance against close-in blast demands when adequate foam thickness is used. This is due to the exterior concrete wythe acting as a sacrificial wythe, allowing the gap and foam to dissipate much of the concrete fragment kinetic energy and mitigate the incipient shockwaves from the initial shock.

www.manaraa.com

6. BALLISTIC DEMANDS

The following section outlines the current design methodology for reinforced concrete slabs subjected to ballistic and fragment demands. Additionally, a new probabilistic design approach for ballistic and fragment design to assess the probability of personnel injury is outlined with a design example.

6.1. Fragility Analysis for Ballistic Design

Reliability analysis and performance based design are becoming common practice in structural engineering as the occupant safety and building efficiency continue to become more important. The use of the fragility analysis method, which was originally developed in earthquake engineering (Cornell and Krawinkler 2000) (Luco and Cornell 2000) (Vamvatsikos and Dolsek 2011), has been expanded to other structural engineering fields including wind design (Petrini and Ciampoli 2010) and blast design (Olmati et al. 2013). The fragility analysis allows designers to quickly assess the probability of exceedance of limit states for structural components knowing the probability density function of the intensity measure. This paper develops a framework to expand the fragility analysis to the field of ballistic design allowing the designer to assess the probability of personnel injury for a given direct fire or indirect fire weapon, e.g. mortar round.

Effective structural design to resist ballistic effects such as small arms or fragmenting weapons has been a goal since weapons were developed. Approaches currently in use for ballistic design are predominantly deterministic, allowing designers to decide what wall thickness should be used in order to stop a prescribed bullet impacting at a predefined velocity. Cumulative distribution functions (CDF) have been formed in literature (Elek and Jaramaz 2009) for the mass dispersion of a fragmenting weapon, allowing a designer

www.manaraa.com

to set a confidence level for the mass of the fragment (DoD 2008c); however, no further probabilistic analysis has been considered. Current methods fall short of allowing the designer or owner to have an accurate understanding of the level of safety that is provided by a given design. To overcome this shortfall a probabilistic approach is developed that can be used in order to determine the degree of safety of a structural design against bullets and fragments. The proposed approach expands on reliability based analysis for fragmentation effects and penetration of fragments into concrete (Twisdale et al. 1993), allowing the designer to account for variability in the materials used, the construction thicknesses, the variation in the fragment size, distribution and strike velocity, and the probability of critically harming an inhabitant of the structure.

The approach is broken down into three categories: 1) Direct Fire Weapons, 2) Indirect Fire Weapons, and 3) Injury to Personnel. Category 1 introduces the concept of uncertainty in demand and capacity through stochastic variables utilized in bullet penetration equations. Category 2 expands on category 1 by introducing variables that are a function of the defined stochastic variables. Category 3 builds on category 2 by utilizing the output obtained in category 2 to determine the likelihood of personnel injury.

Each mentioned category is illustrated through numerical examples of a wall design in order to assess: a) Threat levels presented in Unified Facilities Criteria (UFC) 4-023-07 (DoD 2008a), b) Typical mortar round approximated by a fragmenting cylindrical charge, c) Critical organ damage provided in UFC 3-340-02 (DoD 2008c).

6.1.1. Models for perforation

The following sections list the threat parameters and relevant equations utilized in the performed probabilistic analysis.

www.manaraa.com

Direct Fire Weapons

The UFC 4-023-07 provides design procedures for structures subject to direct weapons fire (DOD 2008a). Four different threat levels are defined to represent the weapons that can be expected to be used on a building and personnel. These threat levels were derived from the Underwriters Laboratories Standard for Safety (UL 752) (UL 2005). The mentioned four threat levels are defined by the mass, impact velocity, size and shape of the ammunition. The parameters of interest for the purpose of this study are shown in Table 18; in particular the Underwriters Laboratories provides the nose performance coefficient, *N*, for the prescribed ammunition. Alternatively *N* can be calculated as the summation of 0.72 and a quarter of the quotient of the projectile nose length and diameter (DoD 2008a). Bullet mass is commonly calculated in grains, thus for consistency, bullet and fragment mass will be referred to in grains (15.43grain = 1g).

Table 18: Direct fire weapons threat parameters (DoD 2008a) (UL 2005)

Design Basis Threat	UL 752 Level	N	Mass (grain)	Strike Velocity (m/s)	Diameter (mm)
Very High	10	1.31	709.5	856-942	12.95
High	9	1.39	166	828-910	7.82
Medium	5	1.26	150	838-922	7.82
Low	3	0.91	240	411-453	11.18

Note: "N" is the nose performance coefficient

The maximum penetration into an air backed concrete wall (mm) is empirically provided in Equation 43 where *d* is the projectile diameter (mm), *m* is the projectile mass (kg), *c* is the maximum gravel size in concrete (mm) (assumed to be 19mm for most concrete (DoD 2008a)), v_s is the strike velocity (m/s), f_c is the concrete compression strength (MPa), and f_{age} is the concrete age factor (taken to be 1). Equation 43 is then utilized to determine the thickness required (mm) in order to prevent perforation, T_{PL}, in the empirically formed Equation 44 which can be used to calculate the residual velocity, v_r, of the projectile (m/s) in Equation 45 where *t* is the actual wall thickness (mm) of the panel.

www.manaraa.com

$$P_c = \frac{56.6\left({}^{m}/_{d^3}\right)^{0.075} N m {v_s}^{1.8}}{\frac{d^2\sqrt{f_c}}{+\,d}}\left({}^{d}/_{c}\right)^{0.15} f_{age} \qquad \text{Equation 43}$$

$$T_{PL} = D\left[1.239\left({}^{P_c}/_{d}\right) + 1.132\right] \qquad \text{Equation 44}$$

$$v_r = v_s\left(1 - \frac{{}^{t}/_{D}}{{}^{T_{PL}}/_{D}}\right)^{0.733} \qquad \text{Equation 45}$$

Indirect Fire Weapons

Upon detonation of a mortar, fragments are generated both from the mortar casing, termed "primary fragments", and from objects that interact with the blast wave generated from the detonation, termed "secondary fragments". In this paper, only "primary fragments" will be discussed and thus the name is shortened to fragment for convenience. Table 19 provides three different threat levels for indirect fire weapons. Unlike the direct fire threat parameters given in Table 18, the indirect fire weapon threat levels are defined relative to the protection provided and the proximity of the detonation; consequently the size of the fragmenting munition is dependent on the needs of the owner.

Table 19: Indirect fire weapons threat parameters 41

Design Basis Threat	Impact Distance (m)
High	Near Contact
Medium	2
Low	5

Once the mortar casing ruptures, a large number of fragments are generated which are assumed to all project with the same initial velocity. The most prevalent technique to determine the initial velocity, v_o (fps), is the Gurney method (Gurney 1943)(DoD 2012)

www.manaraa.com

shown in Equation 46 (DoD 2008c); which is only valid for cylindrical cylinders uniformly packed with explosive, W (lbf) is the charge weight, W_c (lbf) is the weight of the casing (the mortar in this case) and $(2E')^{1/2}$ (fps) is the Gurney Energy Constant dependent on the explosive type. Although it is assumed that all fragments have the same initial velocity, the strike velocities will differ as it is a function of the fragment mass, drag, and standoff distance. Note that the equations in this section were developed for English units; however, the results have been converted to SI units.

$$v_o = (2E')^{1/2}\left(\frac{W/W_c}{1+0.5W/W_c}\right)^{1/2} \qquad \text{Equation 46}$$

Numerous CDFs have been developed for the mass dispersion of fragments (Elek and Jaramaz 2009). CDFs give the probability that a stochastic variable "X", with a proper probability density function, is equal to or less than a value (x). One of the most popular and proven distributions is the Generalized Mott Distribution, shown in Equation 47 ((Elek and Jaramaz 2009) where $N_T(m)$ is the number of fragments greater than mass m, μ is the mean mass, and λ is an exponent depending on the thickness of the casing. The Generalized Mott Distribution is formulated based on three-dimensional fragmentation geometric statistics. For thin-walled steel casings, a value of ½ was found to be adequate (Arnold and Rottenkolber 2008)(Gurney 1943).

$$N_T(m) = exp\left[-\left(m/\mu\right)^{\lambda}\right] \qquad \text{Equation 47}$$

The mean fragment mass is taken to be M_A^2 where M_A ($oz^{1/2}$) is the fragment distribution factor provided in Equation 48 (DoD 2008c). The fragment distribution factor is a function of the casing thickness t_c (in), the mean inner casing diameter d_i (in) and an explosive

www.manaraa.com

constant, B ($oz^{1/2}in^{-7/6}$), dependent on the explosive type.

$$M_A = Bt_c^{5/6} d_i^{1/3} \left(1 + {}^{t_c}/_{d_i}\right) \qquad \text{Equation 48}$$

In order to determine the fragment diameter, a fragment shape as shown in Figure 90 is assumed. The caliber density, D (lb/in^3), which is equal to the quotient of the fragment mass and the cube of the fragment diameter, is taken to be 0.079 grain/mm^3. This defines a typical fragment shape of chunky geometry (DoD 2008c).

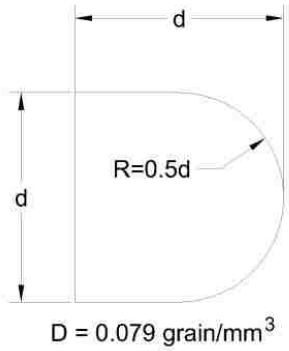

Figure 90: Standard fragment shape (DoD 2008c)

Many equations exist to calculate the penetration of a bullet or other designed projectile into concrete; however, there are relatively few equations available for fragment penetration in particular. The Modified National Defense Research Committee formula (NDRC 1946)(Arnold and Rottenkolber 2008), originally derived by Beth (Beth 1946)(NDRC 1946), was chosen because it agrees with the largest range of experimental test data (Kennedy 1975)(Beth 1946)(Yankelevsky 1997), it is based on a theory of penetration with empirically determined coefficients allowing it to be extrapolated beyond the range of available test data with greater confidence (Kennedy 1975)(Beth 1946), it is one of the most representative equations in use (Li et al. 2005)(Yankelevsk 1997), and it is

www.manaraa.com

one of the only equations aside from the Amman and Whitney Formula (Kennedy 1975)(Beth 1946) available for fragment penetration. Additionally, empirical formulas have been developed for spalling and perforation limits based on the NDRC equation (Li et al. 2006)(Li et al. 2005). The Modified NDRC equation is reproduced as Equation 49 where X_f (in) is the maximum penetration of an armor piercing fragment into air backed concrete with a strength of 27.6MPa, d (in) is the diameter of the fragment and v_s (fps) is the strike velocity. The penetration depth can be adjusted for various concrete and fragment strengths (DoD 2008c). Equation 50 and Equation 51 provide the minimum thicknesses of the concrete wall to prevent perforation, T_{pf} (in), and spall, T_{sp} (in) respectively. The residual velocity of a fragment that perforates the concrete wall is empirically given by Equation 52.

$$X_f = 2.86 * 10^{-3} d^{1.1} v_s^{0.9} \text{ for } X_f \leq 2d$$
$$X_f = 2.04 * 10^{-6} d^{1.2} v_s^{1.8} + d \text{ for } X_f > 2d \qquad \text{Equation 49}$$

$$T_{pf} = 1.13 X_f d^{0.1} + 1.311 d \qquad \text{Equation 50}$$

$$T_{sp} = 1.215 X_f d^{0.1} + 2.12 d \qquad \text{Equation 51}$$

$$v_r = v_s \left[1 - \left({}^{t}/_{T_{pf}}\right)^2\right]^{0.555} \text{ for } X_f \leq 2d$$
$$v_r = v_s \left[1 - \left({}^{t}/_{T_{pf}}\right)\right]^{0.555} \text{ for } X_f > 2d \qquad \text{Equation 52}$$

While no methods exist for calculating the probability of obtaining a penetration depth given a bullet impact, a method has been established for fragment strikes. A confidence level, C_L, as defined by (DoD 2008c) can be chosen to limit the design mass of the

www.manaraa.com

fragment as given in Equation 53.

$$m = M_A^2 ln^2(1 - C_L) \qquad \text{Equation 53}$$

The C_L is a one-sided confidence limit, giving the lower critical value of the CDF. For example, the engineer would select a C_L of 0.9 in order to design for a fragment that is 90% heavier than all the other fragments produced during the detonation. Unfortunately, the method provided in (DoD 2008c) does not account for the fragment trajectory. The method presented in this paper serves as a suitable probabilistic approach that allows the designer to determine the probability of a fragment to strike a target and assess the probability of injury to personnel.

Injury to Personnel

Human organ tolerance levels have been established for four critical organs as defined in (DoD 2008c): thorax, abdomen, limbs, and head. Table 20 provides the threshold limit of each critical organ in terms of fragment mass and velocity. Intuitively, a fragment with a smaller mass must travel faster in order to cause bodily harm. Note that the threshold limit for each organ is not at a constant kinetic energy limit.

Table 20: Threshold of serious injury due to fragment impact (DoD 2008c)

Critical Organ	Mass [grain]	Velocity [m/s]
Thorax	>17500	3.1
	700	24.4
	7	121.9
Abdomen and limbs	>42000	3.1
	700	22.9
	7	167.6
Head	>56000	3.1
	700	30.5
	7	137.2

www.manaraa.com

6.1.2. Theory and Calculation

The following sections provide the distributions, mean values, and coefficients of variation utilized in the probabilistic analysis. The number of samples, *n*, was selected to be 100,000 for each input variable. Each group of random samples comprising the input variable was generated from a prescribed probability density distribution. The input variable is a variable which is independent of all other variables, while variables that depend on input variables are referred to as intermediary variables. To develop the distribution of an intermediary variable, Monte Carlo simulations were conducted utilizing the equations provided in the "Models for perforation" section. The Monte Carlo simulation assesses the probability of a certain event occurring through the repetition of a large number of deterministic experiments. In general, the Monte Carlo simulation is performed in four tasks as shown in Figure 91:

1. Statistic characterization of the random variables,

2. Generation of the samples from the prescribed probability density functions,

3. Solution of the deterministic problem for each set of inputs to compute a set of outputs,

4. Post-processing and statistical analysis of the results in order to obtain the probabilistic characteristics of the output variables.

Figure 91 generally depicts how the Monte Carlo process was utilized for the direct fire weapons, indirect fire weapons, and injury to personnel sections.

In contrast to the Monte Carlo simulation, the confidence level method is unable to account for variations in input and thus intermediary variables as shown in Figure 91. The confidence level approach allows the engineer to design for one specific fragment mass,

www.manaraa.com

determined based on the corresponding mass value determined from the Mott Distribution from the confidence level selected, as provided in Equation 53. All other variables are considered deterministic, including the standoff distance and charge size. A probabilistic curve may be developed using the confidence level method by repeating the process and saving each calculated output value corresponding to the selected confidence level.

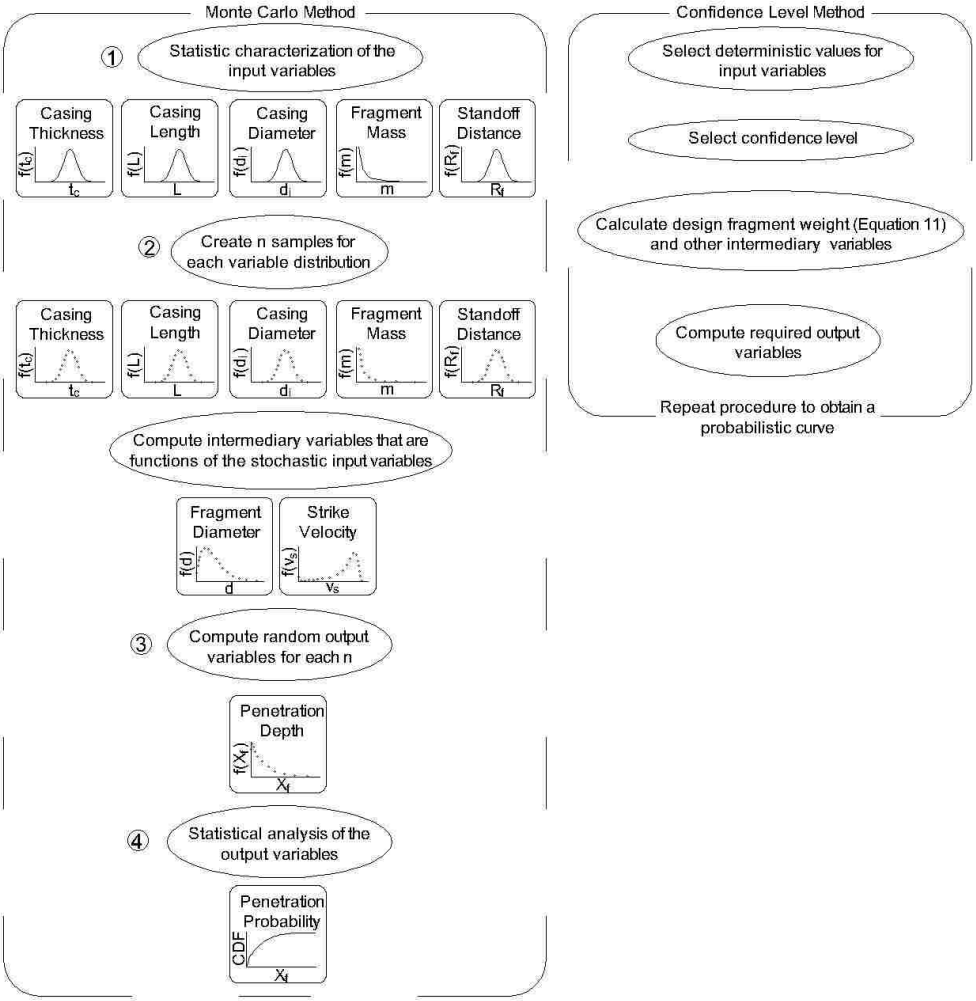

Figure 91: Monte Carlo simulation versus confidence level method

Direct Fire Weapons

The bullet mean velocity for each threat level was taken to be the mean between the

www.manaraa.com

maximum and minimum velocities for each threat level provided in Table 18. The Coefficient of variation (COV), defined as the quotient of the standard deviation and the mean value of the distribution, was selected in order to obtain such that the number of bullets with a velocity outside of the range provided in Table 18 was less than 1% of the total number of samples.

For security reasons, data available on ballistic demands and performance is limited distribution to the public. As a consequence, the distribution for strike velocity shown in Figure 93 was assumed to be lognormal, as the lognormal distribution is useful especially when the values of the stochastic variables are strictly positive (Ang and Tang 2007). Confidential documents should be consulted to apply a more realistic distribution and improve the accuracy of the results.

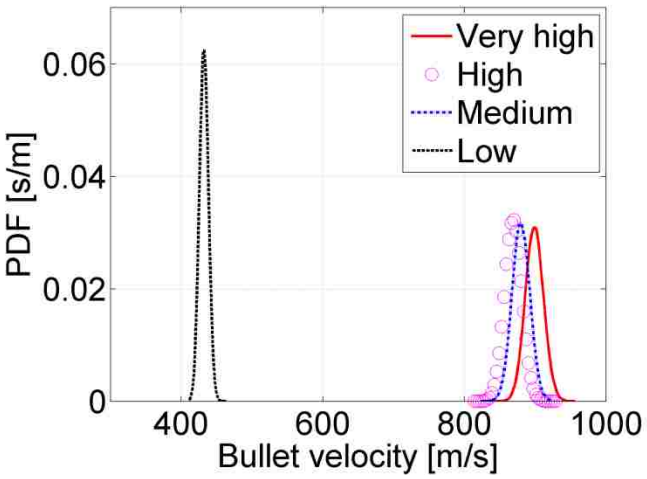

Figure 92: Strike velocity distribution

Similar to the bullet velocity, the bullet mass distribution was assumed to be lognormal with a mean value obtained from the mass expected for each bullet type used in the threat levels of Table 18. An open distribution report by the U.S. Air Force Academy found that the largest standard deviation of bullet mass from a sample of 40 boxes of ammunition

www.manaraa.com

representing seven different companies was 0.470% (Magee et al. 2012). The concrete strength was also taken as stochastic variable with lognormal distribution and a COV of 0.18 (Enright and Frangopol) as shown in Figure 94. Table 21 provides a list of the stochastic variables, all of which are lognormal, with their mean values and coefficients of variation. The nose coefficient, *N*, bullet diameter, *d*, and the concrete aggregate size, *c*, were taken as deterministic where *c* was assumed to be 19mm (DoD 2008a). In order to calculate residual velocities, a wall thickness with a mean of 152mm was assumed as provided in Table 21. The COV of the wall panel thickness was based on tolerances for precast concrete (PCI 2010b).

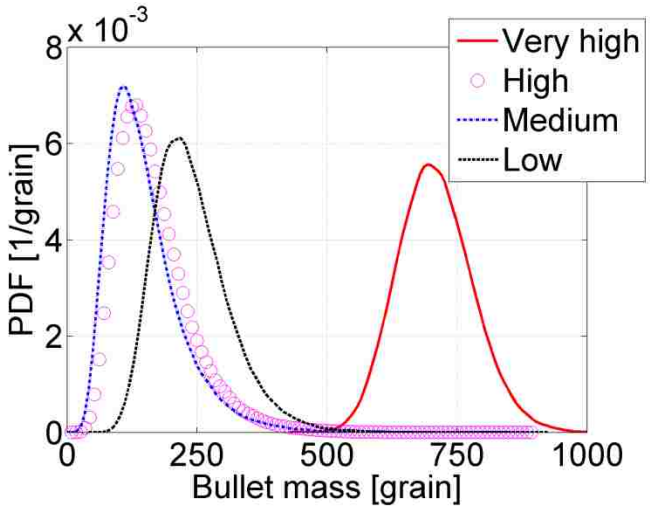

Figure 93: Mass distribution

www.manaraa.com

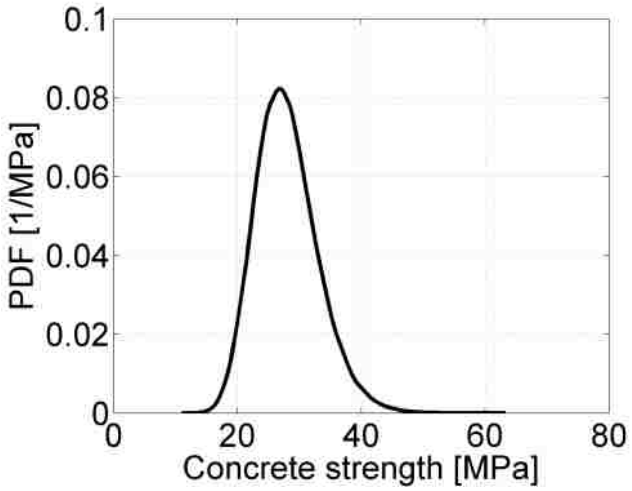

Figure 94: Concrete strength distribution

Table 21: Mean and dispersion of the Direct Fire Weapons Variables		
Variable	Mean Value	COV
Very High Threat Velocity	899 m/s	0.015
Very High Threat Mass	709.5 grain	0.102
High Threat Velocity	869 m/s	0.014
High Threat Mass	166.0 grain	0.432
Medium Threat Velocity	880 m/s	0.014
Medium Threat Mass	150.0 grain	0.488
Low Threat Velocity	432 m/s	0.015
Low Threat Mass	240.0 grain	0.300
Concrete Strength	28 MPa	0.180
Wall Thickness	152 mm	0.001

Indirect Fire Weapons

Mean values for the explosive casing thickness and inner diameter were based on a typical cylindrical explosive (DoD 2008c), while the casing length was selected based on the 81MM M821 high explosive cartridge (AOLLC 2009). Precision for manufacturing mortars was assumed to be the same as that for bullets (Magee et al. 2012), thus the same standard deviation was selected for the casing thickness, inner diameter, and length. The casing and charge mass were then determined through calculated volumes and known material densities, taking the casing material as mild steel and the explosive type as Composition B, which agreed with both the application in UFC 3-340-02 (DoD 2008c) and

www.manaraa.com

the mortar round developed by American Ordnance LLC (AOLLC 2009).

The Mott Distribution was formulated using Equation 47 and the fragment distribution factor provided in Equation 48. The CDF of the fragment mass for the Mott Distribution is shown in Figure 95, and from the relationship between the caliber density to fragment weight and diameter, the fragment diameter distribution is determined as shown in Figure 96.

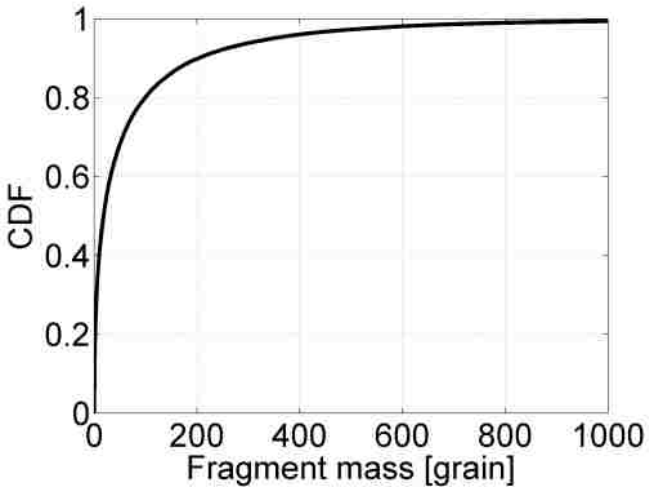

Figure 95: CDF of fragment mass

www.manaraa.com

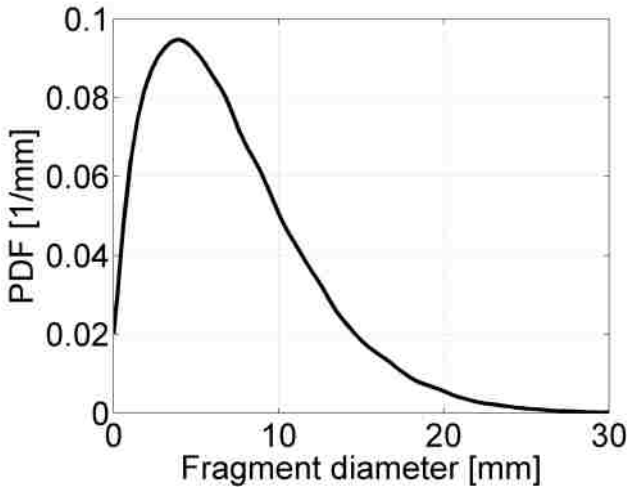

Figure 96: Fragment diameter distribution

A mean standoff distance of 12m with a lognormal distribution and COV of 0.1 was chosen. The mean standoff distance was selected based on conventional construction standoff distances for load bearing, reinforced concrete walls of a high occupancy house (DoD 2012), where the required minimum standoff distance is 26m. The standoff distance is less than that of the required minimum standoff distance because it is assumed that the assailant would be firing an explosive round over a controlled perimeter from the required minimum standoff distance. The landing point is assumed to have a high degree of uncertainty, as aggressors often fire indirect weapons from significant distances, over obstacles without a clear line of sight to the target (DoD 2008b). Thus, although the assumption that the aggressor is firing from the required minimum standoff distance may be conservative, a large coefficient of variation accounts for incompetence or firing from larger distances.

As the initial conditions (i.e. the initial velocity, v_o, a stochastic variable developed from Equation 46, and taking the initial time to be zero), forces acting on the fragment (i.e. gravity and drag), and standoff distance (stochastic variable with assumed lognormal

www.manaraa.com

distribution) are known, the trajectory and strike velocity of the fragment can be calculated. The initial launch angle, φ, for each fragment was taken as a uniformly distributed variable between -90° and 90°. Additionally, the direction of launch, θ, was taken as a uniformly distributed variable between 0° and 360°. The drag force was taken as a vector always acting in the direction opposite of motion and was determined by assuming a circular cross section using the corresponding fragment diameter from Figure 96, and calculating the instantaneous drag coefficient as a function of the velocity as shown in Figure 97 (Zaker 1975). The equation of motion was then solved numerically using an explicit time stepping method (Chopra 2007). Once the strike velocity was calculated, a histogram of the fragment strike velocity for various mass bins was plotted as shown in Figure 98. Mass bins were selected based on the mass distribution CDF, with each bin representing 25% of the total mass. The center of each histogram bar is connected by a line as shown by the "Mass < Bottom 25%" bin in order to increase the plot visibility. As shown in Figure 98, there are a large number of low mass and low velocity fragments that will not have the kinetic energy required to penetrate any protective barrier.

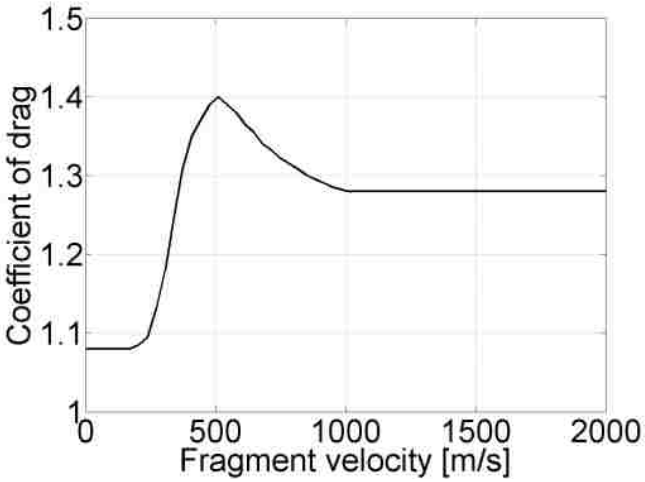

Figure 97: Drag coefficient versus fragment velocity (Zaker 1975)

www.manaraa.com

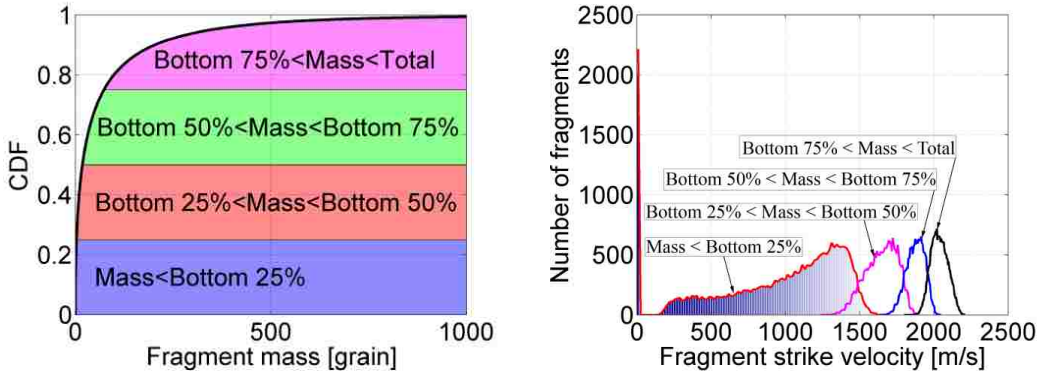

Figure 98: Histogram of fragment velocity for various mass bins

The CDF provided in Figure 95 was for every fragment generated from the ruptured mortar casing; however, only a fraction of these fragments will actually strike the wall panel, depending on the trajectory of the fragment as well as the width and height of the wall panel (Zaker 1975). Figure 99 depicts the influence of the fragment trajectory and wall area on the probability of striking the panel. The wall panel width and height are taken as stochastic variables with COVs based on tolerances for precast concrete (PCI 2010b). The mean width and height are based on standard precast concrete panel sizes currently used in industry (PCI 2010b) Considering the likelihood of the fragment striking the wall panel, a new CDF and histogram can be plotted for the fragment as shown in Figure 100 and Figure 101.

www.manaraa.com

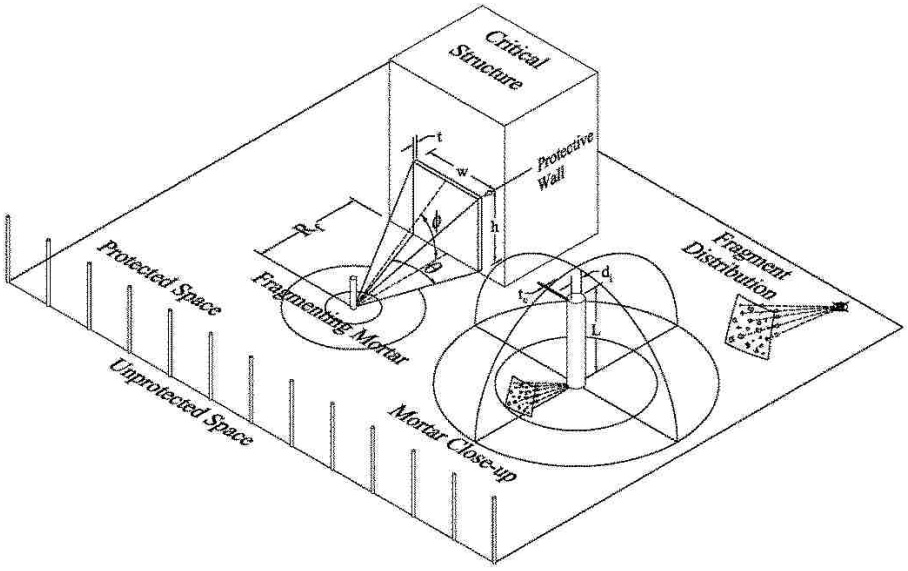

Figure 99: Variables dictating fragment trajectory

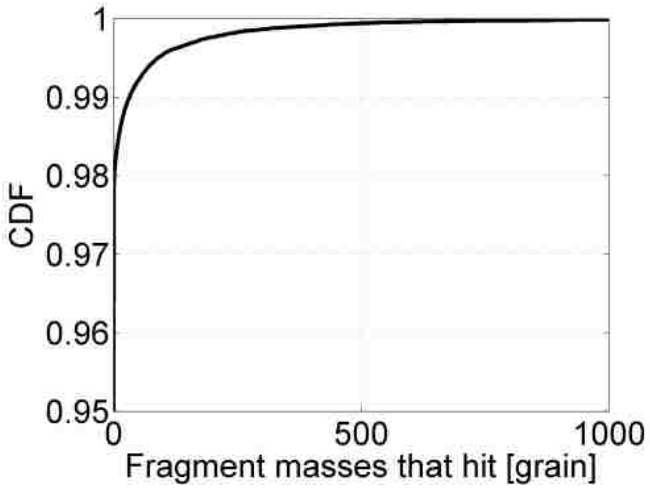

Figure 100: CDF of fragment masses that hit the target

www.manaraa.com

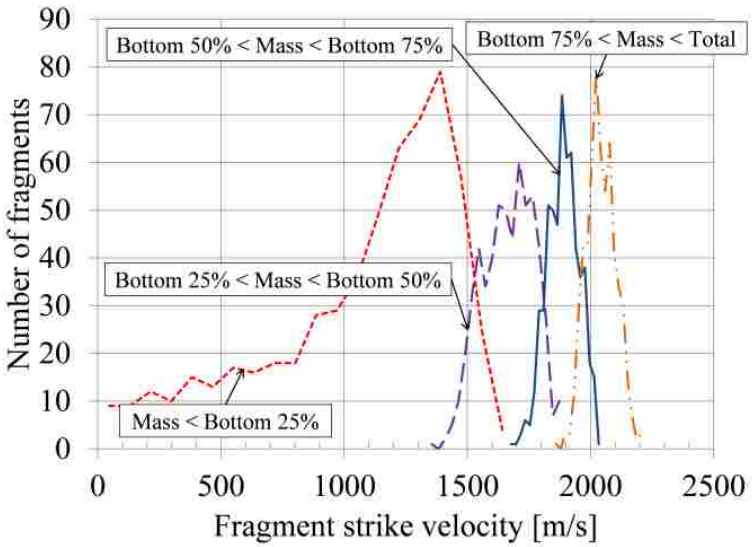

Figure 101: Histogram of fragment velocity for various mass bins for fragments that hit the target

Table 22 provides a list of the stochastic variables with their distribution type, mean values, and coefficients of variation. The concrete strength and wall thickness are the same as that utilized in the direct fire weapons analysis provided in Table 21. COVs of the weapons and structure are small with respect to the COVs of the fragments, concrete strength, and standoff distance; however, the weapons and structure are still analyzed as stochastic in the event that confidential literature indicates larger COVs.

www.manaraa.com

Table 22: Indirect Fire Weapons Analysis Stochastic Variables			
Variable	Distribution Type	Mean Value	COV
Casing Thickness	Lognormal	12.7 mm	0.0094
Casing Inner Diameter	Lognormal	304.8 mm	0.0004
Casing Length	Lognormal	609.6 mm	0.0002
Fragment Mass	Mott	75.9 grain	2.226
Standoff Distance	Lognormal	12.2 m	0.1000
Wall Width	Lognormal	12.2 m	0.0010
Wall Height	Lognormal	9.1 m	0.0010
Concrete Strength	Lognormal	28 MPa	0.1800
Wall Thickness	Lognormal	152 mm	0.0010

Injury to Personnel

The critical human organ survivability thresholds provided in Table 20 are plotted in Figure 102 below. Fragments with a mass and velocity landing in the area above any of the threshold lines represent a threat to the organ for which it lies above. To simplify the analysis, a conservative single threshold line based on the minimum of all three lines at any point was formed. Therefore, if a fragment lies above the single threshold line, it is assumed that it will cause injury to all of the critical organs as shown in Figure 102. By taking the quotient of the quantity of fragments in the injury area and the total number of fragments, the probability of injury is obtained.

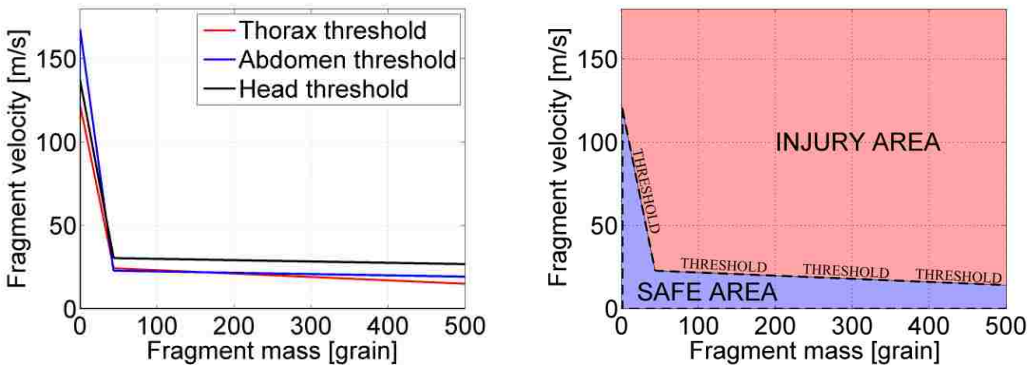

Figure 102: Critical human organ damage thresholds

Curves are developed providing the probability of injury versus wall thickness for the

www.manaraa.com

standoff distances provided in Table 19. In order to develop each curve, Monte Carlo simulations are conducted for each fragment to determine the mass and residual velocity of each of the *n* number of fragments for a given wall thickness and standoff distance, as shown in Figure 91. Thus, a single point on the probability of injury curve is calculated for each prescribed wall thickness and standoff distance. This process is repeated as shown in Figure 103 until the probability of injury versus wall thickness for each standoff distance is determined.

www.manaraa.com

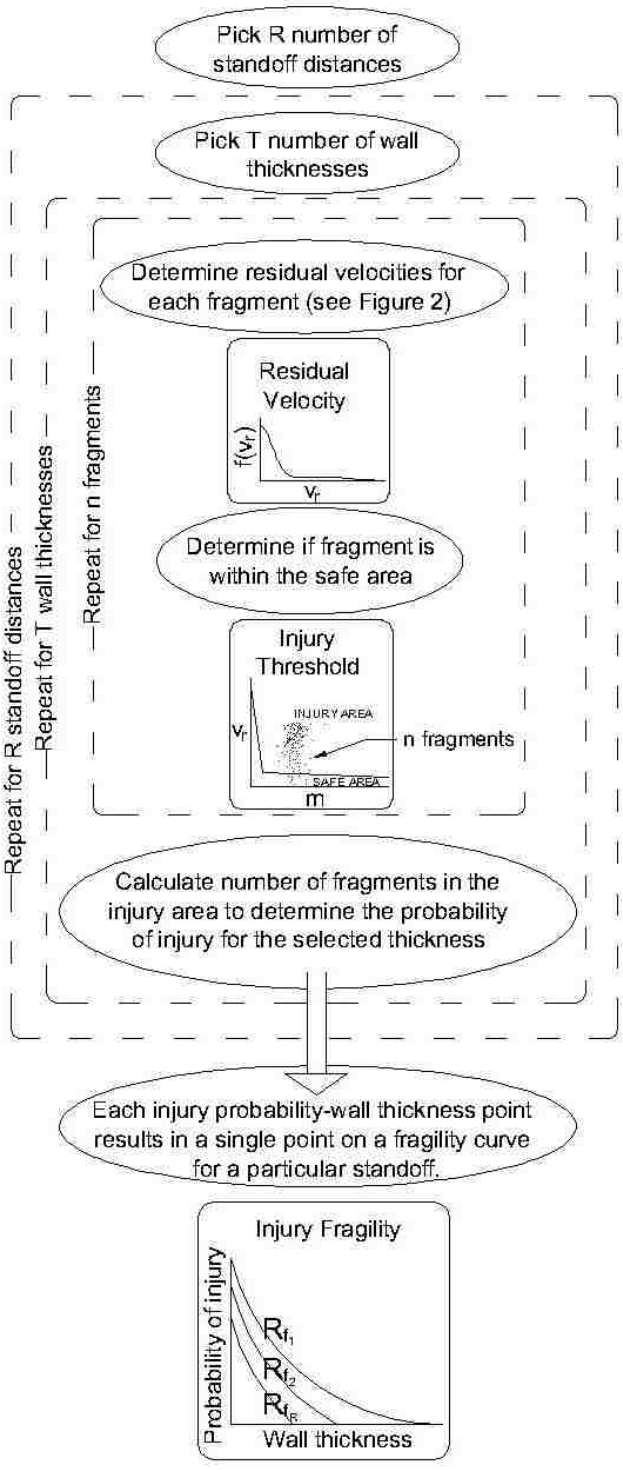

Figure 103: Schematic of the fragility curve for injury

www.manaraa.com

6.1.3. Ballistic and Fragment Results and Discussion

The following sections provide the results obtained through the Monte Carlo simulation and the intellectual merit of the study. Although the following graphs are referred to as "fragility curves" in this paper, historically, fragility curves are based on an intensity measure, an interface variable introduced in order to be able to fully represent the characteristics of the hazard in a single scalar, often, or in a vector variable, rarely. In the case of a ballistic threat, a conclusion on the opportune scalar intensity measure is not generally achieved; therefore the fragilities presented in this paper are defined as functions of the wall thickness or the residual velocity rather than the ballistic demand.

Direct Fire Weapons

Fragility curves are developed for the limit state of perforation as a function of a prescribed threat level where the wall thickness serves as the intensity measure as shown by the solid lines against the primary abscissa in Figure 104. The developed fragilities can act as a design tool for the engineer to quickly determine what wall thickness is required to achieve a particular level of safety. For example, to stop a bullet from perforating a wall 80% of the time, a 300mm thick wall would be necessary to achieve a medium threat level, while a 500mm thick wall would be necessary for a very high threat level. Additionally, the designer can use the curve to assess the probability of perforation for a given wall thickness. For example, for a 500mm thick wall, there is an 80% probability that a very high threat level will perforate the wall.

Curves are also developed for the probability of exceeding a particular residual velocity for a given wall thickness (in this case a mean wall thickness of 152mm) as shown by the dotted lines against the secondary abscissa in Figure 104. For example, it is very unlikely that the bullet corresponding to a low threat level will penetrate a 152mm thick wall with a

www.manaraa.com

residual velocity of at least 200 m/s, while there is approximately a 50% chance for a medium threat level bullet and a 100% chance for a very high threat level bullet.

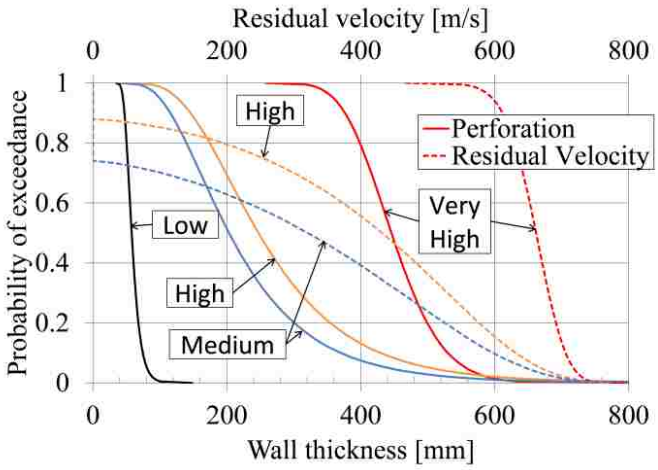

Figure 104: Probability of perforation and exceeding a given residual velocity for various threat levels

Residual velocities can also be plotted for the case of multiple wall thicknesses. Figure 105 depicts the fragility curves for a very high threat level where residual velocity is the intensity measure at four different wall thicknesses. Intuitively, a bullet is less likely to perforate a thicker wall panel with a particular minimum residual velocity. Note for the case of no wall, the residual velocity fragility is directly determined from the distribution of the strike velocity.

www.manaraa.com

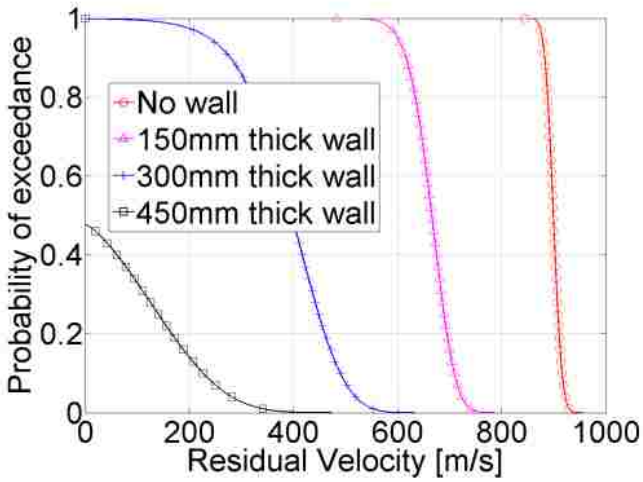

Figure 105: Probability of exceeding a given residual velocity for various wall thicknesses for a very high threat

Indirect Fire Weapons

Similar to the direct fire weapons' probabilistic analysis, the fragility of a fragment perforating a wall can be plotted with the wall thickness as the intensity measure. Figure 106 provides the probability of spall or perforation occurring for a mean standoff distance of 12m for all fragments on the primary ordinate and for fragments that strike the wall panel on the secondary ordinate. As seen by considering the fragment trajectory, even with an infinitesimally thin wall panel the probability of spall or perforation is not 100%. This is attributed to the possibility that the fragment may not strike the wall panel at all.

www.manaraa.com

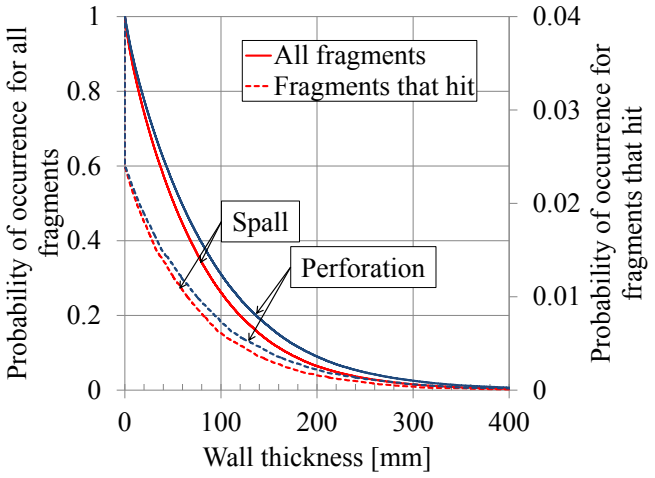

Figure 106: Fragment perforation and spall probability for a mean standoff of 12m

The Monte Carlo results were compared to the confidence level method of (DoD 2008c) by following the process laid out in Figure 91. A numerical program was developed in order to plot multiple confidence level points versus wall thicknesses. As shown in Figure 107, the fragility analysis (by Monte Carlo simulations) leads to a significant difference from the confidence level method. Differences between the confidence level method and the fragility analysis are attributed to the compounding of the many stochastic variables and the numerical determination of the fragment strike velocity which could not be implemented in the confidence level method.

www.manaraa.com

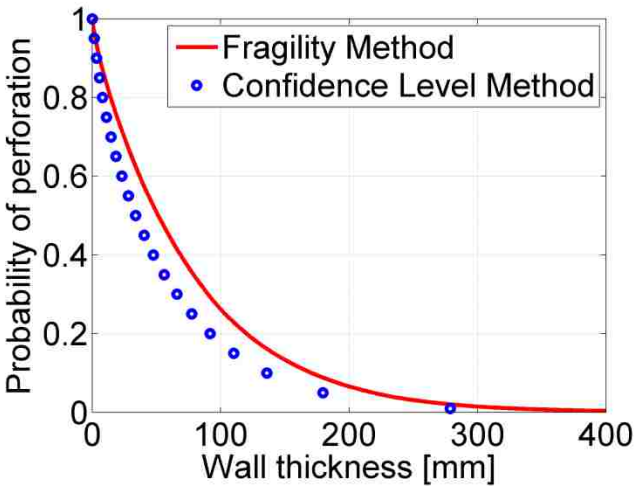

Figure 107: Fragility method versus confidence level method for a mean standoff of 12m

Furthermore, as the standoff distance is decreased, the confidence level method and fragility analysis begin to converge for all wall thicknesses. This is due to the fact that at small standoff distances (less than 6.1m (DoD 2008c)) the fragment strike velocity will be approximately equal to the initial velocity, regardless of the fragment mass or drag. However, the confidence level method is unable to account for the actual probability of fragment strike due to fragment trajectory (initial launch angle and direction) and wall area.

Injury to Personnel

For a given wall thickness and standoff distance, 100,000 samples were used in the Monte Carlo simulation and thus 100,000 fragments with a particular fragment mass and fragment velocity were considered. Each of these samples is plotted against the human critical organ injury thresholds as shown in Figure 108. In the case that the fragment did not penetrate the wall, the fragment velocity is zero. Figure 108 clearly demonstrates how the dispersion of the fragment mass and velocity is much greater than the different thresholds for each critical organ, thus justifying the use of a single threshold curve. Additionally, treating the organ threshold as a stochastic variable would make little difference in the results since the

www.manaraa.com

coefficient of variation for each human critical organ injury threshold is very small compared to the dispersion in fragment mass and velocity.

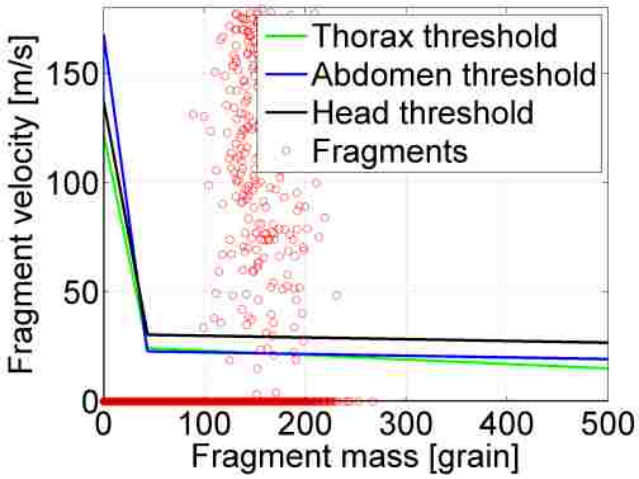

Figure 108: Fragment mass and velocity versus critical organ damage threshold for a mean wall thickness of 152mm and a mean standoff of 12m

Only injuries occurring from perforation of the wall are considered. Concrete spall from primary fragments generally results in velocities less than 1.5m/s (DoD 2008c), thus spall from fragment penetration alone is unlikely to cause personnel injury. However, when designing a wall system it is important to also consider the blast pressure from the explosive, which can create lethal spall velocities (Naito et al. 2014b).

By taking the quotient of the number of samples that fall in the injury area, referred to as "lethal fragments", and the total number of samples, it is possible to compute the probability of injury occurring. In this paper, it is assumed that lethal fragment generation and injury are directly correlated, i.e. when a lethal fragment occurs injury will also occur. This can then be repeated for multiple wall thicknesses by following the procedure depicted in Figure 103 in order to obtain a fragility curve for injury where the wall thickness is the intensity measure.

www.manaraa.com

Figure 109 plots the probability of injury occurring for the standoff distances corresponding to the high, medium, and low threat levels provided in Table 19. The solid lines represent the probability of injury occurring if all fragments strike the wall panel while the dotted lines represent the probability of injury occurring considering fragment trajectory. Intuitively, a thinner wall thickness and smaller standoff distance increases the likelihood of injury occurring.

As seen in Figure 109, there exists a possibility that even with an infinitesimally thin wall the personnel subjected to the mortar blast may not be struck by a fragment traveling fast enough or with enough mass to cause injury, thus neither the solid or dotted curves reach a probability of 100%. However, at the standoff distances prescribed in Table 19, the effects of the over pressure developed during the detonation will likely harm a person if no physical barrier is present.

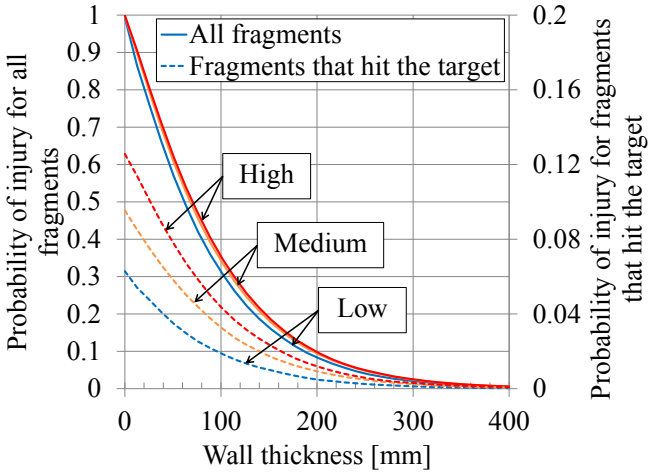

Figure 109: Probability of injury

6.1.4. Ballistics and Fragments Conclusions

Probabilistic analyses were conducted in order to design reinforced concrete wall systems against ballistic threats from small arms fire and fragmenting munitions. The study

www.manaraa.com

presents an approach for assessing the likelihood of perforation, residual velocity, and life safety of occupants given various design scenarios. The following conclusions can be drawn:

- The approach can be used to develop fragility curves for assessing perforation of a concrete wall based on a design threat. The four design levels for direct fire weapons threats from UFC 4-023-07: Very High, High, Medium and Low are used as a basis. Currently, UFC 4-023-07 does not furnish a method for calculating the probability of wall penetration or residual velocity.
- The fragility curves for fragment perforation deviate significantly from the confidence level method set forth in UFC 3-340-02. This indicates that the use of stochastic variables to define the fragment threat affects the probability of perforation and spall.
- Fragility curves can be developed which account for fragment trajectory, while the confidence level method in UFC 3-340-02 does not differentiate between all fragments generated from the munition and fragments that will actually strike the target.
- The likelihood of injury can be assessed based on critical organ thresholds presented in UFC 3-340-02. The variance in organ tolerance is much smaller than the variance in fragment mass and velocity, justifying the use of a single, deterministic injury threshold for all organs.
- The fragility curves for injury can be developed for various threat levels with the wall thickness as the intensity measure to quickly provide the engineer and owner with an understanding of the level of safety of the wall system for the defined threat level.
- The work presented provides a probabilistic framework for assessing the probability of exceeding a given limit state (e.g. design threat, wall thickness, or injury threshold),

www.manaraa.com

allowing engineers to develop tools to quickly quantify the safety of a structure under direct and indirect fire weapons' demands.

www.manaraa.com

7. FULL SYSTEM INTEGRATION

The goal of this phase of the research is to assess the performance of an insulated panel utilizing the finger tie and analytical models developed throughout the entire research project. The insulated panel will be based on a 32in wide by 10ft clear span 3-2-3 layout with 4000psi strength concrete, typical of panels experimentally tested in the laboratory. Constitutive properties determined for the finger tie will be used in the analytical model developed for insulated wall panels to determine the number of ties to use as well as the location of each tie. The insulated wall panel's resistance function will be developed using the analytical model and the prescribed tie locations. The performance of the panel under a blast load will be assessed via single degree of freedom (SDOF) analysis and the blast load prescribed for the ACI blast blind contest (Olmati et al. 2014) scaled by a 25%.

In addition to far-field demands, the response of the panel to close-in threats will be examined. The panel will be subjected to the same explosive charge and standoff as in (Naito et al. 2014b). Spall and breach will be determined using developed empirical methods and experimental results (Naito et al. 2014b).

Additionally, the hazard to personnel behind the wall from ballistic and fragment loads will be assessed for the wall panel using the fragility method previously developed (Trasborg et al. 2014a). The threat levels presented in (DoD 2008a) will be used for the ballistic threat while an 81MM M821 will be used for the fragment threat just as in (Trasborg et al. 2014a).

Finally, based on the shear tie layout, a finite element analysis will be conducted to determine the R-value of the insulated wall panel. Heat flux contour plots will be provided to show heat flow through the panel. Analytical calculations will be conducted to validate the numerical results.

www.manaraa.com

7.1. Far-Field Performance

Given the cross section provided in Figure 110, the moment-curvature relationships are developed for the composite and non-composite panels without any information on the shear tie connector. From the moment-curvature relationships, the moment-rotation behavior of the composite and non-composite panels was computed with the methodology provided in (Trasborg et al. To be submitted).

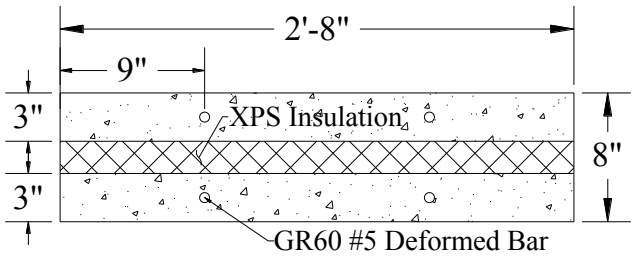

Figure 110: Panel cross section

Following the procedure described in (Naito et al 2012), a backbone curve was computed for the finger tie as shown in Figure 111. Utilizing the simplified constitutive property of the finger tie and the method provided in (Trasborg et al. To be submitted), the response of the partially-composite panel was calculated. Additionally, considering that the shear tie will be redesigned to have a ductile response, the response of the partially-composite was computed for such a tie titled “Ductile Tie” in Figure 111.

www.manaraa.com

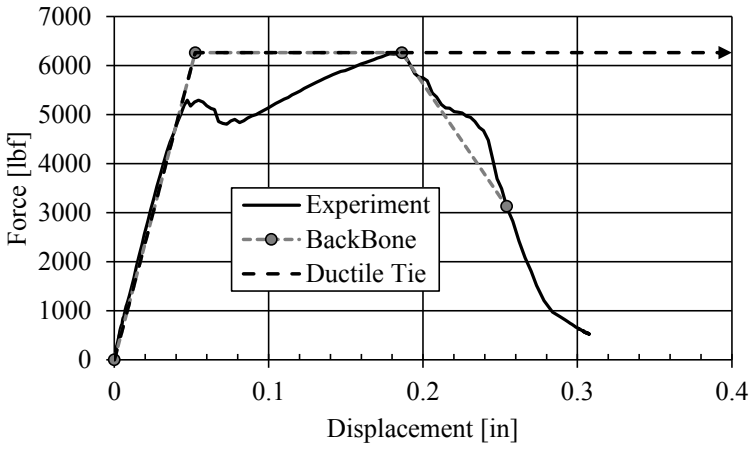

Figure 111: Finger tie backbone curve

A moment-rotation performance balanced between deformation capacity and strength is necessary for a panel to perform well under a blast load. Additionally, the number of ties required to meet the desired moment-rotation behavior should be reasonable. The number of ties and tie location were iterated until the requirements were met. The tie layout is provided in Figure 112. Placing the ties near the center of the panel sacrifices the global panel stiffness and overall strength; however, the ductility of the panel is increased which is vitally important to dissipate the energy generated during a detonation. Additionally, the layout was optimized for the "Ductile Tie" system. Figure 112 shows the layout for the "Ductile Tie" system on the left and the original finger tie system on the right.

www.manaraa.com

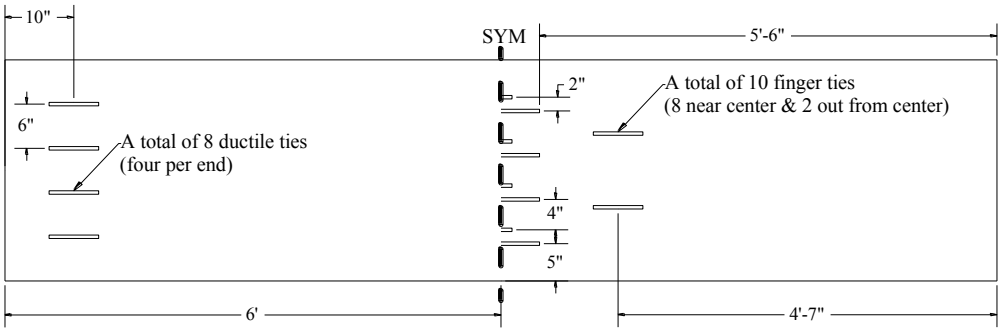

Figure 112: Panel tie layout for original finger ties and ductile ties

The moment-rotation response of the original finger tie panel is provided in Figure 113. By knowing the boundary conditions and span length, the applied moment can be converted to a pressure load which is commonly used to describe the resistance function of a system in blast design. Additionally, the moment-rotation response of the "Ductile Panel" is provided in Figure 113. Back-bones were developed for each panel resistance function as shown in Figure 113. By using the ductile tie layout, the panel was able to reduce the number of ties from 12 to 8 and still maintain the same strength, but have a stiffer response.

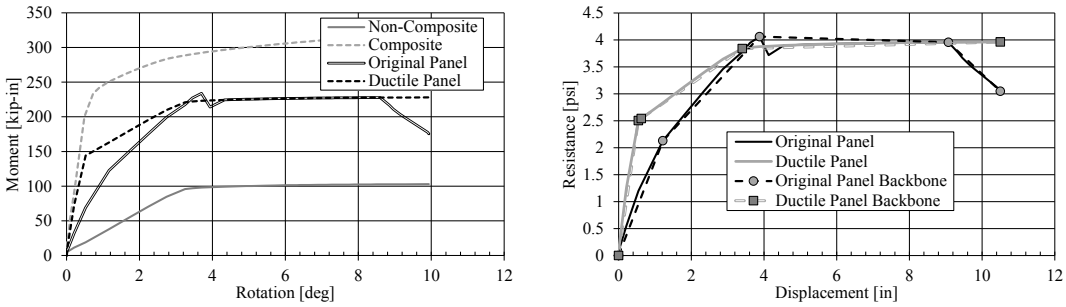

Figure 113: Original finger tie panel and ductile panel moment-rotations

The resistance function each panel is used in an SDOF analysis to predict the response of the panel to a blast load. Load-mass transformation factors are applied such that the single

www.manaraa.com

degree system will have equal kinetic, work and strain energies at all points in time as the actual system (PCI 2010a). For a simply supported panel under uniform loading, the elastic and plastic load-mass factors are equal to 0.78 and 0.66 respectively. For rebound, it is assumed that no component degradation has occurred with a kinematic hardening material model. Dynamic increase factors were not applied to the steel or concrete in order to avoid iteration and to simplify the analysis.

"Blast load 2" from the ACI Blast Blind Contest (Olmati et al. 2014) was scaled by 0.25 and applied to the finger tie panel. To carry out the SDOF analysis and obtain the time-history result of the panel, the constant velocity numerical method was selected as described by Biggs (Biggs 1964) due to the ease of implementation and unconditional stability. The time step was adjusted until the time-history results did not significantly change. A time step of 0.2ms was found to be adequate. Figure 114 plots the applied load on the primary ordinate and the panel time-history analysis to the blast load on the secondary ordinate. The maximum deflection for the original finger tie panel was found to be 4.71 in. occurring at 66.4ms which correlates to 4.5° of support rotation. The maximum deflection for the ductile tie panel was found to be 3.79 in. occurring at 62.2ms which correlates to 3.6° of support rotation. Residual displacement was calculated by averaging all the points after one complete panel oscillation. The residual displacement was found to be 2.03 in. and 2.69 in. for the original finger tie and ductile tie respectively.

www.manaraa.com

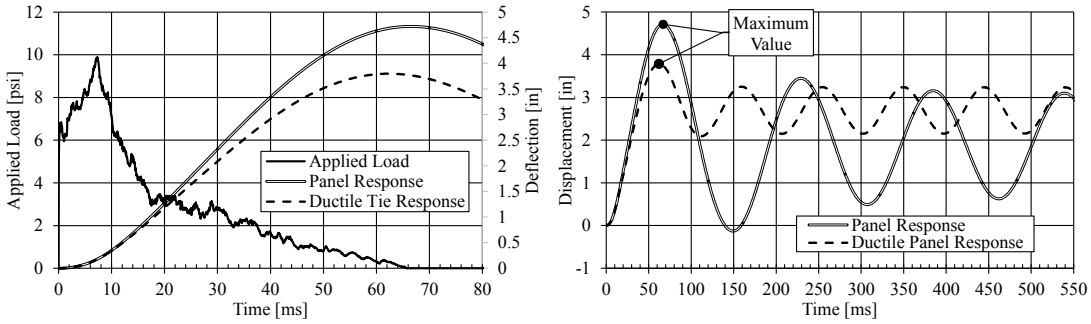

Figure 114: Original finger tie panel and ductile panel blast load response

The higher residual displacement for the ductile tie is attributed to the assumption of kinematic hardening which causes the panel to return on a larger stiffness than the original finger tie panel. This can be seen in the hysteresis of the resistance functions shown in Figure 115.

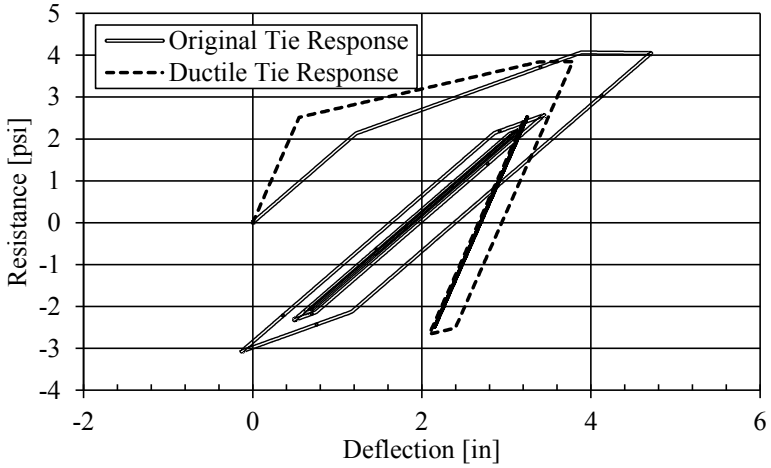

Figure 115: Original finger tie and ductile tie panel hysteresis

Table 23 reports the component damage flexural limits for non-prestress panels. Current flexural limits set forth by USACE (USACE 2008) are given in the top row while average panel response limits from experimental testing proposed by Naito (Naito et al 2014a) are provided in the second row. Based on the maximum support rotations of 4.5° and 3.6° for

www.manaraa.com

the finger tie and ductile tie panel respectively, the panels have sustained heavy and moderate degrees of damage according to USACE and Naito respectively.

Table 23: Component damage response limits				
Component damage level	***Superficial***	***Moderate***	***Heavy***	***Hazardous***
(USACE 2008)	$\mu \leq 1.0$	2.0°	5.0°	10.0°
(Naito et al 2014a)	0.78°	5.06°	6.51°	8.44°

7.2. Spall and Breach Performance

As concluded in the spall and breach section, empirical equations (DoD 2008b) do not represent the complex behavior occurring during a close-in detonation demand on an insulated wall panel. Conservatively assuming that the exterior wythe does not contribute to the resistance of the close-in detonation but adds to the stand-off distance (i.e. an increase in stand-off distance equal to the thickness of the exterior wythe), empirical equations indicate that the 3-2-3 panel will spall but not breach. However, experimental data indicates that the 3-2-3 panel configuration results in a spall and breach of both the exterior and interior wythes. Thus, for the demand considered in the prior spall and breach section, it is assumed the panel will spall and breach. More research is needed to develop empirical equations for insulated wall panels.

7.3. Ballistic and Fragment Performance

The four different threat levels prescribed in the UFC 4-023-07 for direct weapons fire are repeated in Table 18 (DoD 2008a) for convenience. The threat levels listed were derived from the Underwriters Laboratories Standard for Safety (UL 2005). The four threat levels are defined by the mass, impact velocity, size and shape of the ammunition. "N" is the nose performance coefficient of the ammunition round used.

www.manaraa.com

Table 24: Direct fire weapons threat parameters (DoD 2008a) (UL 2005)					
Design Basis Threat	UL 752 Level	N	Mass (grain)	Strike Velocity (m/s)	Diameter (mm)
Very High	10	1.31	709.5	856-942	12.95
High	9	1.39	166	828-910	7.82
Medium	5	1.26	150	838-922	7.82
Low	3	0.91	240	411-453	11.18

Note: "N" is the nose performance coefficient

Perforation limits and residual velocities are calculated with empirical equations provided in the UFC 4-023-07. For an insulated wall panel, it is conservative to assume that the strike velocity on the interior wythe is equal to the residual velocity of the bullet that perforated the exterior wythe. Using Monte Carlos simulations, fragility curves are developed with the intensity measure set as the residual velocity of the bullet. Figure 116 plots the fragility of the exterior and interior wythe, called "ext" and "int" respectively, for each of the four threat categories: very high, high, medium, and low. The absence of the interior wythe fragility for the low threat category indicates that the probability of the bullet perforating the interior wythe is 0%. Large shifts between the exterior and interior wythe fragilities indicates that the residual velocity of the bullet exiting the exterior wythe has decreased enough that the interior wythe can have a significant effect on the life safety of personnel behind the wall.

www.manaraa.com

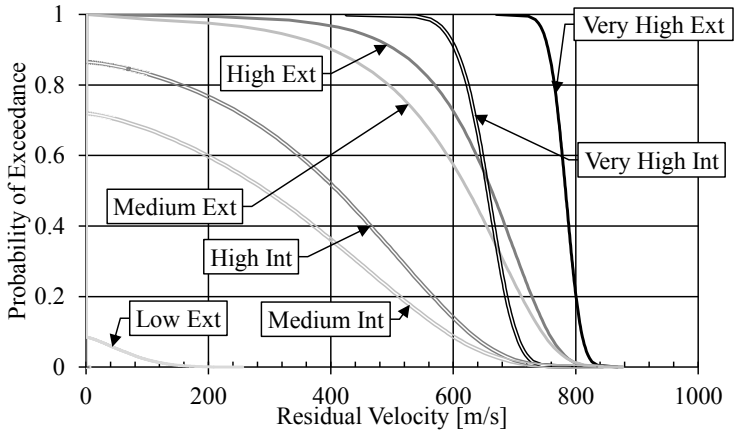

Figure 116: Fragility of the exterior and interior concrete wythes with residual velocity intensity measure

Similarly to the ballistic demands, fragility curves are developed for fragment demands. The fragment generating explosive was based on the same demands discussed previously, an 81MM M821 high explosive cartridge (AOLLC 2009) and a typical explosive (DoD 2008b). A standoff distance of 40ft was selected based on conventional construction standoff distances for load bearing, reinforced concrete walls of a high occupancy house (DoD 2012). To assess the probability of bodily harm, established human organ tolerance levels were followed (DoD 2008b).

Figure 117 provides fragility curves for probability of perforation with wall thickness as the intensity measure. From the perforation fragility curve, the probability for fragment generated from an 81MM M821 high explosive to perforate the exterior and interior wythe is 36.1% and 15.4% respectively. Additionally, Figure 117 provides the probability of exceedance with residual velocity as the intensity measure. The residual velocity fragility and fragment mass distribution is used to calculate the probability of injury occurring to personnel behind the wall panel. For the 3-2-3 panel, assuming that all fragments will strike the wall panel, the probability of injury occurring is 15.4%. As shown previously, if

www.manaraa.com

the fragment trajectory is taken into account, the probability of injury occurring is reduced significantly.

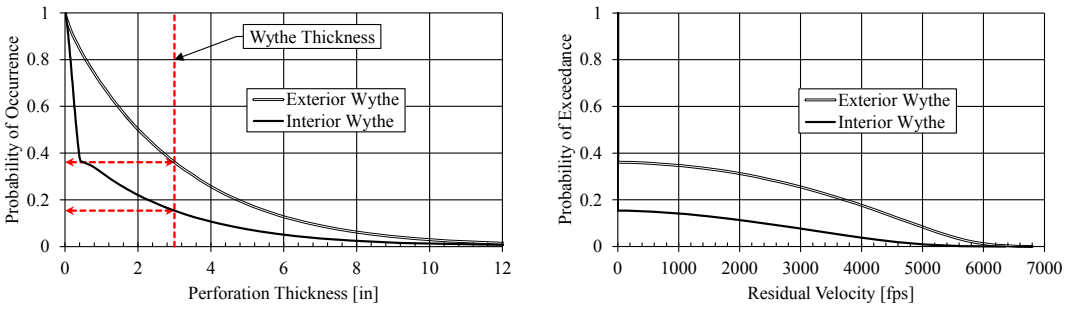

Figure 117: Probability of perforation and residual velocity exceedance

7.4. Thermal Performance

A finite element analysis was performed using the multi-purpose finite element software Abaqus. An uncoupled heat transfer analysis was conducted. In an uncoupled heat transfer analysis, the stress/deformation state of the wall is assumed to have no effect on overall system's R-value to simplify each numerical model. Additionally, the material properties were assumed to be temperature independent due to lack of literature available. The boundaries of the walls were assumed to be perfectly insulated.

All material resistances were taken from PCI 7th edition (PCI 2010b) handbook thermal section, ASHRAE handbook fundamentals (ASHRAE 2005), or from a material property data sheet (MatWeb 2014). In this study, R will be in English units of *[(°F*hr*ft^2)/(BTU*in)]* for resistance per thickness and *[(°F*hr*ft^2)/(BTU)]* for resistance. The assumed properties are summarized in Table 25.

www.manaraa.com

Table 25: Material resistances	
Material Description	**Resistance/thickness** *[(°F*hr*ft²)/(BTU*in)]*
Extruded polystyrene (XPS)	5.0
G10 Garolite	2.0
Normal Weight Concrete (140 pcf)	0.10

The entire panel was modeled in three dimensions consisting of the full length and width of the panel. Figure 118 shows the insulation and shear tie mesh with the concrete removed for both the original finger tie panel and the new ductile tie panel. The 8-node linear heat transfer brick, DC3D8, was selected for the analysis. This is a typical element used for uncoupled heat transfer applications (Dassault Systèmes 2010).

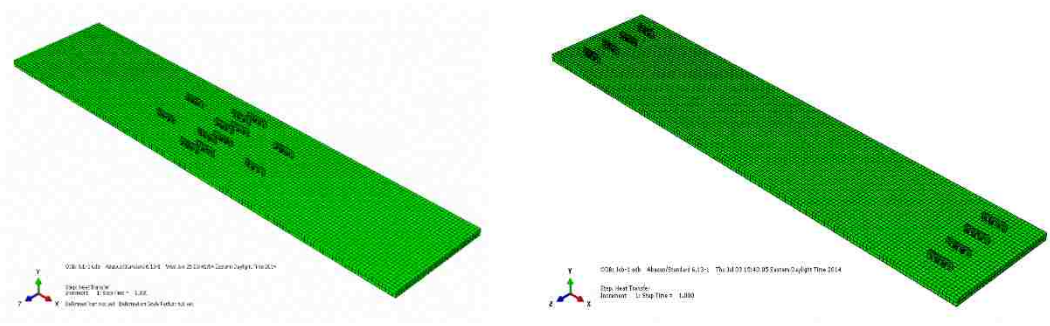

Figure 118: Finite element model mesh

The procedure to determine the R-Value of each panel follows that given by B. Lee and S. Pessiki (Lee and Pessiki 2008). Convection loading was used to represent the boundary conditions on the hot and cold surfaces of each panel. For all other surfaces, Abaqus assumes an adiabatic boundary condition. The R-Value can be directly computed using Equation 54.

$$R = A(t_h - t_c)/Q \qquad \text{Equation 54}$$

Where A is the cross sectional area of a surface perpendicular to the direction of heat transfer, Q is the heat flow rate through that surface which is directly computed from the heat flux values output from the FEA. t_h and t_c are the temperatures on the hot and cold

www.manaraa.com

surface, respectively.

When using convection boundary conditions, the temperatures, t_h and t_c, may be taken as either the surface temperatures or the ambient air temperatures. For building applications, the R-Value is typically computed using the ambient air temperatures. For this analysis, t_h = 125 °F and t_c = 25 °F.

Figure 119 plots the progression of the heat transfer through the concrete wythe and insulation for the original finger tie panel on the left and the new ductile tie panel on the right. The numerical analysis resulted in a total panel R-value of 11.2 and 11.3 (°F*hr*ft^2)/(BTU) for the original finger tie panel and new ductile panel respectively. A model was also conducted removing the shear ties entirely to determine the effect of the thermal bridging. Due to the low conductivity of G10 Garolite, the R-value for the panel increased by approximately 3% for the original finger tie panel. Analytical calculations performed to validate the numerical model resulted in a panel R-value of 10.4 (°F*hr*ft^2)/(BTU), approximately 7% lower than the numerical calculations.

www.manaraa.com

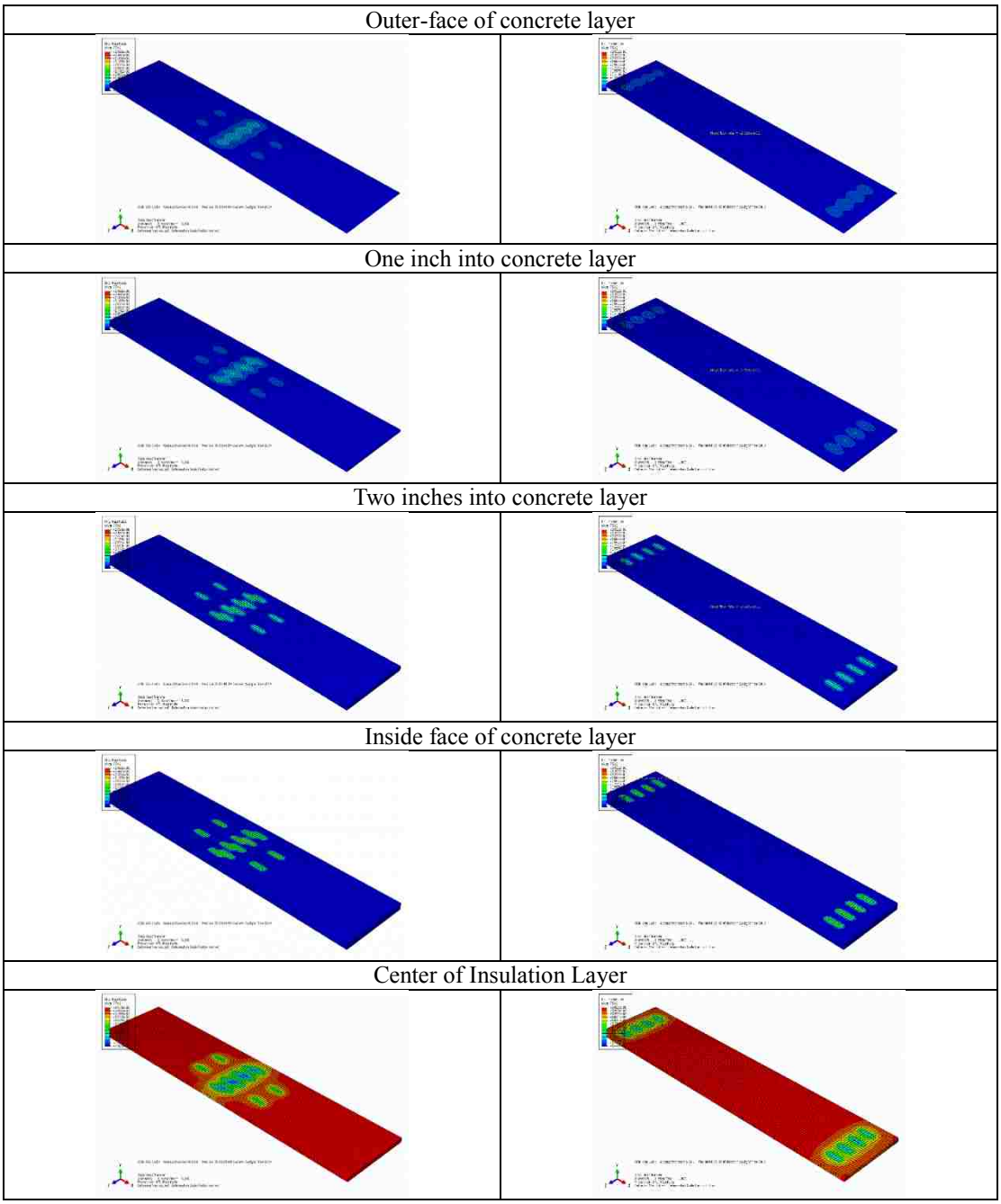

Figure 119: Heat flux contour plots through the original finger tie panel and new ductile tie panel on the left and right respectively

www.manaraa.com

8. CONCLUSIONS

8.1. Thermal Demands

- A solid concrete panel provides significantly less thermal resistance than a panel with shear ties or solid zones. By replacing 25% of the interior with insulation, the R-value is increased by 92%. This is a conservative value as the minimum reported resistance for the insulation was used.
- Solid-zones and steel ties can have detrimental effects on the overall R-value of the panel. In the case considered, the R-value was decreased by nearly 78% and 62% respectively.
- The modified zone method yields the same results as the isothermal planes and parallel flow methods when there are no materials bridging across a different another i.e. there are no solid zones or shear ties. This is due to the fact that there are no paths for lateral heat transfer to occur. On the other hand, the isothermal planes and parallel flow methods yield extremely different results when highly conductive materials are embedded due to the large lateral heat paths.

8.2. Far-Field Detonations

- A fiber analysis can provide an accurate prediction of the moment-curvature for a reinforced concrete slab given the material properties of the reinforcement and concrete as well as the geometry of the panel and placement of the reinforcement.
- Moment-curvature analysis can be used for the prediction of the resistance function for a reinforced concrete slab with varying boundary conditions. Boundary conditions can

www.manaraa.com

be adjusted as the panel deflects in an analytical model if the panel response is carefully monitored and saved at each boundary condition transition.

- Single degree of freedom analysis can provide an accurate prediction of the time-history response of a reinforced concrete slab subjected to a blast load when given the duration and magnitude of the load, assuming the loading is uniform on the surface of the panel.
- Analytical methods compare to the experimental results, indicating that analytical methods are suitable for a quick check when more time consuming and computationally expensive numerical methods are not available.
- A flexural mechanism with sustained resistance does not occur in thin concrete elements due to crushing of the concrete in the compression zone. The fiber analysis model conducted in this paper confirms that panels which are classified as tension controlled by ACI 318-11 R10.3.4 may have limited ultimate deformation capacity due to concrete compression failure.
- A predictable hinge can be created by utilizing a specially designed steel mechanism at the center of the panel. Dogbone panels were designed to obtain a support rotation of 10° and a yield force equal to the nominal moment of a conventionally reinforced panel. Analytical methods based on first principles accurately predict the behavior of the dogbone panel.
- Dogbone panels require considerable effort to fabricate, deviating significantly from traditional cast-in-place techniques. Further research on alternative design details may be required for the dogbone method to be applicable in practice.

www.manaraa.com

- Locally unbonding longitudinal reinforcement provides a predictable, ductile flexural mechanism in an emulative manner while maintaining enough development to allow transmission of the necessary bar forces to attain a high panel resistance.
- An analytical model based on a localized flexural mechanism and deformable beams was developed to predict the behavior of unbonded panels.
- As illustrated through experimental tests on solid panels and analytical modeling, prestressed panels have less deformation capacity than non-prestressed panels due to smaller ultimate material strains; however, prestressed panels have a stiffer initial response compared to non-prestressed panels due to the initial jacking force of the prestressed delaying the onset of cracking. The improvements in ductility are diminished for insulated panels with low levels of composite action.
- All insulated panels tested have measurable end-slip despite the fact that some of the panels achieve a fully composite behavior, indicating that the assumption of composite behavior is incorrect.
- The PCI design approach is based on force equilibrium alone and does not consider the constitutive properties of the connector or compatibility between the wythes. This methodology may be acceptable for handling and service loads, but for panels loaded to their nominal strength a deformation based approach is necessary. Additionally, the PCI approach may lead to an unconservative design, particularly if brittle shear ties are utilized.
- For the panels examined, the PCI design approach generally provides a conservative estimate of percent composite action. The design composite level was typically lower than the actual composite level achieved.

www.manaraa.com

- As illustrated through experimental testing and parametric studies, the global performance of an insulated panel is dependent on the constitutive properties of the shear connector: stiffness, strength, and deformation capacity, as well as tie placement within the panel.
- An analytical approach is developed which accounts for equilibrium, compatibility, and the constitutive properties of the ties. The approach provides an accurate method for determining the moment-deflection of partially-composite panels.
- Experiments indicate that locally unbonding has no significant effect on the performance of an insulated panel. This is attributed to the fact that the response of the insulated panel is controlled by the shear ties.
- The effect of locally unbonding solid, double reinforced prestressed or non-prestressed panels is unclear. Future numerical modeling would provide insight into the behavior of a locally unbonded wall panel.
- The analytical model developed for singly reinforced slabs provides an accurate estimate of the ultimate deflection and maximum moment for both prestressed and non-prestressed panels. However, the method provides a conservative response of both panels in general.

8.3. Close-In Detonations

- The solid 6 in. concrete panel (6C panel) and the panel composed of two stacked 3 in. wythes (3C-0F-3C panel) provide a comparable level of resistance to close-in detonations. The mechanism of failure however is altered in that the stacked panel

www.manaraa.com

prevents the occurrence of a complete breach with minimal damage on the exterior wythe and breach only on the interior wythe.

- The use of EPS insulation foam resulted in mixed performance as a function of the insulation foam thickness. Small amounts of insulation, 2 in. (51 mm), resulted in a full breach (similarly as the experimental results of Yamaguchi et al. (2011)) while the case with no insulation (3C-0F-3C panel) had no breach. Greater thicknesses of insulation resulted in full protection of the interior wythe with no damage on either the front or rear face of the interior wythe.
- The empirical formulations for spall and breach matched the data for the solid panel (6C panel).
- The use of empirical formulations for predicting the spall and breach on the insulated wall panels was made by assuming that the exterior wythe was not present and the stand-off distance was increased. This approach was found to be inaccurate as it does not represent the complex behavior that occur, as the shockwave propagates through the various panel materials and the external wythe debris impacts the interior wythe.
- The numerical simulations are able to predict the occurrence of the spall and breach for insulated panels subjected to close-in detonations; the breach diameters on the rear face of the interior wythe were found to be marginally unconservative for small foam thickness but bound the response at higher thicknesses.
- The numerical models indicate that the density and strength of the insulation foam is the main factors in transfer of demand to the interior wythe.

www.manaraa.com

- The numerical models supported the experimental data and could be used to further develop semi empirical spall and breach curves for insulated wall panels subjected to close-in detonations.

8.4. Ballistic Demands

- The approach can be used to develop fragility curves for assessing perforation of a concrete wall based on a design threat. The four design levels for direct fire weapons threats from UFC 4-023-07: Very High, High, Medium and Low are used as a basis. Currently, UFC 4-023-07 does not furnish a method for calculating the probability of wall penetration or residual velocity.
- The fragility curves for fragment perforation deviate significantly from the confidence level method set forth in UFC 3-340-02. This indicates that the use of stochastic variables to define the fragment threat affects the probability of perforation and spall.
- Fragility curves can be developed which account for fragment trajectory, while the confidence level method in UFC 3-340-02 does not differentiate between all fragments generated from the munition and fragments that will actually strike the target.
- The likelihood of injury can be assessed based on critical organ thresholds presented in UFC 3-340-02. The variance in organ tolerance is much smaller than the variance in fragment mass and velocity, justifying the use of a single, deterministic injury threshold for all organs.
- The fragility curves for injury can be developed for various threat levels with the wall thickness as the intensity measure to quickly provide the engineer and owner with an understanding of the level of safety of the wall system for the defined threat level.

www.manaraa.com

- The work presented provides a probabilistic framework for assessing the probability of exceeding a given limit state (e.g. design threat, wall thickness, or injury threshold), allowing engineers to develop tools to quickly quantify the safety of a structure under direct and indirect fire weapons' demands.

8.5. Full System Integration

- Deformation capacity is critical to dissipating energy during a blast event. Placing a brittle tie near the center of a panel can increase the panel's overall maximum displacement; however, more ties are necessary to increase the panel strength. When using a ductile shear tie, shear ties should be placed at the ends of the panel for a more efficient design requiring less ties. By using the ductile shear tie system, the number of ties was able to be reduced by 33%. Any reduction in the number of ties will result in a reduction of cost due to less materials and less labor intensive installation.
- When subjected to the 25% of the blast load in the ACI blast contest, the wall was found to behave in a moderate to heavy damage level.
- The 3-2-3 panel is capable of stopping a low threat ballistic with 100% certainty; however, a high threat ballistic has an 86.5% chance of perforating the wall system. For the fragmenting munition considered, the wall system has 15.4% chance of causing injury to personnel behind the wall panel.
- Further research is required to develop accurate empirical equations for insulated wall panels; however, experimental data indicates that a 3-2-3 panel will undergo spall and breach in both the exterior and interior wythes.

www.manaraa.com

- The thermal resistance of the insulated wall panel with finger ties was found to be 11.2 (°F*hr*ft^2)/(BTU). Despite the significant shear tie area, the thermal resistance is only decreased by 3% with the inclusion of shear ties due to the low thermal conductivity of G10 Garolite. Using ductile shear ties will allow the designer to incorporate less shear ties in the panel, thus slightly increasing panel thermal resistance while decreasing panel cost.

www.manaraa.com

PAPERS

The following papers were produced during this research project and are either submitted or in press:

1. Trasborg, P., Naito, C., Davidson, J. (To be submitted). "Experimental and analytical evaluation of insulated wall panels." *ASCE Journal of Structural Engineering*.
2. Naito, C., Olmati, P., Trasborg, P., Davidson, J., Newberry, C. (2014). "Assessment of insulated concrete walls to close-in blast demands." *Journal of Performance of Constructed Facilities*, Submitted.
3. Olmati, P., Trasborg, P., Naito, C., Bontempi, F. (2014). "Prediction of Response of Reinforced Concrete Slabs using Finite Element Methods." *ACI Structural Journal Special Publication*, Submitted.
4. Trasborg, P., Naito, C., Bocchini, P., Olmati, P. (2014). "Fragility Analysis for Ballistic Design." *Structural Safety Journal*, STRUCS-D-14-00038, submitted.
5. Trasborg, P., Nickerson J., Naito C., Olmati P., Davidson J. (2014b). "Forming a predictable flexural mechanism in reinforced wall elements." *ACI Structural Journal*, Submitted.
6. Trasborg, P., Naito, C. (2013). "Composite action in insulated concrete wall systems." *Concrete Plant International,* 6, 164-168.

www.manaraa.com

REFERENCES

1. American Concrete Institute (ACI). (2011). "Building Code Requirements for Structural Concrete and Commentary." *ACI Committee 318*. ACI 318-11.

2. ACI. (2013). "Blast Blind Simulation Contest 2012." *ACI 447 ACI 370*, <http://sce.umkc.edu/blast-prediction-contest/experimental_program.html> (July 1, 2014).

3. American Ordnance LLC (AOLLC). (2009) "Mortars and mortar components." <*http://www.aollc.biz/mortars.htm*> (January 21, 2014).

4. Ang, A., H-S., Tang, W., H. (2007). "Probability concepts in engineering: emphasis on applications to civil and environmental engineering 2nd edition." *John Wiley & Sons*.

5. Arnold, W., Rottenkolber, E. (2008). "Fragment mass distribution of metal cased explosive charges." *International Journal of Impact Engineering*, 35: 1393-1398.

6. American Society of Heating, Refrigerating and Air-Conditioning Engineers, Inc (ASHRAE). (2005). "2005 ASHRAE handbook fundamentals inch-pound edition." *ASHRAE*.

7. ASTM. (2002). "C469-02 Standard Test Method for Static Modulus of Elasticity and Poisson's Ratio of Concrete in Compression." *ASTM International*, West Conshohocken, PA, 2012, DOI: 10.1520/C0469-02, <www.astm.org>.

8. ASTM. (2003). "Standard E488: Standard Test Methods for Strength of Anchors in Concrete and Masonry Elements." *ASTM International 2003*, West Conshohocken, PA, 2003, <www.astm.org>.

www.manaraa.com

9. ASTM. (2004). “E8-04 Standard Test Methods for Tension Testing of Metallic Materials.” *ASTM International*, West Conshohocken, PA, 2012, DOI: 10.1520/E0008-04, <www.astm.org>.

10. ASTM. (2005). “C39 Standard Test Method for Compressive Strength of Cylindrical Concrete Specimens.” *ASTM International*, West Conshohocken, PA, 2005, DOI: 10.1520/C0039_C0039M-05E01, <www.astm.org>.

11. ASTM. (2009). “A615 Standard Specification for Deformed and Plain Carbon-Steel Bars for Concrete Reinforcement.” *ASTM International*, West Conshohocken, PA, 2012, DOI: 10.1520/A0615_A0615M-09, <www.astm.org>.

12. ASTM. (2009). “A706 Standard Specification for Low-Alloy Steel Deformed and Plain Bars for Concrete Reinforcement.” *ASTM International*, West Conshohocken, PA, 2012, DOI: 10.1520/A0706_A0706M-09, <www.astm.org>.

13. ASTM. (2010). "A1064 Standard Specification for Steel Wire and Welded Wire Reinforcement, Plain, and Deformed, for Concrete." *ASTM International*, West Conshohocken, PA, 2010, DOI: 10.1520/A1064_A1064M-10, <www.astm.org>.

14. ASTM. (2010). “D638-10 Standard test method for tensile properties of plastics.” *ASTM International*, West Conshohocken, PA, 2010, DOI: 10.1520/D0638-10, <www.astm.org>.

15. ASTM. (2012). “A370-12 Standard Test Methods and Definitions for Mechanical Testing of Steel Products.” *ASTM International*, West Conshohocken, PA, 2012, DOI: 10.1520/A0370-12, <www.astm.org>.

www.manaraa.com

16. ASTM. (2012). “A572/A572M-12 Standard Specification for High-Strength Low-Alloy Columbium-Vanadium Structural Steel.” *ASTM International*, West Conshohocken, PA, 2012, DOI: 10.1520/A0572_A0572M-12, <www.astm.org>.

17. ASTM. (2012). "A615 Standard Specification for Deformed and Plain Carbon-Steel Bars for Concrete Reinforcement." *ASTM International*, West Conshohocken, PA, 2012, DOI: 10.1520/A0615_A0615M-12, <www.astm.org>.

18. ASTM. (2012). “C31/C31M-12 Standard practice for making and curing concrete test specimens in the field.” *ASTM International*, West Conshohocken, PA, 2012, DOI: 10.1520/C0031_C0031M-12, <www.astm.org>.

19. ASTM. (2012). “C617/C617M-12 Standard practice for capping cylindrical concrete specimens.” *ASTM International*, West Conshohocken, PA, 2012, DOI: 10.1520/C0617_C0617M-12, <www.astm.org>.

20. Beth, R., A. (1946). “Final report of concrete penetration.” *Report No. 6459*, Office of Scientific Research and Development.

21. Benayoune, A., Abdul Samad, A., A., Trikha, D., N., Abang Ali, A., A., Ellinna, S., H., M. (2008). “Flexural behavior of pre-cast concrete sandwich composite panel – experimental and theoretical investigations." *Construction and Building Mat.*, 22: 580-592.

22. Biggs, John M. (1964). “Introduction to Structural Dynamics.” *McGraw-Hill*, New York.

23. Bontempi, F., Malerba, P.G. (1997). “The role of softening in the numerical analysis of R.C. framed structures.” *Structural Engineering and Mechanics*, 5(6): 785-801.

www.manaraa.com

24. Bontempi, F., Faravelli, L. (1998) "Lagrangian/Eulerian description of dynamic system." *Journal of Engineering Mechanics*, 124(8): 901-911.

25. Børvik, T., Dey, S., Clausen, A.H. (2009). "Perforation resistance of five different high strength steel plates subjected to small-arms projectiles." *International Journal of Impact Engineering*, 36: 948-964.

26. Bush, T. D., and Stine, G. L. (1994). "Flexural behavior of composite pre-cast concrete sandwich panels with continuous truss connectors." PCI J., 39(2): 112–121.

27. CEB-FIP model code 1990. Trowbridge, Wiltshire, UK: Committee Euro-International Du Beton, Redwood Books; 1993.

28. Chen, W.F. (1982). "Plasticity in Reinforced Concrete." *Mc Graw Hill*, New York.

29. Chen, W., Hao, H. (2012). "Numerical study of a new multi-arch double-layered blast-resistance door panel." *International Journal of Impact Engineering*, 43: 16-28.

30. Chopra, A., K. (2007). "Dynamics of structures: theory and applications to earthquake engineering 3rd edition." *Pearson Education.*

31. Collins, T., F. (1954). "Precast concrete sandwich panels for tilt-up construction." *ACI J.,* 26(2): 149-164.

32. Cornell, C., A., Krawinkler, H. (2000). "Progress and challenges in seismic performance assessment." *PEER Center News*, 3(2).

www.manaraa.com

33. Coughlin, A.M., Musselman, E.S., Schokker, A.J., Linzell, D.G. (2010). "Behavior of portable fiber reinforced concrete vehicle barriers subject to blasts from contact charges." *International Journal of Impact Engineering 2010*, 37: 521-529.

34. Cowper G.R., Symonds P.S. (1957). "Strain hardening and strain rate effects in the impact loading of cantilever beams." *Applied Mathematics Report No. 28*, Brown University, Providence, Rhode Island, USA.

35. Dassault Systèmes. (2010). "Abaqus Unified FEA Software Ver. 6.10." *Dassault Systèmes Simulia Corp*., Providence.

36. Croop, B., Lobol, H. (2009). "Selecting material models for the simulation of foam in LS-DYNA." *Proceedings: 7th European LS-DYNA Conference*, Salzburg, Austria.

37. Davidson, J.S., Fisher, J.W., Hammons, M.I., Porter, J.R., Dinan, R.J. (2005). "Failure mechanisms of polymer-reinforced concrete masonry walls subjected to blast." *Journal of Structural Engineering,* 131(8): 1194-1205.

38. Department of Defense (DoD). (2008a). "Design to resist direct fire weapons effects." *UFC 4-023-07*, United States of America.

39. Department of Defense (DoD). (2008b). "DoD security engineering facilities planning manual." *UFC 4-020-01*, United States of America.

40. Department of Defense (DoD). (2008c). "Unified Facilities Criteria: Structures to resist the effects of accidental explosions." *UFC 3-340-02*, United States of America.

41. Department of Defense (DoD). (2012). "DoD minimum antiterrorism standards for buildings." *UFC 4-010-01*, United States of America.

www.manaraa.com

42. Di Landro, L., Sala, G., Olivieri, D. (2002). "Deformation mechanisms and energy absorption of polystyrene foams for protective helmets." *Polymer Testing*, 21: 217-228.

43. El-Sheikh, M., Pessiki, S., Sause, R., Lu, L.W. (2000). "Moment rotation behavior of unbonded post-tensioned precast concrete beam-column connections." *ACI Structural Journal*, 97(1): 122-131.

44. Elek, P., Jaramaz, S. (2009). "Fragment mass distribution of natural fragmenting warheads." *Faculty of Mechanical Engineering Transactions*, Belgrade, 37(3).

45. Enright., M., P., Frangopol, D., M. (1998). "Probabilistic analysis of resistance degradation of reinforced concrete bridge beams under corrosion." *Engineering Structures*, 20(11): 960-971.

46. Fedrizzi, R. (2014). "Dear Mr. President: support better buildings through executive action." *Advocacy and policy,* <http://www.usgbc.org/articles/dear-mr-president-support-better-buildings-through-executive-action> (May 28, 2014).

47. Flores-Johnson, E.A., Saleh, M., Edwards, L. (2011). "Ballistic performance of multi-layered metallic plates impacted by a 7.62-mm APM2 projectile." *International Journal of Impact Engineering*, 38: 1022-1032.

48. Forrestal, M., Børvik, T., Warren, T. (2010). "Perforation of 7075-T651 aluminum armor plates with 7.62 mm APM2 bullets." *Experimental Mechanics*, 50: 1245-1251.

49. Frankl, B., A., Lucier, G., W., Hassan, T., K., Rizkalla, S., H. (2011). "Behavior of precast, prestressed concrete sandwich wall panels reinforced with CFRP shear grid." *PCI Journal*: 42-54.

www.manaraa.com

50. Giovino, G, Olmati, P, Garbati, S, Bontempi, F. (2014). "Blast resistance assessment of concrete wall panels: experimental and numerical investigations." *International Journal of Protective Structures*, Submitted.

51. Grote, D.L., Park, S.W., Zhou, M. (2001). "Dynamic behavior of concrete at high strain rates and pressures: I experimental characterization." *International Journal of Impact Engineering*, 25: 869-886.

52. Gurney, R.,W. (1943). "The Initial Velocities of Fragments from Bombs, Shells and Grenades." *Report No. 405*, Ballistic Research Laboratories, Aberdeen Proving Ground, Maryland.

53. International Code CouncIl (ICC). "About ICC." <*http://www.iccsafe.org/AboutICC/Pages/default.aspx*> (July 1, 2014).

54. International Code Council (ICC). (2006). "Evaluation Service: Acceptance Criteria for Fiber-Reinforced Composite Connectors Anchored in Concrete." *ICC Evaluation Report AC320*.

55. International Code Council (ICC). (2010). "Evaluation Service: Acceptance Criteria for Semicontinuous Fiber-Reinforced Grid Connectors Used in Combination with Rigid Insulation in Concrete Sandwich Panel Construction." *ICC Evaluation Report AC422*.

56. International Code Council (ICC). (2006). "International Building Code." *Country Club Hills*.

57. Kaba, S., Mahin, S. (1984). "Refined Modeling of Reinforced Concrete Columns for Seismic Analysis." *Nisee e-library*, UCB/EERC-84/03, <http://nisee.berkeley.edu/elibrary/Text/141375> (July 1, 2014).

www.manaraa.com

58. Katz, A. (2012). "Green building facts." *Media*, <http://www.usgbc.org/articles/green-building-facts> (May 28, 2014).

59. Kennedy, R., P. (1975). "A review of procedures for the analysis and design of concrete structures to resist missile impact effects." *Nuclear Engineering and Design*, 37: 183-203.

60. Lawrence Software Technology Corporation (LSTC). (2012). "LS-DYNA keyword user's manual." *Livermore Software Technology Corporation*, Livermore, CA.

61. Lawrence Software Technology Corporation (LSTC). (2012) LS-DYNA theory manual. Livermore, California, US: *Livermore Software Technology Corporation*.

62. Lee, B.J.; Pessiki, S. (2008). "Revised Zone Method R-Value Calculation for Precast Concrete Sandwich Panels Containing Metal Wythe Connectors." *PCI Journal*, September-October.

63. Li, Q., M., Reid, S., R., Ahmad-Zaidi, A., M. (2006). "Critical impact energies for scabbing and perforation of concrete target." *Nuclear Engineering and Design*, 236: 1140-1148.

64. Li, Q.M., Reid, S.R., Wen, H.M., Telford, A.R. (2005). "Local impact effects of hard missiles on concrete targets." *International Journal of Impact Engineering*, 32: 224-284.

65. Luccioni, B.M., Luege, M.. (2006). "Concrete pavement slab under blast loads." *International Journal of Impact Engineering*, 32: 1248-1266.

www.manaraa.com

66. Luco, N., Cornell, C., A. (2000). "Structure-specific scalar intensity measures for near-source and ordinary earthquake ground motions." *Earthquake Spectra*, 23: 357-92.

67. Magee, L., Oats, A., Courtney, M. (2012). "Comparing measured bullet weight with manufacturer specifications." *Report No. 0704-0188*, DFRL U.S. Air Force Academy.

68. Mains, R.M. (1951). "Measurement of the Distribution of Tensile and Bond Stresses along Reinforcing Bars." *ACI Journal Proceedings*, 23(3): 225-252.

69. Malvar LJ, Crawford JE, Wesevich JW, Simons D. (1997) "A plasticity concrete material model for DYNA3D." *International Journal of Impact Engineering*, 19: 847-873.

70. Manenti, S., Sibilla, S., Gallati, M., Agate, G., Guandalini, R. (2012). "SPH Simulation of Sediment Flushing Induced by a Rapid Water Flow." *Journal of Hydraulic Engineering*, 138(3): 272-284.

71. Marchand, K., Woodson, S., Knight, T. (1994). "Revisiting Concrete Spall and Breach Prediction Curves: Strain Rate (Scale Effect) and Impulse (Pulse Length and Charge Shape) Considerations." *Department of the Army, Corps of Engineers*, Vicksburg, MS: 25.

72. Masso-Moreu, Y., Mills, N.J. (2003). "Impact compression of polystyrene foam pyramids." *International Journal of Impact Engineering*, 28: 653-676.

73. MatWeb. (2014). "G-10 fiberglass epoxy laminate sheet." *Material Property Data*. <http://www.matweb.com/search/datasheetText.aspx?bassnum=PGLAM04> (July 2, 2014).

www.manaraa.com

74. McMaster-Carr (2013). “More about hard fiber, fiberglass, garolite, and carbon fiber.” *Document 8549KAC*, <http://www.mcmaster.com/#8549kac/=sgw3c3> (July 2, 2014).

75. McVay, M. (1988). “Spall Damage of Concrete Structures.” *Department of the Army, Corps of Engineers*, Technical Report SL-88-22, Vicksburg, MS: 430.

76. Murray Y.D. (2007). “Users Manual for LS-DYNA Concrete Material Model 159.” *FHWA-HRT-05-062.*

77. Naito, C., Dinan, R., Bewick, B. (2011a). “Use of Precast Concrete Walls for Blast Protection of Steel Stud Construction.” *Journal of Performance of Constructed Facilities*, 25(5): 454-463.

78. Naito, C., Beacraft, M., Hoemann, J., Shull, J., Salim, H., Bewick, B. (2014a). “Blast performance of single-span precast concrete sandwich wall panels.” *ASCE Journal of Structural Engineering,* In press.

79. Naito, C.J., Hoemann, J., Beacraft, M., Bewick, B. (2012). “Performance and characterization of shear ties for use in insulated precast concrete sandwich wall panels.” *Journal of Structural Engineering*, 138(1): 52-61.

80. Naito, C., Hoemann, J., Shull, J., Saucier A., Salim, H., Bewick., B., Hammons, M. (2011b). "Precast/Prestressed Concrete Experiments Performance on Non-Load Bearing Sandwich Wall Panels." *Air Force Research Laboratory, Airbase Technologies Division Technical Report*, AFRL-RX-TY-TR-2011-0021, Distribution A: 164.

www.manaraa.com

81. Naito, C., Olmati, P., Trasborg, P., Davidson, J., Newberry, C. (2014b). "Assessment of insulated concrete walls to close-in blast demands." *Journal of Performance of Constructed Facilities*, Submitted.

82. Naito, C., Ren, R. (2013). "An evaluation method for precast concrete diaphragm connectors based on structural testing." *PCI Journal*, Spring: 106-118.

83. National Cooperative Highway Research Program (NCHRP). (2010). "Blast-resistant highway bridges: design and detailing guidelines." Washington D.C., US: *Transportation Research Board*.

84. National Defense Research Committee (NDRC). (1946). "Effects of impact and explosion." *Summary Technical Report of Division 2*, 1.

85. Ohkubo, K., Beppu, M., Ohno, T., Satoh, K. (2008). "Experimental study on the effectiveness of fiber sheet reinforcement on the explosive-resistant performance of concrete plates." *International Journal of Impact Engineering*, 35: 1702-1708.

86. Olmati, P., Trasborg, P., Naito, C.J., Bontempi, F. (2013). "Blast resistant design of precast reinforced concrete walls for strategic infrastructures under uncertainty." *International Journal of Critical Infrastructures*, In press.

87. Olmati, P., Trasborg, P., Naito, C., Bontempi, F. (2014). "Prediction of Response of Reinforced Concrete Slabs using Finite Element Methods." *ACI Structural Journal Special Publication*, Submitted.

88. Ozbolt, J., Sharma, A. (2011). "Numerical simulation of reinforced concrete beams with different shear reinforcements under dynamic impact loads." *International Journal of Impact Engineering*, 38: 940–950.

www.manaraa.com

89. Park, R., Paulay, T. (1975). “Reinforced Concrete Structures.” *John Wiley & Sons*, New York.

90. PCI Committee on Precast Sandwich Wall Panels (PCI). (2011). “State of the Art of Precast/Prestressed Concrete Sandwich Wall Panels.” *PCI Journal,* Spring: 131-176.

91. PCI Blast Committee (PCI). (2010a). “Blast-resistant design of precast/prestressed concrete components.” *Chicago.*

92. PCI Industry Handbook Committee (PCI). (2010b). “PCI Design Handbook: Precast and Prestressed Concrete 7th edition.” *Chicago.*

93. Petrini, F., Ciampoli, M. (2010). “Performance-based wind design of tall buildings.” *Structure and Infrastructure Engineering*, 8(10): 954-966.

94. Pfeifer, D. W., and Hanson, J. A. (1964). "Precast Concrete Wall Panels: Flexural Stiffness of Sandwich Panels." *American Concrete Institute*, Special Publication, SP-11, Farmington Hills, MI: 67-86.

95. Plumier, A. (1990). “The Dogbone: Back to the Future.” *AISC Engineering Journal*, 34(2): 61-67.

96. Popovics, S., (1973). “A Numerical Approach to the Complete Stress Strain Curve for Concrete, Cement and Concrete Research.” *Cement and Concrete Research*, 3(5): 583-599.

97. Preservation Green Lab. (2011). “The greenest building: quantifying the environmental value of building reuse.” *National Trust*, 13.

www.manaraa.com

98. Research and Analytics (2010). "Green outlook 2011: green trends driving growth." *McGraw-Hill Construction*.

99. Salmon, D. C., Einea, A. (1995). "Partially Composite Sandwich Panel Deflections." *ASCE Journal of Structural Engineering*, 121(4): 778-783.

100. Schenker, A., Anteby, I., Gal, E., Kivity, Y., Nizri, E., Sadot, O., Michaelis, R., Levintant, O., Ben-Dor, G. (2008). "Full-scale field tests of concrete slabs subjected to blast loads." *International Journal of Impact Engineering*, 35: 184-198.

101. Steinberg, D., S. (2000). "Vibration analysis for electronic equipment." *Wiley-Interscience*, 3rd edition.

102. Su, X.Y., Yu, T.X., Reid, S.R. (1995). "Inertia-sensitive impact energy-absorbing structures part ii: effect of strain rate." *International Journal of Impact Engineering*, 16: 673-689.

103. Tedesco, J.W., Powell, J.C., Ross, C.A., Hughes, M.L. (1997). "A strain-rate-dependent concrete material model for ADINA." *Computers and Structures*, 64: 1053-1067.

104. Thermomass®. (2012A). "Thermomass® X Series." *Thermomass® X Series Datasheet*, <http://www.thermomass.com/files/thermomass_x_series_datasheet.pdf> (June 19, 2014).

105. Thermomass®. (2012B). "Thermomass® CC Series." *Thermomass® CC Series Datasheet*, <http://www.thermomass.com/files/thermomass_cc_series_datasheet.pdf> (June 19, 2014).

www.manaraa.com

106. Thiagarajan, G, Vasudevan, A.K., Robert, S. (2010). "Numerical modeling of concrete slabs reinforced with high strength low alloy vanadium steel bars subjected to blast loads." *ACI Special Publication*, Issue 281 SP: 263-277.

107. Trasborg, P., Naito, C. (2013). "Composite action in insulated concrete wall systems." *Concrete Plant International,* 6: 164-168.

108. Trasborg, P., Naito, C., Bocchini, P., Olmati, P. (2014a). "Fragility Analysis for Ballistic Design." *Structural Safety Journal*, STRUCS-D-14-00038, Submitted.

109. Trasborg, P., Naito, C., Davidson, J. (To be submitted). "Experimental and analytical evaluation of insulated wall panels." *ASCE Journal of Structural Engineering*.

110. Trasborg, P., Nickerson J., Naito C., Olmati P., Davidson J. (2014b). "Forming a predictable flexural mechanism in reinforced wall elements." *ACI Structural Journal*, Submitted.

111. Twisdale, L., A., Sues, R., H., Lavelle, F., M. (1993). "Reliability-based analysis and design methods for reinforced concrete protective structures." *Final Report*, Engineering Research Division, Air Force Civil Engineering Support Agency, Civil Engineering Laboratory, Tyndall Air Force Base, FL.

112. Underwriters Laboratories (UL). (2005). "UL standard for safety for bullet-resisting equipment." *UL 752*, ISBN 0-7629-1080-1.

113. US Army Corps of Engineers. (2008a). "Single Degree of Freedom Structural Response Limits for Antiterrorism Design." *Report PDC-TR 06-08.*

114. USACE (2008b). "Methodology Manual for the Single-Degree-of-Freedom Blast Effects Design Spreadsheets (SBEDS)." *US Army Corps of Engineers*.

www.manaraa.com

115. U.S. Green Building Council (USGBC) (2005). "LEED® for new construction and major renovations version 2.2."

116. Vamvatsikos, D., Dolsek, M. (2011). "Equivalent constant rates for performance-based seismic assessment of ageing structures." *Structural Safety*, 33(1): 8-18.

117. Wang, F., Wan, Y.K.M., Chong, O.Y.K., Lim, C.H., Lim, E.T.M. (2008). "Reinforced concrete slab subjected to close-in explosion." *Proceedings: 7th German LS-DYNA Forum*, Bamberg, Germany.

118. The White House. (2009). "Federal leadership in environmental, energy, and economic performance." *Office of the Press Secretary*. Executive Order 13514.

119. Whitney, C. S. (1937). "Design of Reinforced Concrete Members Under Flexure or Combined Flexure and Direct Compression." *Jounal of the American Concrete Institute*. March-April, 33: 483-496.

120. Widdle, RD, Bajaj, AK, Davies, P. (2008). "Measurement of the Poisson's ratio of flexible polyurethane foam and its influence on a uniaxial compression model." *International Journal of Engineering Science*, 46: 31-49.

121. Williams, G.D., Williamson, E.B. (2011). "Response of reinforced concrete bridge columns subjected to blast loads." *Journal of Structural Engineering*, 136(9): 903-913.

122. Woltman, G., Tomlinson, D., Fam, A. (2013). "Investigation of various GFRP shear connectors for insulated precast concrete sandwich wall panels." *ASCE Journal of composites for construction*, 17: 711-721.

www.manaraa.com

123. Wu, C., Oehlers, D.J., Rebentrost, M., Leach, J., Whittaker A.S. (2009). "Blast testing of ultra-high performance fibre and FRP-retrofitted concrete slabs." *Engineering Structures,* 31: 2060-2069.

124. Wu, Y.-F. (2006). "New Avenue of Achieving Ductility for Reinforced Concrete Members." *ASCE Journal of Structural Engineering*: 1502-1506.

125. Xu, K., Lu, Y. (2006). "Numerical simulation study of spallation in reinforced concrete plates subjected to blast loading." *Computers and Structures*, 84: 431–438.

126. Yamaguchi, M., Murakami, K., Takeda, K., Mitsui, Y. (2011). "Blast resistance of double-layered reinforced concrete slabs composed of precast thin plates." *Journal of Advanced Concrete Technology*, 9(2): 177-191.

127. Yankelevsky, D., Z. (1997). "Local response of concrete slabs to low velocity missile impact." *International Journal of Impact Engineering*, 19(4): 331-343.

128. Zaker, T., A. (1975). "Fragment and debris hazards." *Report No. DDESB TP 12*, Department of Defense Explosives Safety Board.

129. Zhou, X.Q., Kuznetsov, V.A., Hao, H., Waschl, J. (2008). "Numerical prediction of concrete slab response to blast loading." *International Journal of Impact Engineering*, 35: 1186-1200.

130. Zineddin, M., Krauthammer, T. (2007). "Dynamic response and behavior of reinforced concrete slabs under impact loading." *International Journal of Impact Engineering,* 34: 1517-1534.

www.manaraa.com

AUTHOR BIOGRAPHY

Patrick Trasborg was born in Riverview Medical Hospital in Red Bank, New Jersey on May 18th, 1988. Raised in Shrewsbury, New Jersey by parents Paul and Patricia Trasborg.

Education

Lehigh University, Bethlehem, PA
M.S. Structural Engineering, May 2012
Graduate GPA **3.89**/4.00

B.S. Civil Engineering, May 2010
Undergraduate GPA **3.87**/4.00

Honors

Dean's Teaching Assistantship	Fall 2013	Chi Epsilon	Spring 2009
Rossin Doctoral Fellow	Spring 2012	Tau Beta Pi	Spring 2009
President's Scholar	Spring 2010	Co-Op Student, KCI Technologies.	Spring 2008
B.S.with Highest Honors	Spring 2010	Mansfield Merriman Scholarship	Fall 2007
Moles' Scholarship Award	Fall 2009	Eagle Scout, Troop 50. Boy Scouts	Spring 2004

Publications

Nikolov, N., Trasborg, P. (To be Submitted). "Structural Topology Optimization in Architectural Design."

Trasborg, P., Naito, C., Davidson, J. (Submitted). "Experimental Performance and Predictive Modeling of Partially Composite Insulated Precast Concrete Panels." ASCE Journal of Structural Engineering, STENG-3729

Nickerson, J, M., Trasborg, P. A., Naito, C., J., Newberry, C., M., Davidson, J., S. (Submitted). "Finite Element Assessment of Methods for Incorporating Axial Load Effects into Blast Design SDOF Analyses of Precast Wall Panels." *ASCE Journal of Performance of Constructed Facilities*, CFENG-1035

Olmati, P., Trasborg, P., Naito, C., Bontempi, F. (Submitted). "Prediction of Response of Reinforced Concrete Slabs using Finite Element Methods." *ACI Structural Journal Special Publication*

Trasborg, P., Naito, C., Bocchini, P., Olmati, P. (Submitted). "Fragility Analysis for Ballistic Design." *Structural Safety Journal*, STRUCS-D-14-00038

Olmati, P., Naito, C., Davidson, J., Newberry, M., Trasborg, P. (Submitted). "Assessment of Insulated Concrete Walls to Close-In Blast Demands." *ASCE Journal of Performance of Constructed Facilities*, CFENG-942

Trasborg, P., Nickerson, J., Naito, C., Davidson, J., Olmati, P. (Submitted). "Forming a Predictable Flexural Mechanism in Reinforced Wall Elements." *ACI Structural Journal,* S-2013-371

Olmati, P., Trasborg, P., Naito, C., Bontempi, F. (Submitted). "Blast Resistance of Reinforced Precast Concrete Walls Under Uncertainty." *International Journal of Critical Infrastructures*, IJCIS 60911

Trasborg, P., Naito, C. (December 2013). "Bridge Condition Ratings." *Pennsylvania Department of Transportation Local Technical Assistance Program*, Moving Forward, Winter 2013

Trasborg, P., Naito, C. (December 2013). "Composite Action in Insulated Concrete Wall Systems." *Concrete Plant International Magazine*, Issue 6

www.manaraa.com